SSCL-SR-1155
SSC-LOI0003

EMPACT/TEXAS

Letter of Intent

to

Write a Proposal

for an

Experiment

at the

Superconducting Super Collider

November 30, 1990

Coordinator: Michael D. Marx — SUNY at Stony Brook, NY 11794
Phone (516) 632-8102 FAX (516) 632-8101
SBHEP::MARX MARX@SBHEPNY

Deputies:
James E. Brau — University of Oregon
Howard A. Gordon — Brookhaven National Laboratory
Robert C. Webb — Texas A&M University

FRONT COVER

A cutaway view of the EMPACT/TEXAS detector in a three-dimensional model showing most of the details of the detector systems. Visible at the center of the detector are the tracking systems consisting of transition radiation detectors, scintillating fiber preshower detectors, and silicon pads. Surrounding the tracking is a hermetic system of calorimetry—the scintillating fiber in lead (SPACAL) option is shown. Outside the calorimetry is the muon spectrometer, consisting of double superlayers of muon detectors before and after superconducting air-core toroids.

BACK COVER

A three-dimensional model of the EMPACT/TEXAS detector in its underground hall shows installation of one end calorimeter. Visible is the novel overhead support scheme, feasible because of the relatively light weight of the detector. The central elements, including calorimetry, muon toroids, and detectors, are on fixed frames, while the end toroids and muon detectors are mobile, facilitating access and installation of the central elements as shown. Also visible are the large shafts for the installation of major detector assemblies. Through these shafts the full central calorimeter in its support tube, 45° segments of the central toroid, and fully assembled end toroids are lowered.

ACKNOWLEDGMENTS

We gratefully acknowledge the wonderful working environment and hospitality of Martin Marietta Astronautics Group Science Systems, and the competence and cheerfulness of the members of Martin Marietta Astronautics Group art, editorial, production, and secretarial staff who smoothed the production process for the EMPACT/TEXAS Letter of Intent. In particular, we thank Sharon Emas, Ken Ensey, Beverly Gallegos, Deb Krull, and Kevin Perizzolo for an outstanding job. The research represented in this document has been supported in part by the U.S. Department of Energy; the National Science Foundation; the SSC Laboratory through its Generic Detector R&D, Subsystem Development, and bridge funding programs; the Texas National Research Laboratory Commission through funding and fellowship programs; the Urban Development Corporation of New York State; and the collaborating institutions. The advanced state of the detector designs presented in this proposal is possible because of the major technical support of the Grumman, Martin Marietta, and LeCroy Corporations.

ABSTRACT

The EMPACT/TEXAS Letter of Intent represents a merger of the EMPACT, TEXAS, and 10^{34} Expressions of Interest previously submitted to the SSC Laboratory. The proposed detector provides a balanced approach to electrons, photons, muons, jets, and missing p_T, all of which are important signatures for high-mass particles and other high p_T phenomena at the SSC. It includes a combined transition radiation detector and tracker; a scintillating fiber preradiator with silicon pads; hermetic liquid argon or scintillating fiber calorimetry with lead absorber, and a high-resolution electromagnetic section; and a robust muon system with good resolution and acceptance based on superconducting air-core toroids. Each of these systems has been chosen with careful attention to the requirements of a wide range of possible physics signatures and to the cost guidelines provided by the SSC. Significant engineering effort and R&D have established the feasibility of the baseline design and will provide the basis for its further optimization. The collaboration has profited by strong engineering and system-integration support from its industrial partners, greatly contributing to the credibility and cost effectiveness of the experiment.

CONTENTS

Section **Page**

1.0 OVERVIEW
- 1.1 INTRODUCTION....1-1
- 1.2 PHYSICS PROGRAM....1-2
- 1.3 DESIGN AND COST STUDIES....1-5
- 1.4 BASELINE AND PERFORMANCE SPECIFICATIONS....1-6
- 1.5 DETECTOR OPTIMIZATION....1-10

2.0 CALORIMETRY
- 2.1 INTRODUCTION....2-1
- 2.2 PHYSICS REQUIREMENTS....2-1
- 2.3 SCINTILLATING FIBER CALORIMETRY....2-3
- 2.4 LIQUID ARGON LEAD CALORIMETRY....2-8
- 2.5 FORWARD CALORIMETRY....2-11
- 2.6 TRIGGER....2-13

3.0 MUON SYSTEM
- 3.1 INTRODUCTION....3-1
- 3.2 SUPERCONDUCTING TOROIDS....3-1
- 3.3 MUON DETECTORS BASELINE CONFIGURATION....3-4
- 3.4 MUON SYSTEM PERFORMANCE AND ROBUSTNESS....3-9

4.0 TRACKING AND PARTICLE IDENTIFICATION
- 4.1 INTRODUCTION....4-1
- 4.2 DESCOPING OF THE TRACKING SYSTEMS....4-1
- 4.3 BASELINE DESIGN....4-1
- 4.4 ELECTRONICS....4-4
- 4.5 R&D RESULTS....4-6
- 4.6 PRINCIPAL R&D EFFORTS....4-8

5.0 ELECTRONICS, DATA ACQUISITION, AND COMPUTING
- 5.1 FRONT END ELECTRONICS....5-1
- 5.2 LEVEL 1 AND LEVEL 2 TRIGGERS....5-1
- 5.3 READOUT AND THE LEVEL 3 RANCH....5-2
- 5.4 ELECTRONICS COSTS....5-3
- 5.5 OFFLINE COMPUTING....5-3

CONTENTS (contd)

Section **Page**

6.0 PHYSICS
- 6.1 INTRODUCTION 6-1
- 6.2 SIMULATION TOOLS 6-1
- 6.3 PHYSICS QUESTIONS 6-2
  - 6.3.1 Higgs Boson 6-2
  - 6.3.2 Top Quark 6-10
  - 6.3.3 Jet Energy Resolution 6-12
  - 6.3.4 Lepton Detection 6-14
- 6.4 ADDITIONAL PHYSICS STUDIES 6-16
  - 6.4.1 Supersymmetry 6-16
  - 6.4.2 Limits on Quark Compositeness 6-18

7.0 COST, SCHEDULE, AND MANAGEMENT
- 7.1 INTRODUCTION 7-1
- 7.2 EoI BASELINE METHODS 7-1
- 7.3 EVOLUTION OF THE EMPACT/TEXAS DETECTOR 7-1
- 7.4 LoI COST ESTIMATE METHODS 7-2
- 7.5 EMPACT/TEXAS COST AND CONTINGENCY ESTIMATES 7-5
- 7.6 SCHEDULE AND ESCALATED COSTS 7-7
- 7.7 MANAGEMENT 7-14

EMPACT/TEXAS PARTICIPANTS

R. Steiner
Adelphi University, Garden City, New York 11530

M. G. Eklund, G. E. Forden, E. W. Jenkins,
J. P. Rutherfoord, L. S. Shaver, M. A. Shupe
University of Arizona, Tucson, Arizona 85721

E. Booth, R. Carey, S. Dye, T. Johnson, S. Klein, J. Miller, B. L. Roberts,
J. T. Shank, J. Stone, L. Sulak, J. S. Whitaker, R. J. Wilson, W. Worstell
Boston University, Boston, Massachusetts 02215

G. T. Emery
Bowdoin College, Brunswick, Maine 04011

M. S. Atiya, I-H. Chiang, E. Duek, B. G. Gibbard,
H. A. Gordon, J. S. Haggerty, S. Kahn, T. F. Kycia,
L. Littenberg, H. Ma, Y. Makdisi, D. Makowiecki, W. M. Morse, M. J. Murtagh,
F. E. Paige, E. Platner, S. Protopopescu, M. J. Tannenbaum, S. P. Yamin
Brookhaven National Laboratory, Upton, New York 11973

W. Ko, R. Lander, P. M. Yager
University of California at Davis, Davis, California 95616

H. Kobrak, G. Masel, H. Paar, R. Swanson
University of California at San Diego, La Jolla, California 92093

R. M. Edelstein, J. S. Russ
Carnegie Mellon University, Pittsburgh, Pennsylvania 15213

C. Lane
Drexel University, Philadelphia, Pennsylvania 19104

D. R. Winn
Fairfield University, Fairfield, Connecticut 06430

S. Linn, J. Womersley
Florida State University, Tallahassee, Florida 32306

T. G. Brown, J. J. Connelly, P. A. Fraser, S. R. Gottesman, F. Halfen, J. Klafin,
W. R. Matlach, J. R. Mueller, T. Myers, J. Pusateri, P. T. Spampinato, D. Weiss
Grumman Corporation, Bethpage, New York 11714

C. Avilez, W. Correa, G. Moreno
Universidad de Guanajuato, Leon, Mexico

D. Hungerford, K. Lau, B. W. Mayes II, D. Parks, L. S. Pinsky, J. Pyrlik, R. Weinstein
Institute for Beam Particle Dynamics, University of Houston, Houston,
Texas 77204

T. Marshall, H. J. Martin, D. Zieminska, A. Zieminski
Indiana University, Bloomington, Indiana 47405

E. G. Boos, N. N. Nurgozhin, W. Voinov
Institute for High Energy Physics, Alma-Ata, U.S.S.R.

I. Azhgirey, A .F. Borisov, A. F. Busulutskov, O. Buyanov,
S. Chernichenko, A. Denisov, D. Denisov, V. A. Dorofeev, Yu. Ermolin,
N. N. Fedyakin, A. Galyaev, V. Glebov, S. V. Golovkin, A. Gorin, A. Kholodenko,
A. E. Kiryunin, E. Kistenev, V. I. Kochetkov, A. P. Koshevnikov, I. V. Kotov,
A. S. Kozhin, V. Kravtsov, V. P. Kubarovsky, A. V. Kulik, N. Kulman,
A. I. Kulyavtsev, V. Kurshetsov, A. Kushnirenko, L. G. Landsberg, S. V. Los,
A. Medvedkov, E. Melnikov, Yu. Michailov, N. V. Mokhov, V. Molchanov,
V. A. Mukhin, V. Onuchin, A. Pereypkin, S. Petrenko, Yu. Pirogov,
Yu. M. Pischalnikov, V. K. Semenov, K. E. Shestermanov, A. Soldatov,
V. Vasil'chenko, A. Zaichenko
Institute for High Energy Physics, Protvino, U.S.S.R.

H. A. Baturitsky, Yu. V. Gilitsky, A. A. Kubasov, E. I. Podolny, M. M. Shumeik
Institute for Nuclear Problems, Byelorussian State University,
Minsk, U.S.S.R.

V. Bolotov, S. Gninenko, V. Isakov, V. Laptev, V. A. Matveev,
A. Poblaguev, V. Postoev
Institute for Nuclear Research, Moscow, U.S.S.R.

A. Kharchilava
Institute of Physics of the Georgian Academy of Science, Tbilisi, U.S.S.R.

M. Gritsuk, Yu. Gryshkin, A. Ya. Kochanov, I. E. Korolko, V. Kozitsyn, A. Ostapchuk,
O. Pogorelko, O. Zemskov
Institute of Theoretical and Experimental Physics, Moscow, U.S.S.R.

G. Alexeev, A. V. Bannikov, L. S. Barabash, S. A. Baranov,
G. Bitsadze, J. Bohm, Yu. E. Bonyushkin, G. Chelkov, O. Denisov,
B. Fialovszky, Yu. A. Gornushkin, M. A. Ignatenko, B. A. Kalinnikov,
M. Yu. Kazarinov, B. Khomenko, N. N. Khovansky, O. Klimov, A. V. Korytov,
Z. V. Krumstein, P. A. Kulinich, V. L. Malyshev, Yu. P. Merekov, G. V. Mitselmakher,
A. A. Nozdrin, A. G. Olsheveki, K. Piska, A. A. Popov, S. Prakhov, C. Razin,
A. N. Sissakian, G. D. Stoletov, L. Tkatchev, T. P. Todorov, V. V. Tokmenin,
L. S. Vertogradov, S. Vyskocil
Joint Institute for Nuclear Research, Dubna, U.S.S.R.

R. Ammar, P. Baringer, R. Davis, N. Kwak
University of Kansas, Lawrence, Kansas 66045

M. Lowry, C. McConaghy
Lawrence Livermore National Laboratory, Livermore, California 94551

B. Govorkov, G. Kaluzhnaj, V. Kurbatov,
V. Raevsky, L. Shtarkov, V. Shubin, G. Sokol
Lebedev Physical Institute, Moscow, U.S.S.R.

J. Hoftiezer, L. Klassen, T. Majors, K. Roberts
LeCroy Corporation, Chestnut Ridge, New York 10977

A. Kanofsky
Lehigh University, Bethlehem, Pennsylvania 18015

R. R. McNeil
Louisiana State University, Baton Rouge, Louisiana 70803

T. Adams, J. Bakken, J. Brogan, N. J. DiGiacomo,
B. Easom, G. Flores, G. Guenterberg, G. Hanowski, K. Killian,
L. Mason, M. Montgomery, J. Petry, J. Pohlen, T. Wright, G. Zambre
Martin Marietta Astronautics Group, Denver, Colorado 80201

D. Jensen, M. Rabin
University of Massachusetts at Amherst, Amherst, Massachusetts 01003

W. Busza, J. I. Friedman, T. Hansl-Kozanecka,
H. Kendall, T. Lyons, L. S. Osborne, L. Rosenson, F. Taylor, R. Verdier
Massachusetts Institute of Technology, Cambridge, Massachusetts 02139

M. A. Abolins, B. G. Pope
Michigan State University, East Lansing, Michigan 48824

V. Bondarenko, S. Furletov, V. Grigoriev, R. Kokoulin, I. Markina
Moscow Engineering and Physical Institute, Moscow, U.S.S.R.

A. A. Arodzero, G. L. Bashindjagyan, S. F. Berznev, P. F. Ermolov,
Yu. V. Fisyak, V. G. Gavryasev, A. N. Larichev, A. K. Leflat, S. M. Ruzin,
E. K. Shabalina, N. A. Sotnikova, A. G. Voronin, Y. V. Yarba, S. A. Zotkin
Moscow State University, Moscow, U.S.S.R.

O. Ye. Gorchakov, A.V. Kulikov, V. Kurochkin, S. V. Trusov, V. V. Yazkov
Moscow State University, Dubna Branch, Dubna, U.S.S.R.

T.-Y. Chen, G. Gao, D. Xi
Nanjing University, Nanjing, People's Republic of China

J. Kourlas, A. Mincer, M. Mudan, P. Nemethy, J. Sculli
New York University, New York, New York 10003

G. Alverson, W. Faissler, D. Garelick,
M. Glaubman, A. Grimes, I. Leedom, C. Lirakis,
J. Moromisato, E. Pothier, S. Reucroft, E. Saletan, E. von Goeler, T. Yasuda
Northeastern University, Boston, Massachusetts 02115

K. G. Falter, J. Luton, R. A. Todd
Oak Ridge National Laboratory, Oak Ridge, Tennessee 37831

J. E. Brau, R. E. Frey, K. Furuno, C. J. Zeitlin
University of Oregon, Eugene, Oregon 97403

P. Bonanos, M. M. Ito, D. Marlow, P. Meyers
Princeton University, Princeton, New Jersey 08544

P. Draper, G. Fanourakis, T. Ferbel
University of Rochester, Rochester, New York 14627

S. F. Novaes
Universidade Estadual de São Paulo, São Paulo, Brazil

P. Eboli, C. O. Escobar, P. Gouffon
Universidade de São Paulo, São Paulo, Brazil

C. Rosenfeld, J. R. Wilson
University of South Carolina, Columbia, South Carolina 29208

R. Engelmann, M. Gundy, C.-K. Jung, M. D. Marx,
R. McCarthy, M. M. Mohammadi, M. Quint, M. Rijssenbeek
State University of New York at Stony Brook, Stony Brook,
New York 11794

L. R. Cormell, K. Morgan, F. Stocker, G. P. Yost
Superconducting Super Collider Laboratory, Dallas, Texas 75237

N. S. Amaglobeli, W. P. Dzhordzhadze,
A. J. Mchedlishvili, D. A. Mzavia, R. G. Shanidze, F. G. Tkebuchava
Tbilisi State University, Tbilisi, U.S.S.R.

T. Kamon, R. Webb
Texas A&M University, College Station, Texas 77843

G. W. Hoffmann, C. Kao, P. J. Riley, J. L. Ritchie, A. Yamashita
University of Texas at Austin, Austin, Texas 78712

R. S. Panvini, J. P. Venuti
Vanderbilt University, Nashville, Tennessee 37235

C. Schwarz
Vassar College, Poughkeepsie, New York 12601

V. Cook, D. Forbush, P. M. Mockett, J. Rothberg, F. Toevs
University of Washington, Seattle, Washington 98195

M. Eckhause, J. R. Kane, R. E. Welsh, R. G. Winter
College of William and Mary, Williamsburg, Virginia 23185

R. K. Adair, P. Cushman, H. Kasha, M. P. Schmidt
Yale University, New Haven, Connecticut 06511

N. Dashyan, N. Khalatyan, A. Saribekyan, A. Yeritsyan
Yerevan Physics Institute, Armenia, U.S.S.R.

1.0 OVERVIEW

1.1 INTRODUCTION

The major detectors constructed for the new Superconducting Super Collider Laboratory (SSCL) must justify the enormous investment in the machine by having the capability to exploit the full potential of the world's premier facility for high-energy physics during the first decades of the next century. This entails the ability to search for a wide variety of predicted phenomena, sensitivity to the unexpected, and the ability to use the full luminosity of the SSC as it improves. It is the purpose of this Letter of Intent (LoI) to provide the basis for approval of an experiment—EMPACT/TEXAS—that can maximally exploit opportunities offered by the SSC. We describe a detector system offering a balanced emphasis on the key signatures for new physics and having the capability of extracting these signals at high luminosities. A detailed cost basis has been used to define the scope of the project within which the detector can be further optimized.

This proposal is based on the efforts of three groups that submitted Expressions of Interest (EoI) in May—EMPACT (Electrons, Muons, Partons with Air Core Toroids); TEXAS (Totally hermetic EXperiment At the Supercollider); and 10^{34} [1, 2, 3]. (Hereafter these Expressions of Interest are referred to as EEoI, TEoI, and HLEoI.) The groups share a common philosophical emphasis in the design of an SSC experiment—to provide a detector capable of running at high luminosity, consisting primarily of excellent electromagnetic and hadron calorimetry coupled with a robust muon system. Calorimetry at high energies and luminosities provides the best measurement of electrons, photons, jets, and noninteracting particles. A robust muon system implies excellent resolution over a large solid angle, including forward coverage; capability of using the highest attainable luminosities; and high efficiency and redundancy in the face of high rates exacerbated by hadronic and electromagnetic debris, with a magnetic spectrometer insensitive to minor faults. The detector is intended to be complementary to a general-purpose device that emphasizes magnetic tracking and is competitive in its ability to study high p_T phenomena with distinct advantages in superior calorimetry, muon systems, and ability to exploit high luminosity.

The design of the detector under consideration has been strongly influenced by the desire to close all windows for the elusive Higgs, from the LEP 200 regime of 80 GeV to very heavy Higgs manifesting itself as strongly interacting intermediate vector bosons. But the Higgs is only one of many possibilities. The detector will also provide the ability to search for extended gauge groups, for new quark or lepton families, for indications of the compositeness of quarks, and for new noninteracting particles. It is felt that a detector optimized and tested against these goals will also be in a position to discover new and unexpected phenomena that may occur at the SSC energy scale.

Since the submission of the EoIs in May and the subsequent actions of the Program Advisory Committee (PAC), the collaboration has devoted its effort to sharpening the focus of the experiment and to reducing its scope within the PAC guidelines. The nonmagnetic tracking and calorimeter environment has been confirmed as the optimal choice for maintenance of the detector performance at high luminosity, stressing calorimetry over tracking functions. The tracking system has been reduced in scope with the elimination of a vertex detector. The central feature is an elegant system of transition radiation detector (TRD) tracking, now beam tested, that provides excellent particle identification and vertex determination. Pattern recognition and ϕ tracking are provided by a combined scintillating fiber tracker and preconverter augmented by silicon pads. Excellent hermetic calorimetry consisting of either scintillating fiber/lead (SPACAL), or liquid argon (LAr) with lead absorber has been improved to provide high resolution for electromagnetic showers, enabling a search for a low-mass Higgs using its 2γ decay mode at low or high luminosity.

Finally, the muon system has been made more robust while reducing costs. The central feature of the muon spectrometer remains a system of three large superconducting air core toroids. An alternate

design of an optimized system of iron toroids was designed, costed, and evaluated for system performance, and found to be inadequate for our physics goals. Significant effort by major magnet fabricators and fusion laboratories have further bolstered confidence in the feasibility of construction and reliability of air-core toroid magnets and have provided a firm cost basis for their construction. System robustness has been improved by opening the bore of the central toroid, permitting line-line measurements with space point readout on the inner chambers and by the inclusion of inner tracking information to improve the efficiency for very high momentum tracks most likely to have accompanying electromagnetic debris. This has reduced the probability of losing a muon track, while allowing the scope of the toroids to be reduced by lowering the fields and reducing their size. Because of the improved precision of the four-point measurements, the number of planes and channels in the muon detectors has been reduced without seriously affecting the attainable resolution. The additional radial space provided by increasing the bore permits a broader optimization of tracking, calorimetry, and muon volumes in the next phase of the design.

Of critical value in this process have been teams of engineers and physicists from our industrial collaborators, Grumman and Martin Marietta. Given the scale of the SSC detectors, EMPACT/TEXAS has from the outset used expertise available in the aerospace industry to assist in design and integration of the detector concepts. In the time period between EoI and LoI the utility and efficiency of using industry has been abundantly confirmed. Drawing from the pool of manpower available, the teams have tripled in numbers to respond to the time pressure of the PAC requests. This increase would have been impossible in the normal environment of high-energy physics. The additional manpower, including professionals in manufacturing, costing, and other critical areas of major project development, has been smoothly integrated into the effort. This pool of expertise is an invaluable resource available in major industry. This work, in conjunction with SSCL staff, has provided the basis for the SSCL cost guidelines for all detectors. In this short time period, the baseline detector was fully costed, and new designs investigated, iterated, and thoroughly modeled. It is this expertise that gives us confidence in the ability to provide a detector that has been optimized to provide the best performance at the lowest cost, within the constraints of the physics requirements and fiscal realities. While projects on the SSC scale are new for high-energy physics, they are commonplace in aerospace, and it seems advisable to use the expertise, experience, and tools developed over many years.

1.2 PHYSICS PROGRAM

The primary motivation for the construction of a 40 TeV hadron collider is to explore electroweak symmetry breaking, that is, the origin of the masses of the gauge bosons and the quarks and leptons [4]. While the source of this symmetry breaking is unknown, the mass scale at which it must manifest itself is not. If there is no new physics, then the interactions of the longitudinal components of the vector bosons, W_L and Z_L, must increase with energy, violating unitarity at the 1–2 TeV scale. This fact sets the 1 TeV mass scale for electroweak symmetry breaking. In the standard model this new physics is a single scalar Higgs boson. Among the possible alternatives, supersymmetric models, which have profound implications for the unification of all forces, produce a host of new particles with well defined interactions and decays but undetermined masses. Possible signatures include multiple jets with large missing p_T and like-sign dileptons. Technicolor and other dynamical symmetry breaking models replace elementary Higgs bosons with composite particles, predicting a rich spectrum at the 1 TeV scale and generally lighter particles as well. Alternatively, the role of the elementary Higgs might be played by a $t\bar{t}$ bound state formed by new dynamics at a very high mass scale [5]. Composite models replace the quarks and leptons themselves with dynamical bound states. Finally, if there is no new physics, then strong W_L and Z_L interactions must develop in the 1–2 TeV range [6]. A detector that measures jets, leptons,

photons, and missing p_T well and can exploit the ultimate luminosity of the SSC will be able to detect all of these possibilities.

The cleanest method for discovering the standard Higgs boson above the Z^0Z^0 threshold is through the decay of the Higgs to two Z^0's that subsequently decay to either electrons or muons. Figure 1-1 shows the contours in energy and luminosity for producing 20 such Higgs events with electrons or muons in the final state. Realistic detector and running efficiencies suggest that discovery in this channel for Higgs masses above 600 GeV will require the measurement of both electron and muon decays, and most likely higher luminosity. Figure 1-2 shows the reconstructed 400 GeV Higgs signal with background for both the air core and iron core toroids, and for two choices of mass cut on

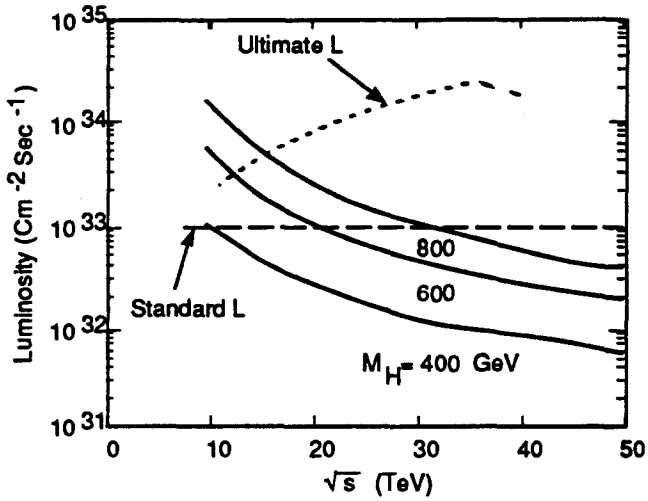

Figure 1-1 Luminosity required to produce in one year 20 Higgs bosons decaying to e or μ as a function of CM energy.

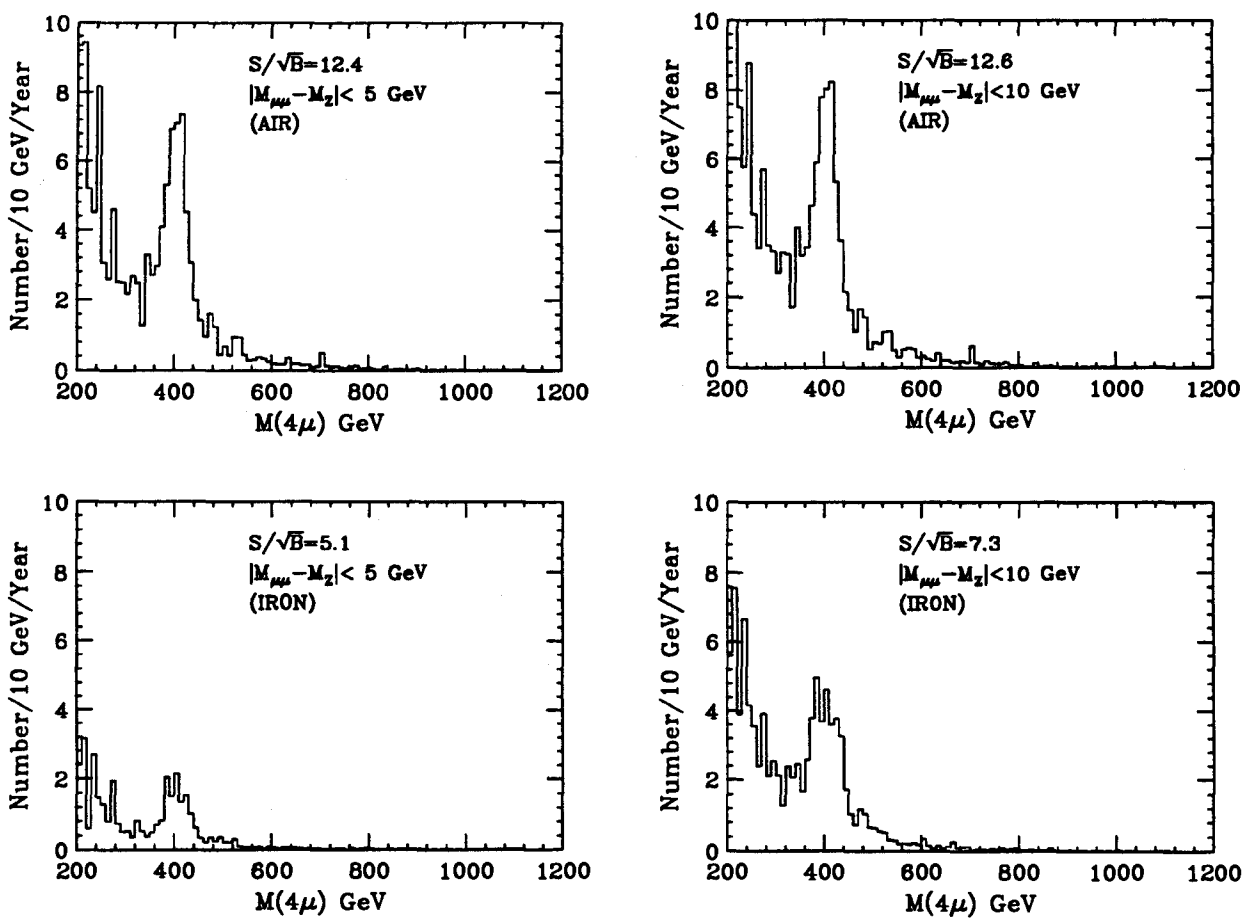

Figure 1-2 Reconstructed mass of 4μ system including 400 GeV Higgs with QCD ZZ and $t\bar{t}$ background for baseline air toroid and optimized iron toroids. Tight and narrow cuts on dimuon mass are shown.

reconstructed Z^0's. The premium of good resolution, is apparent.

As the Higgs mass increases and the cross section decreases, there emerges a need for searches in more complex decay channels. These include decays to Z^0Z^0 where one Z^0 is detected through the leptonic decay, and the other is detected by its decay to either jets or neutrinos. This underscores the need for excellent hadron calorimetry, for jet studies, and for missing p_T resolution. Because it now appears that this signal can be seen, good jet measurements will certainly be required. Forward tagging of spectator jets provides a critical handle, requiring an adequate forward calorimeter covering the region up to rapidities of 5.5. Figure 1-3 shows the clear Z signal in jet-jet mass, from the decay of a 800 GeV Higgs, requiring the other Z to decay leptonically, and the presence of a forward jet. The decays to WW are also available, but the double leptonic decay is unreconstructible, and there is a large background from the decay of heavy top.

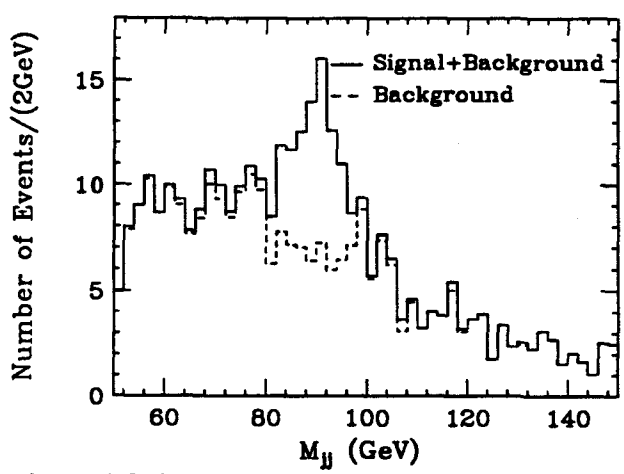

Figure 1-3 Signal and background for $Z \rightarrow jj$ from $H \rightarrow ZZ$ with one Z decaying to leptons and requiring a jet with $p_T > 50$ GeV and $\eta > 3$.

For Higgs masses below the Z^0Z^0 threshold but above about 80 GeV, different approaches are needed [7]. Below Z^0Z^0 threshold, ZZ*(virtual Z) production can be studied through similar channels as real Z^0Z^0. However, for the range from about 80 GeV to around 150 GeV, the most attractive option is to study the rare decay of the $H \rightarrow \gamma\gamma$. This has the added feature of providing sensitivity to the existence of nonstandard Higgs, such as those arising in supersymmetric models. Measurement of this branching ratio is a critical step in elucidating the Higgs sector in standard and nonstandard models. Superior calorimetry will be essential to reconstruct these narrow final states and to minimize the background. In addition to the irreducible background from genuine two-photon final states, further background events can arise from jet-jet and photon-jet events where the jet has a leading π^0 and masquerades as a photon. Two-photon events, photon-jet events, and two-jet events occur in the ratios of $1:10^4:10^8$ and so jets must be distinguished from photons with a rejection power exceeding 10^4 [7]. Jet rejection will be accomplished by a combination of isolation cuts on charged particles using the tracking system, electromagnetic and hadronic energy cuts using the calorimeter, and shower development and pattern cuts using the preshower detector. Discovery in this channel will be helped by runs at elevated luminosity. The background is much reduced for $H \rightarrow \gamma\gamma$ produced in association with a W [8]. This reduces the requirements on detector resolution, but because of the much lower associated production rate, may require running at high luminosity. Associated production might also permit the study of the Higgs decay to $b\bar{b}$, but the signal-to-background in this channel is small, requiring good b tagging with a vertex detector and rejection of $t\bar{t}$ decays.

For a very heavy Higgs in the TeV mass range, elucidation of symmetry breaking will come through studies of $W_L W_L$ final states. Extraction of the signal may require a measurement of event multiplicities [9] that is particularly suited to the capabilities of a nonmagnetic detector. Tagging of spectator jets can provide additional handles on extraction of this signal. Because of the small cross sections, it is likely that these studies can only be done at high luminosity, and thus are likely to be done using muon rather than electron decays.

The electroweak gauge group may be larger than in the standard model. In the search for new extended gauge groups, a key signal would be the detection of a heavy Z′ boson. While resolution is not likely to affect the discovery of such an object

because of the expected absence of background, an understanding of the character of the new object will come through measurements of its decay asymmetry. This requires a detector with good resolution and acceptance for muons in the forward region.

In addition to the exploration of the symmetry breaking sector, the SSC will provide the opportunity to search for evidence of new families of quarks and leptons. The SSC will be an ideal instrument for studying the top quark, whether or not it is discovered at the Tevatron. The top must be well understood, because it is a background to Higgs studies as well as a possible source of symmetry breaking if its mass arises through dynamical means. In addition, it is still possible, for example, to contemplate the existence of a fourth generation whose leptons (charged and neutral) are so heavy they do not affect the width measurements of the Z^0.

With the energies available at the SSC, it will be possible to extend the Rutherford scattering exploration for substructure of the quarks themselves. Through studies of very high p_T jets, it will be possible to detect compositeness at the scale of tens of TeV or, equivalently, objects 10^{-5} of the size of the proton. This imposes constraints on the quality of the hadron calorimetry—for linearity, dynamic range, and compensation.

Finally, the discovery limits of the SSC are determined by the energy and luminosity of the machine. Designing a detector that can accommodate luminosities significantly above the design luminosity of $10^{33}\,cm^{-2}s^{-1}$ will greatly extend the usefulness and power of the detector for discovery of higher mass phenomena. It is likely that the approach to high luminosity of the SSC will occur over a 5-year period, which will permit thorough studies of lower p_T physics like decays of top, enabling an increase of thresholds in p_T as the luminosity increases and attention shifts to studies of high mass and high p_T phenomena at the limits of accessible physics.

1.3 DESIGN AND COST STUDIES

The PAC guidelines issued in July specify a reduced detector scope consistent with U.S. funding of $250 to $300 million dollars, augmented with up to equal amounts of foreign funding. To propose a detector within these guidelines, it has been necessary first to determine with confidence the costs of the detectors originally proposed in the EoIs, then to parametrize these costs for changes in scope and performance, and finally to construct a limited number of detector examples that fit within the guidelines and accomplish the stated physics goals. In parallel with this work, negotiations with the Soviet participants in EMPACT/TEXAS have resulted in a draft agreement indicating an expected contribution at the level of one third of the total costs. We now have confidence that a detector of sufficient power can be built to provide a broad and successful attack on SSC physics issues, and that a major fraction of the requisite foreign funding can be secured.

To provide a baseline from which the descoped detector could be derived, the EMPACT detector, as described in the May EoI, was selected. Using detailed engineering designs of the major systems, a full-cost estimation was commissioned from our industrial partners. The major cost drivers of the experiment are the calorimetry, the toroidal magnets, and the electronics. The calorimetry was studied by Martin Marietta, who also coordinated the overall costing efforts. SPACAL was studied independently by Martin Marietta and the Draper Laboratory. The toroidal magnets were costed by Grumman using their own expertise augmented by independent estimates by General Dynamics (prime contractor for the SSC dipoles) and Ansaldo (fabricator of HERA dipoles). The entire electronics chain was studied and costed by LeCroy using their extensive experience in circuit and chip design for high-energy physics. In all of this cost estimation careful attention was paid to issues of risk and contingency, which was estimated item by item, with additional contingency generated by the use of accepted standard factors applied to the overall project that provides allowances for items and subsystems not initially costed. Much of this work was done in conjunction with SSC staff, and the method employed has been adopted by the SSC as the standard for all detectors.

As part of the costing tasks, effort was expended for each system to understand how the costs would extrapolate for changes in key parameters and design changes. For the calorimetry, costs were parametrized as a function of the segmentation, the starting radius and depth for variations in absorber material, and the fabrication assumptions. The toroids were studied in terms of changes in physical size and magnetic field strength, and the electronics costs were examined as a function of complexity and number of circuits in the chain. It is expected that the costs are a ceiling on the actual costs that would be obtained after new designs are executed, as there is considerable room for further optimization.

1.4 NEW DETECTOR BASELINE AND PERFORMANCE SPECIFICATIONS

The detector examples discussed in this LoI have been improved in reliability, robustness, and performance while reducing the overall cost. Figure 1-4 shows a side section of the detector with LAr calorimetry. For comparison, Fig. 1-5 shows the same section for the detector described in the EEoI. Figure 1-6 shows a quadrant of the detector with SPACAL calorimetry for this LoI and as described in the EEoI.

The tracking detector has been simplified in function and reduced in scope. The central feature remains a system of azimuthal straw tube chambers functioning as TRD and tracker. Prototype beam tests gave results consistent with calculations and have increased confidence in the system; these test results have been incorporated in simulations of system performance. The channel count for the TRD has been reduced by removing overlaps between adjacent sections and reducing the rapidity coverage to 2.5. Axial tracking and pattern recognition is accomplished with a modest system of scintillating fibers integrated with lead converters to provide assistance in electron identification, photon pointing, and γ/π^0 discrimination. The tracker is augmented with silicon pads matched to the calorimetry segmentation to aid in trigger and pattern recognition by resolution of ambiguities. One of the major goals for the next design phase is to complete the optimization of pattern recognition and particle identification, by considering these elements in conjunction with the calorimetry and a possible vertex detector. The latter has not been included as part of the current baseline, but because it can provide significant benefits, it will be evaluated to test its overall cost and performance within the scope described here.

The calorimetry technologies under consideration concentrate on SPACAL and LAr. Considerable design work incorporating new ideas of casting technology have significantly reduced overall SPACAL costs. In addition, the lateral segmentation has been coarsened, reducing channel count, and the fiber size in the hadronic section has been increased. Overall performance has been improved by the addition of a high-resolution electromagnetic section with finer sampling, sufficient to study the $H \rightarrow \gamma\gamma$ decay.

The LAr calorimetry cost has been reduced by replacing uranium absorber with lead. This is expected to affect the degree of compensation, but calculations indicate this will be within tolerable limits, and will be tested this spring. To maintain the depth of the calorimeter, the outer radius has been increased. To reduce costs, the longitudinal and transverse segmentation of the detector has been coarsened. Finally, to address the issue of $H \rightarrow \gamma\gamma$, the sampling of the electromagnetic section has been increased, improving the resolution.

Beam tests of both technologies have demonstrated sufficient resolution to achieve the stated goals. For example, JETSET [10] has achieved $6.5\%/\sqrt{E}$ with fiber calorimetry and NA31 [11] has achieved $7.5\%/\sqrt{E} \oplus 0.5\%$ with LAr. The $H \rightarrow \gamma\gamma$ signal with these resolutions is shown in Fig. 1-7.

Careful consideration has been given to avoid compromising the resolution and coverage of the hadron calorimetry, which is critical for studies of jets and missing p_T physics. The designs presented here are reasonable extrapolations of current experience, but particularly in the case of a new technology like SPACAL, must be proven by detailed engineering, construction of prototypes

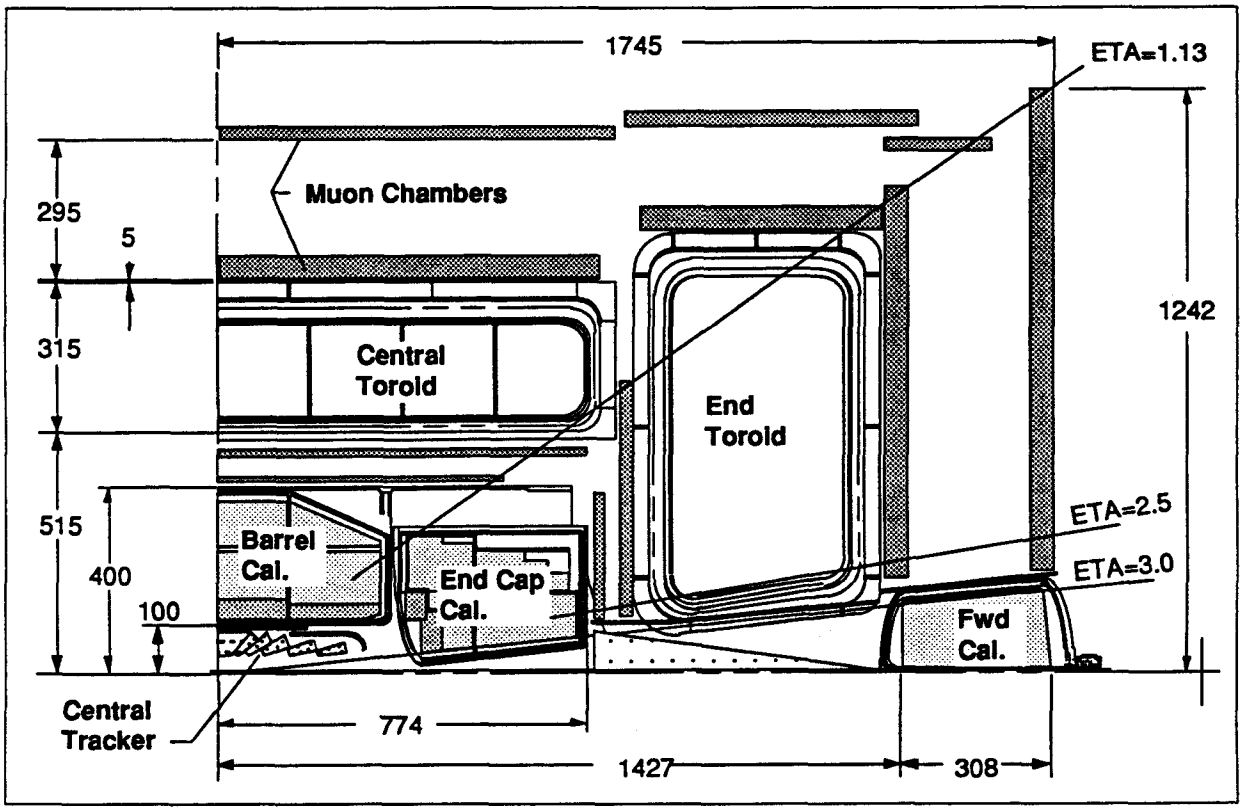

Figure 1-4 LoI detector section with LAr calorimeter.

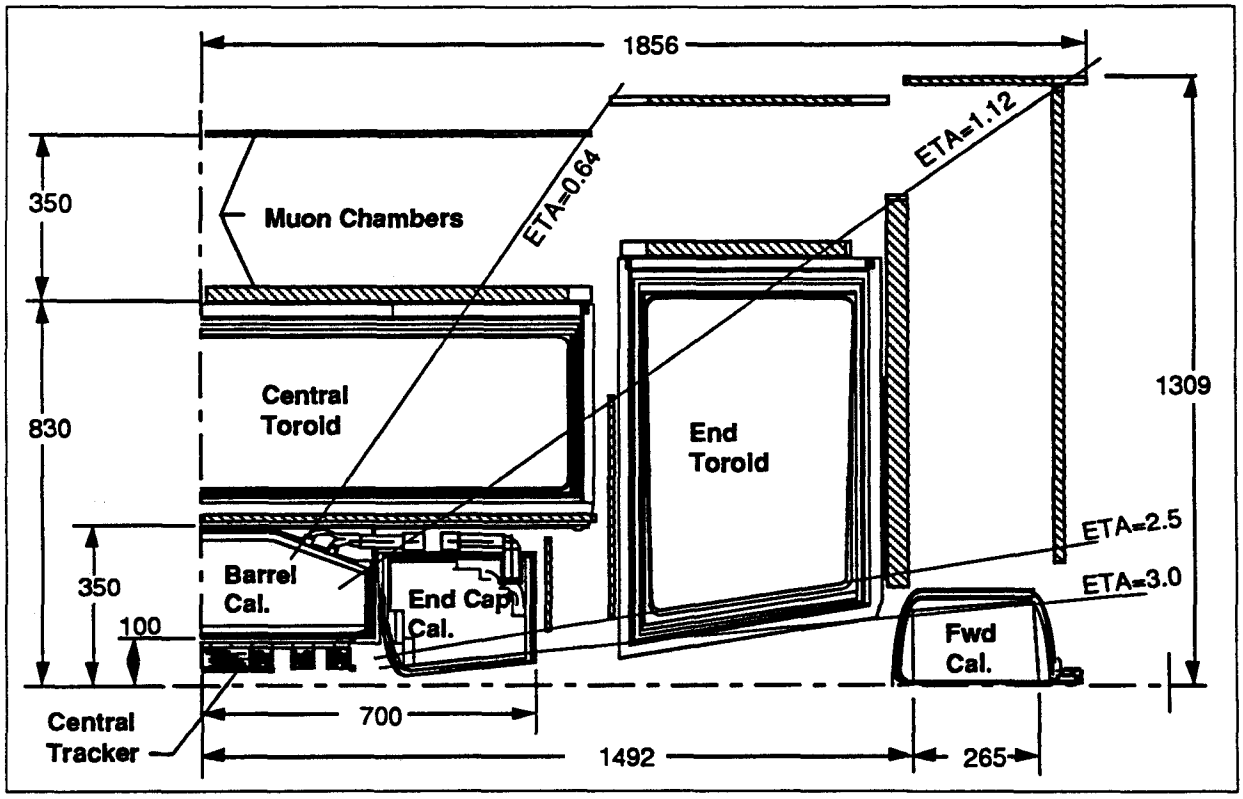

Figure 1-5 EEoI detector section with LAr calorimeter.

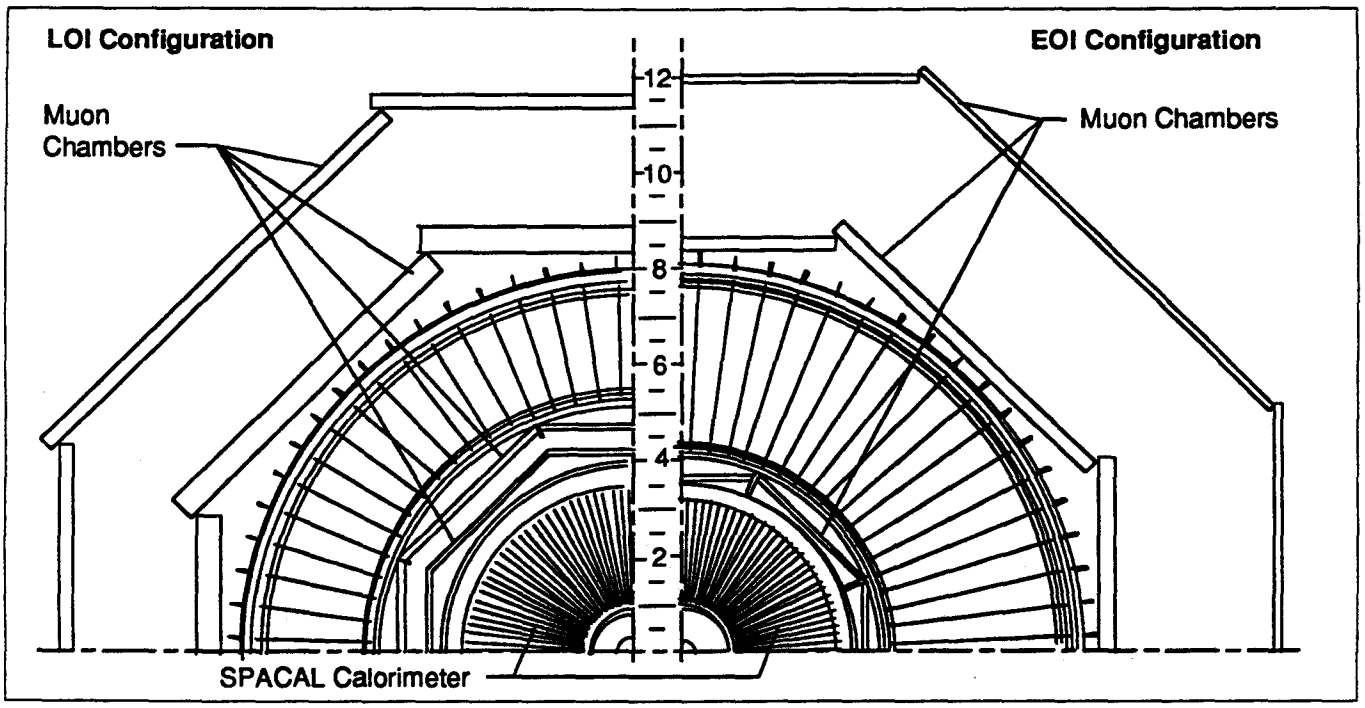

Figure 1-6 Quadrant section through beam for the LoI detector (left) and EEoI detector (right).

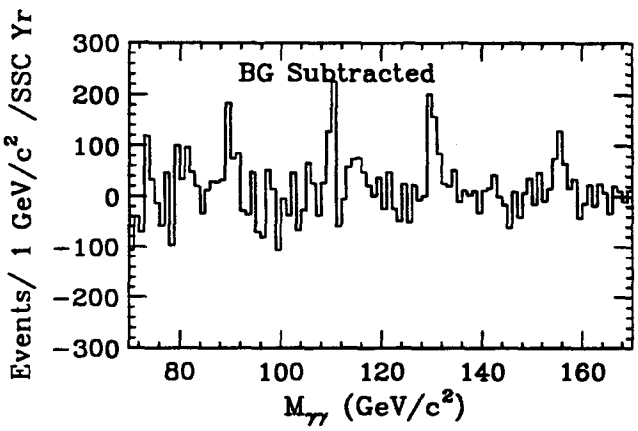

Figure 1-7 Background subtracted signal for $H \rightarrow \gamma\gamma$ for several masses (90, 110, 130, 150 GeV).

using improved manufacturing schemes, and performance testing. It is projected, that with appropriate R&D support, an informed choice of calorimeter technology based on performance and cost, could be made within a year.

Forward calorimetry to provide sufficient rapidity coverage for missing p_T studies has been retained. Technologies under study include scintillator-filled capillaries imbedded in lead (CAPCAL), liquid argon, and high-pressure argon gas. Significant progress has been made in calculating radiation levels in this region.

The muon system has undergone major revision. Since the EEoI, however, superconducting air-core toroids remain central elements of the spectrometer. Major design effort has been expended to confront issues of optimization, assembly cost, and schedule, employing expertise from major magnet fabricators and fusion laboratories. Resolution studies have underscored the improvement in performance to be gained by going from point-line measurements to line-line [12, 13]. To allow this, the inner radius of the central toroid has been increased to over 5 m, keeping the outer radius and maximum field the same, while the inner superlayer of chambers has been split in two. Although the field integral is reduced, the momentum resolution is essentially unchanged. The new design has the additional benefit of reducing the probability of losing a muon because of debris obscuring the track in the first chambers after the calorimetry. The space gained is available for lever arm, for displacing the first chambers away from the calorimetry further reducing backgrounds, and for relieving space constraints on the calorimetry system, permitting

full depth with lead absorber instead of uranium. Determination of the event vertex at the level achievable by the TRD provides additional robustness in the case where the inner muon chambers are obscured by debris accompanying high-momentum tracks.

The costs of the changes to the central toroid are minimal—reduced volume is offset by increased conductor costs. Major cost savings are accomplished by reducing the size and fields of the end toroids. The muon system has been further descoped by reducing the number of planes outside the toroids and slightly increasing the cell size. In addition, the outer lever arm has been reduced, decreasing the area of the chambers. At no additional cost, the nonbend chambers inside the toroids will be replaced with cathode strips providing space-point readout, greatly improving pattern recognition and muon finding in the busy environment after the calorimetry. Chamber construction, assembly, and alignment, while underfunded this year, are being studied in programs initiated in the U.S. and the Soviet Union.

With all these changes, good resolution for muons has been maintained. While somewhat degraded from the EEoI, the system still provides resolution comparable to the natural width of Z^0's from the decay of an 800 GeV Higgs as shown in Fig. 1-8 and is well matched to the kinematics of the decays of a heavy particle produced at the SSC. Also shown are the intrinsic width of the Z^0 and the improved resolution for electron decays. For

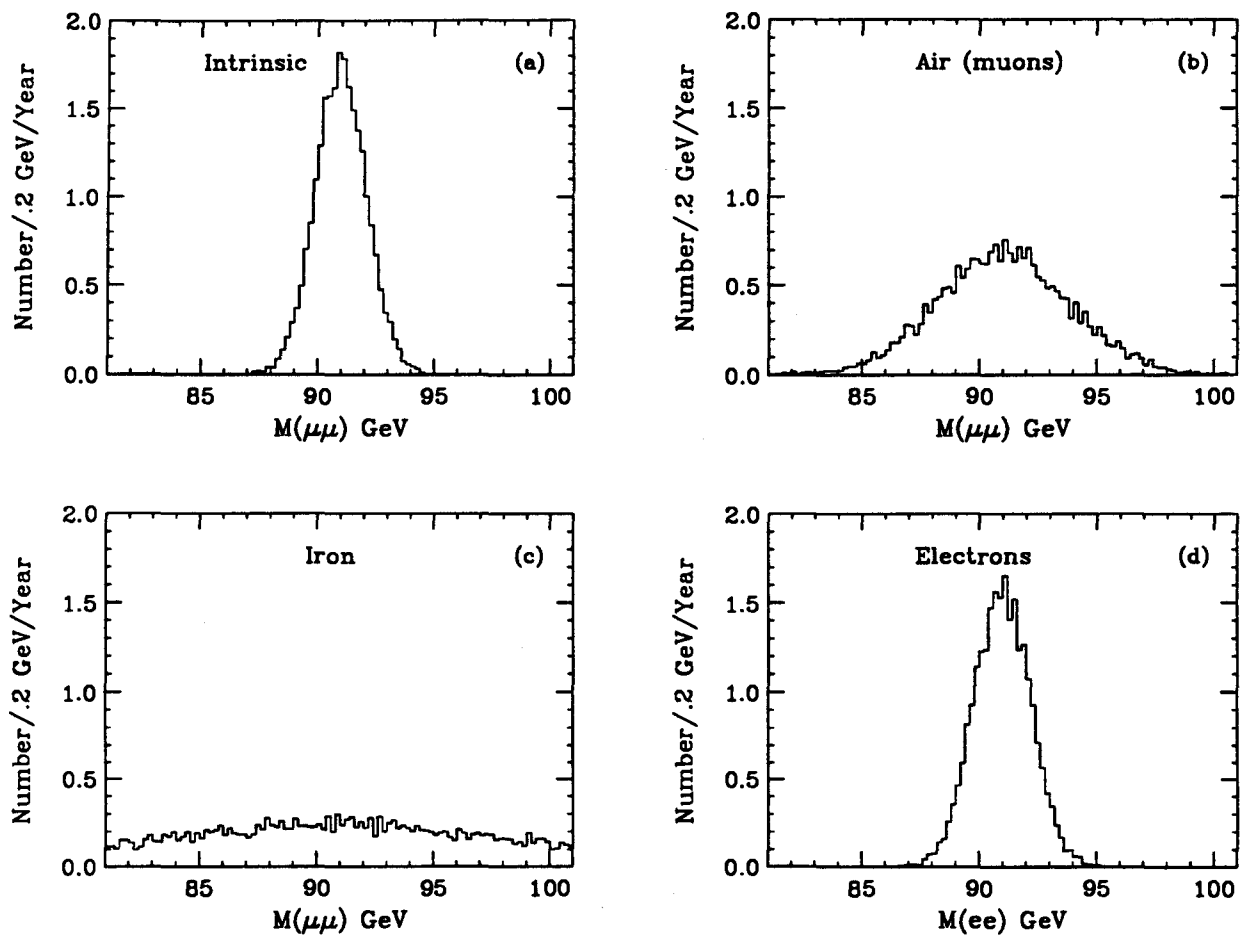

Figure 1-8 Reconstructed width of Z from 800 GeV Higgs decay to leptons. Shown in (a) natural width (b) width for muons using air toroids (c) width for muons using optimized iron toroids and (d) width for electrons.

comparison we include the resolution obtainable from an optimized system of iron toroids [14]—which would add 30 000 tons to the weight of the detector, decrease the efficiency for higher energy muons because of unobservable radiation losses, jeopardize the efficiency of the outer chambers, and raise the minimum energy of a detectable muon, degrading the efficiency and resolution for such processes as Higgs decays to ZZ*.

In conjunction with developments of the design, progress has been made in detector simulation and beam tests. A detailed simulation of radiation levels in the detector using GEANT and MARS10 [15] has identified major sources of backgrounds and raised confidence in the ability to run at 10^{34} $cm^{-2}s^{-1}$.

Calculations have provided valuable insight into hadronic punchthrough, electromagnetic backgrounds accompanying muons, muon energy loss in calorimetry, and optimization of the muon detector arrays. The ray tracing capabilities of the three-dimensional engineering models has been extended to allow comparisons of multiple scattering of muons to be directly compared to the bending provided by the toroids. Using data obtained from beam tests of TRD modules, simulation of performance gives added confidence in the ability to identify electrons and high-momentum muons. Excellent results have been obtained in test beams for SPACAL calorimetry, enhancing confidence in this technology [16]. Tests of new configurations of absorber and readout for liquid argon, indicate enhanced performance at high rates [17].

1.5 DETECTOR OPTIMIZATION

The detector designs presented in this document are intended to provide examples to illustrate the performance and the scope or cost of such a project. The expected performance is summarized with specifications listed in Table 1-1. It must be stressed that the example detectors presented here still require considerable effort in optimization, and in many cases demonstration of performance in beam tests and engineering prototypes. The examples are intended as an illustration of feasibility and to set a scope for the project. The optimization and the

Table 1-1 EMPACT/TEXAS Performance Summary

TRD/TRACKING			
Coverage*	$\eta < 2.5$		
Rejection	3×10^{-3} for $P\pi < 50$ GeV/c		
Efficiency	0.9 for Pe > 1 GeV/c		
Channels:			
TRD/Tracker		290 000	
Preshower		476 000	
Si. Pads SPACAL		30 000	
Si. Pads LAr		62 000	
Total Channels SPACAL			796 000
Total Channels LAr			828 000
CALORIMETRY			
Coverage	$\eta < 5.5$		
Depth	at $\eta = 0$	at $\eta = 3$	at $\eta = 5.5$
SPACAL	10.7 λ Active	14.0 λ Active	14.5 λ Active
	12.0 λ Total	14.0 λ Total	15.2 λ Total
LAr	10.3 λ Active	14.5 λ Active	14.5 λ Active
	11.6 λ Total	15.2 λ Total	15.2 λ Total
$\Delta\eta = \Delta\varphi$	at $\eta = 0$	at $\eta = 3$	at $\eta > 3$
SPACAL	0.05	0.14	0.2
LAr EM	0.035	0.035	—
LAr HAD	0.07	0.07	0.2
$\Delta E/E$ (GeV)			
SPACAL	$0.075/\sqrt{E} \oplus 0.005$ EM		
	$0.5/\sqrt{E} \oplus 0.01$ HAD		
LAr	$0.075/\sqrt{E} \oplus 0.005$ EM		
	$0.5/\sqrt{E} \oplus 0.01$ HAD		
Total Channels	SPACAL 26 500	LAr 118 000	
MUON SYSTEM			
Coverage	$\eta < 2.5$		
Bmax	1.5 T Central;	3.5 T Ends	
Field Integral	2.5 Tm at $\eta = 0$;	12 Tm at $\eta = 2.5$	
Stored Energy	0.8 GJ central;	0.5 GJ each end	
Number of Superlayers	120		
Alignment Accuracy	25 µm externa ; 50 µm internal		
Max Drift	1.25 cm		
Spatial resolution/plane	200 µm		
Measurement planes/track	28 Bend	10 Non Bend	
Total Channels	410 000		
$\Delta P/P$	4% 100 GeV; 7.8% 600 GeV		$\eta = 0$
	1% 100 GeV; 1.8% 600 GeV		$\eta = 2.5$
PHYSICAL PARAMETERS			
	Diameter(m)	Length(m)	Weight (MT)
TRD	2.0	6.0	1
SPACAL Calorimeter	7.8	16.6	2 378
LAr Calorimeter	8.0	16.6	3 075
Forward Calorimeter (ea.)	3.5	3.1	225
Central Toroid	16.6	16.6	797
End Toroid (ea.)	18.6	5.1	385
MUON Detector**	24.8	34.9	795
Total Detector Weight SPACAL			5 191
Total Detector Weight LAr			5 888

* η is written for $|\eta|$ everywhere in this document
** Includes alignment structure

iterations to be performed will use this scope and physics performance specification as a constraint, finding the best combinations of technologies and the optimal distribution of detector elements to maximally exploit the SSC physics.

This process of design optimization by iteration has been part of our method from the outset. The key missing ingredient from this process was a financial or scope constraint that has now been supplied by the SSC. This has provided the impetus for the new baseline detectors described in detail in this LoI. The remaining steps of performance and cost iteration must still be studied in far greater detail than has been done in the short interval available between EoI and LoI. This will involve progress towards the critical choice of calorimeter technology, which in turn will determine the final choice of tracking components and the relative reliance on preconverters, TRD, and vertex detectors. This optimization requires performance and cost data from all systems to be fully executed. This is a major function of the systems integration effort that will use systems codes available from industrial partners with expertise in major project design and management.

The collaboration has demonstrated its expertise and creativity in the original and descoped designs and will bring to bear the most advanced tools available for detector design, integration, simulation, and project management. The collaboration has been growing, and it is expected that if approval is granted, many additional physicists and institutions from the U.S. and abroad will be integrated into the effort.

The remainder of this document describes in detail the detector systems, the anticipated physics performance, and the cost basis for the proposed detector examples.

REFERENCES

1. "The EMPACT Experiment at the Superconducting Super Collider," SSC–EoI–0006 (1990). Hereafter EEoI in text.
2. "A Calorimeter-Based High-Rate Detector for the SSC," SSC–EoI–0011 (1990). Hereafter TEoI in text.
3. "10^{34}, An Expression of Interest," SSC–EoI–0007 (1990). Hereafter HLEoI in text.
4. Report of the 1990 HEPAP Subpanel on SSC Physics, DOE/ER–0434 (1990).
5. W. Marciano, Phys. Rev. Lett. **62**, 2793 (1989); W. Bardeen, C. T. Hill, and M. Linder, Fermilab–PUB–89/127–T; D. E. Kahana and S. H. Kahana, BNL-44380 (1990).
6. M. S. Chanowitz, "Electroweak Symmetry Breaking at the pp Colliders of the 1990's and Beyond," LBL–26613–MC (1989); M. S. Chanowitz, Annu. Rev. Nucl. Part. Sci. **38**. 323 (1988).
7. J. F. Gunion *et al.*, Nucl. Phys. **B299**, 231 (1988).
8. R. Kleiss *et al.*, preprint DTP/90/54 (1990).
9. J. F. Gunion *et al.*, Phys. Rev. **D40**, 2223 (1989).
10. D. Hertzog *et al.*, "Scintillating Fiber Calorimetry," in Proceedings of the Workshop on Radiation Damage to Plastic Scintillator," Tallahassee, Florida, March, 1990.
11. H. Burkhardt *et al.*, Nucl. Instrum. & Methods **A268**, 116 (1988).
12. R. Adair, "Iron Toroids," EMPACT/TEXAS Note 273 (1990).
13. L. Rosenson, "Studies of the EMPACT/TEXAS Muon Spectrometer Directed Towards Robustness and Descoping," EMPACT/TEXAS Note 354 (1990).
14. G. Hanowski *et al.*, "Design of an Iron Core Toroid for EMPACT/TEXAS," EMPACT/TEXAS Note 361, November 1990.
15. I. L. Azhgirey and N. V. Mokhov, "Radiation Doses and Background Particle Fluxes in EMPACT Experiment at the SSC," EMPACT/TEXAS Note 329 (1990).
16. R. Wigmans, Fort Worth Symposium on Detector R&D for the SSC (1990).
17. B. Aubert *et al.*, "Liquid Argon Calorimetry with LHC-Performance Specifications," CERN/DRDC/90-31 August 1990.

2.0 CALORIMETRY

2.1 INTRODUCTION

The calorimeter is the crucial element of the EMPACT/TEXAS detector. Calorimetry identifies and measures photons, electrons, muons, jets, and by missing p_T, neutrinos. Scintillating fiber (SPACAL) and liquid argon (LAr) calorimetry will meet the physics requirements. Detailed designs are presented and a focused program of research and development (R&D) to optimize these technologies is outlined. The forward calorimeter presents a special challenge because of the high radiation levels, but viable solutions exist. We intend to choose the technologies for the SSC proposal over the next year based on the demonstrated physics performance, technical assessment, and cost.

2.2 PHYSICS REQUIREMENTS

The physics requirements for calorimetry are summarized in Table 2-1, and some of the more salient issues are discussed briefly below. The radiation doses have been calculated for our geometry, and have been found to be less demanding than estimated in our EoIs [1]. The dose is maximal for a very small area of the end cap calorimeter near $\eta \sim 3$ where it reaches ~ 10 Mrad/year at 10^{34} $cm^{-2}s^{-1}$ as shown in Fig. 2-1. The forward calorimeter must withstand more than 1 Grad at small radii as shown in Fig. 2-2.

Electrons, muons, and jets above 20 GeV are required to be timed to the bucket in which they were produced. This requirement and pile-up considerations require fast response, especially for high-luminosity operations. Integration time should cover a minimum number of beam crossings.

A significant improvement over that of the EEoI in the electromagnetic (EM) calorimeter resolution has been implemented, extending its capability to find an intermediate mass Higgs. With the resolution described as $\sigma_E / E = A / \sqrt{E} \oplus B$ (where $\oplus$ indicates the terms add in quadrature), the specification is $A \leq 7.5\%$ and $B \leq 0.5\%$. As shown in Sect. 6, this is sufficient to find a Higgs in the mass range between 80 to 180 GeV through its $\gamma\gamma$ or $Z Z^*$ decay modes. We have calculated [2] the effect of the sampling term A on the significance of the $H \rightarrow \gamma\gamma$ signal for a 120 GeV Higgs. Some of the results are shown in Fig. 2-3, and they indicate that discovery is viable for $M_H >$ 110 GeV in one year at $L = 10^{33}$ $cm^{-2}s^{-1}$ with A = 7.5% and in somewhat longer periods for lower mass.

Table 2-1 Calorimeter Requirements

Attribute	Physics Requirements	Specification
Survivability	$10^{34} cm^{-2} sec^{-1}$/year	
EM		< 10 Mrad
HAD		< 1 Mrad
Forward		< 3 Grad
Dynamic Range		
EM	Low - 50 MeV Shower Tails High- 5 TeV Z'	10^5
HAD	Low - 3.5 GeV μ High- 15 TeV Jets	10^4
Energy Resolution		
EM	$H \rightarrow \gamma\gamma$	$\frac{7.5\%}{\sqrt{E}} \oplus 0.5\%$
	$\Gamma_{Z'}$	$\frac{15\%}{\sqrt{E}} \oplus 1\%$
HAD	$Z \rightarrow j j$	$\frac{50\%}{\sqrt{E}} \oplus 2\%$
	Compositeness	$\frac{50\%}{\sqrt{E}} \oplus 2\%$
Time Resolution		
EM	e, γ, μ	< 16 ns
HAD	jet, μ	< 16 ns
Noise		
EM	e/γ Isolation	$\Sigma E_T < 5$ GeV in $\Delta R = 0.2$
Depth		
EM	Resolution	25-30 X_0
HAD	Punchthrough	11-15 λ
Hermeticity	$H \rightarrow l l \nu \nu$	$\Delta p_T <$ υ Bkgd $\eta \rightarrow 5.5$
Segmentation		
EM	$\Delta x \sim 1$ mm, $\pi^{\pm}/\gamma$ Overlap	$\Delta\eta = \Delta\varphi \leq 0.05$
HAD	$Z \rightarrow j j$	$\Delta\eta = \Delta\varphi \leq 0.1$

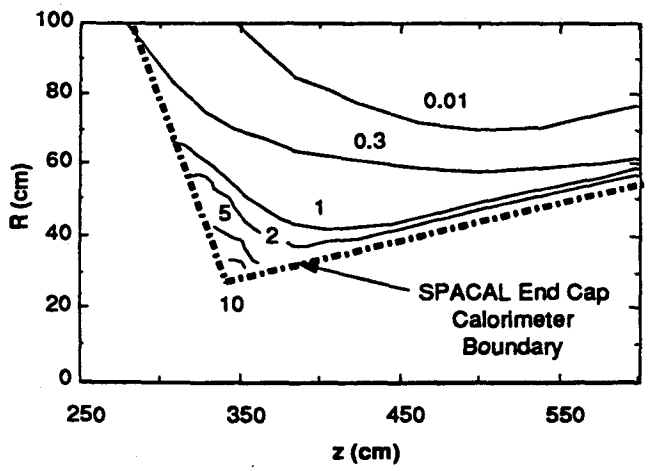

Figure 2-1 Radiation doses for 1 year at 10^{34} $cm^{-2}s^{-1}$ for the end cap calorimeter of the EEoI (doses are in Mrad and assume lead and scintillator [1]).

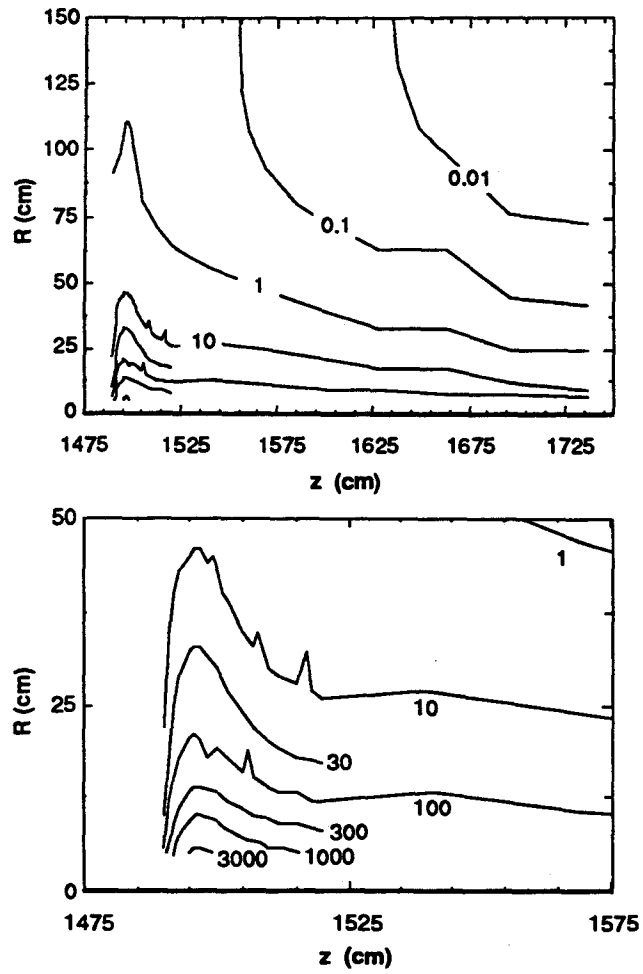

Figure 2-2 Radiation doses for 1 year at $10^{34}cm^{-2}s^{-1}$ for the forward calorimeter of the EEoI (doses are in Mrad and assume lead and scintillator [1]). Lower plot is an enlargement of a section of the top plot.

For the calorimeter transverse segmentation, we have chosen $\Delta\eta = \Delta\varphi = 0.05$ for the EM and hadronic (HAD) sections of the SPACAL option, while for LAr we have chosen $\Delta\eta = \Delta\varphi = 0.035$ for the EM section and $\Delta\eta = \Delta\varphi = 0.07$ in the HAD section. Experience with the NA34 liquid argon calorimeter has shown the value of small (2 cm) EM pads for electron identification near a jet. The calorimeter must be able to resolve single muons, and the dynamic range and noise specifications are consistent with this requirement. The active depth is 10.7 λ near $\eta = 0$, growing to 14 λ at $\eta = 3$. The shower centroid resolution is set by the $\pi^{\pm}/\gamma$ overlap background for electrons. While the preradiator provides some redundancy for this, the proposed segmentation provides position resolution of about 1 mm. The hermeticity requirement is set by the magnitude of the irreducible missing E_T from neutrinos, requiring the calorimetry to cover $\eta < 5.5$. Further, to maintain a calorimeter resolution with a constant term of 0.5% requires that the energy scale of each cell be known at this level.

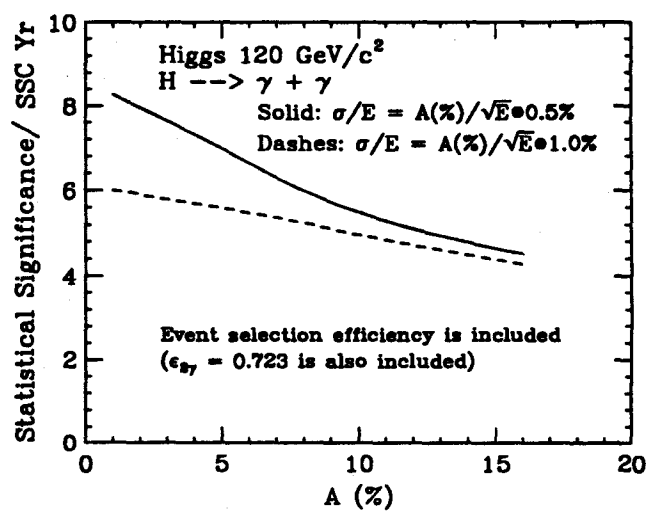

Figure 2-3 Statistical significance for $H \rightarrow \gamma\gamma$ vs sampling term for integrated luminosity of 10^{40} cm^{-2}.

2.3 SCINTILLATING FIBER CALORIMETRY

2.3.1 Baseline Design

Scintillating fiber calorimetry, while a relatively new development, has shown dramatic progress within the last few years. The SPACAL group [3] has demonstrated the speed, compensation, uniformity of response as function of impact point and angle, energy resolution, and $e/\pi^{\pm}$ separation that can be obtained with a scintillating fiber calorimeter, while in the U.S. the SSCintCal group [4] made progress in scintillating fiber construction techniques and radiation hardness studies. Both the EEoI and TEoI included scintillating fiber calorimeters as options, and emphasized the capability of this technique for achieving our common physics goals.

The hermetic arrangement of uniform, projective SPACAL towers is designed for uniform response to decrease backgrounds for missing E_T measurements. Compensated calorimetry is helpful for energy measurements of jets and for invariant mass reconstruction from jet energy measurements. The inherent speed of scintillation light production and collection satisfies the speed requirements.

To provide the capability for detection and measurement of an intermediate mass Higgs boson through the $H \rightarrow \gamma\gamma$ decay mode, it was found to be necessary to separate the EM and HAD sections of the SPACAL calorimeter so that each section can be optimized separately. Measurements [5] have shown that e/π = 1.05–1.10 for a fiber-to-lead volume fraction 1:4. To adjust this ratio to be closer to 1.00, the fiber fraction must be reduced. We have chosen fiber:lead = 1:5. The EM section is designed to achieve a resolution of $\sigma_E/E = 7.5\%/\sqrt{E} \oplus 0.5\%$ mainly through finer sampling with smaller diameter (0.5 mm) fibers. An extrapolation of SPACAL measurements with 1 mm fiber gives us confidence that this resolution can be achieved (see Sect. 2.3.2).

Some downscoping of the calorimeters envisioned in the EoIs has been necessary. In particular, the calorimeter segmentation is now 0.05×0.05 (4 times as large as the TEoI). Additional cost savings result from the change in fiber : lead ratio, and from the use of 3 mm diameter fibers in place of the 2 mm diameter fibers originally planned for the HAD calorimeter compartment.

The EEoI and TEoI, cost estimates for scintillating fiber calorimeters are based on experience with laminated prototypes along the lines developed by the SPACAL [3] and JETSET [6] groups. Extensive design studies of this and the alternative technology of low-melting-point casting have resulted in significant cost savings. The latter would use low-melting-point lead alloys. These techniques have been demonstrated with small prototypes, and the development of large-scale cast prototypes for a high-energy test beam study is currently underway [4].

For the baseline design, separate EM and HAD sections will be used. They are optically coupled through mass fiber splice joints, and mechanically coupled with optical epoxy [7]. Effective longitudinal segmentation is achieved through the separate readout of fibers that go through the entire HAD section and EM section, and fibers, which because of the projective geometry, only extend through the HAD section. This arrangement is indicated for a representative tower near $\eta = 0$ in Fig. 2-4.

EM calorimeter sections use 0.5 mm diameter scintillating fibers arranged in a rectangular lattice, with a volume ratio of 1 part plastic fibers to 5 parts lead/bismuth alloy. This alloy is a dense (9.6 g/cm^3), low-melting-point (70°C) eutectic mixture with an extremely small thermal coefficient of expansion and other desirable mechanical properties. A small constant term in the energy resolution of this device is achievable through a combination of the following: regularity of the fiber lattice; uniformity of the absorber density; uniformity of the light yield from individual fibers and of the optical coupling efficiencies; rotating the fiber axes by at least 5° from the incident particle axis; mixing of light from different parts of the calorimeter to more uniformly illuminate the face of readout photomultiplier tubes (PMT); and smoothing the response across tower boundaries.

Each EM section is followed by a HAD section consisting of 3 mm diameter fibers and lead alloy in the volume ratio 1:5. These fibers will be exactly projective and have no mirroring on the front ends because of the larger attenuation lengths expected for 3 mm fibers. Fibers will end flush with the lead at the readout side and will be coupled through an optical fiber bundle to photomultipliers. Each fiber bundle is embedded in lead to increase the shielding of the muon chambers. The assembly of integrated towers and their installation into a complete calorimeter is illustrated in Fig. 2-4. Properties of the design are listed in Table 2-2 and Fig. 2-5.

A preliminary manufacturing design for all components of the scintillating fiber calorimeter has been developed [7]. For EM and HAD sections, fibers are fed in parallel from large numbers of spools through die-cast precision positioning plates.

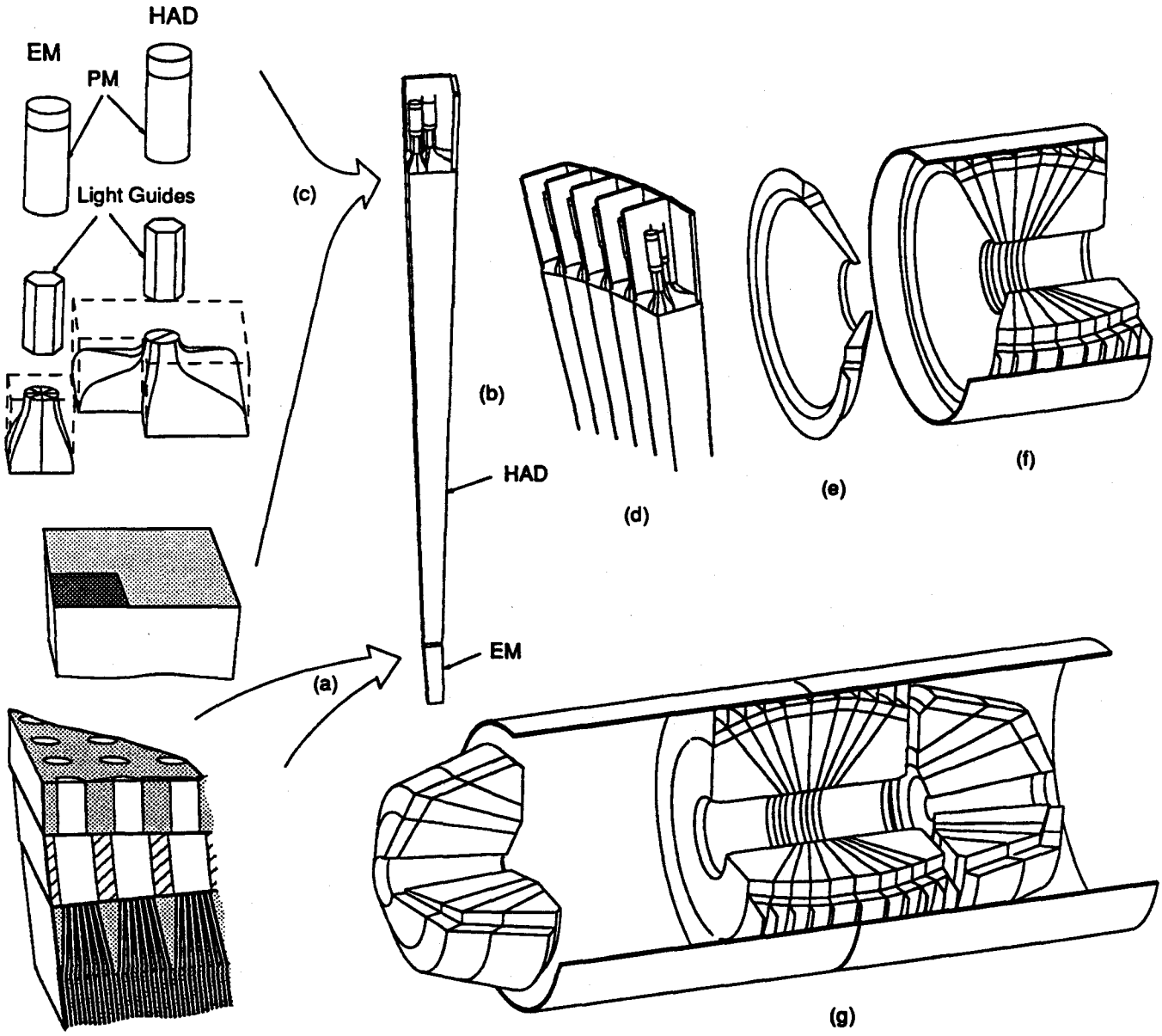

Figure 2-4 Construction details of the SPACAL design. (a) Coupling of 0.5 mm EM fibers to 3 mm HAD fibers; (b) single tower; (c) coupling of fibers to PMTs, dashed area will be filled with lead alloy; (d) ring detail; (e) super-ring; (f) central barrel; (g) full calorimeter.

Table 2.2 Specifics of SPACAL design

	EM Section	Hadronic Section	Total
Total X_0	30		
Active Thickness (λ)			10.7 ($\eta = 0$) 14 ($\eta = 3$)
e/μ	0.67	0.67	
$\Delta\eta \times \Delta\varphi$	0.05 x 0.05	0.05 x 0.05	
Thermal Noise	< 5 MeV	< 5 MeV	
Number of Channels	11 482	14 982	26 464
Fiber	0.5 mm	3.0 mm	
$X_0 = 0.82$ cm $\lambda = 22$ cm			Weight (MT) 2379

For the EM portion of the tower, the fibers are first fixed in place by one low-melting-point alloy, then immersed in a second such alloy with a lower melting point. By only threading fibers once during the setup for fabrication of a large number of towers, a high-volume production process is developed that minimizes setup and handling. The HAD sections are cast into a large form and then are slowly extracted while solidifying, forming a continuous production process. Sections of the proper length are then cut and machined into shape. The two parts of the tower are then optically and mechanically integrated with radiation hard-epoxy bonds. Epoxy is also used to bond towers into rings, and rings into "super-rings," each time generating a stable and self-supporting structure.

Radiation damage is a key issue for scintillating fiber calorimetry, and the radiation hardness of fibers has greatly improved over the last few years

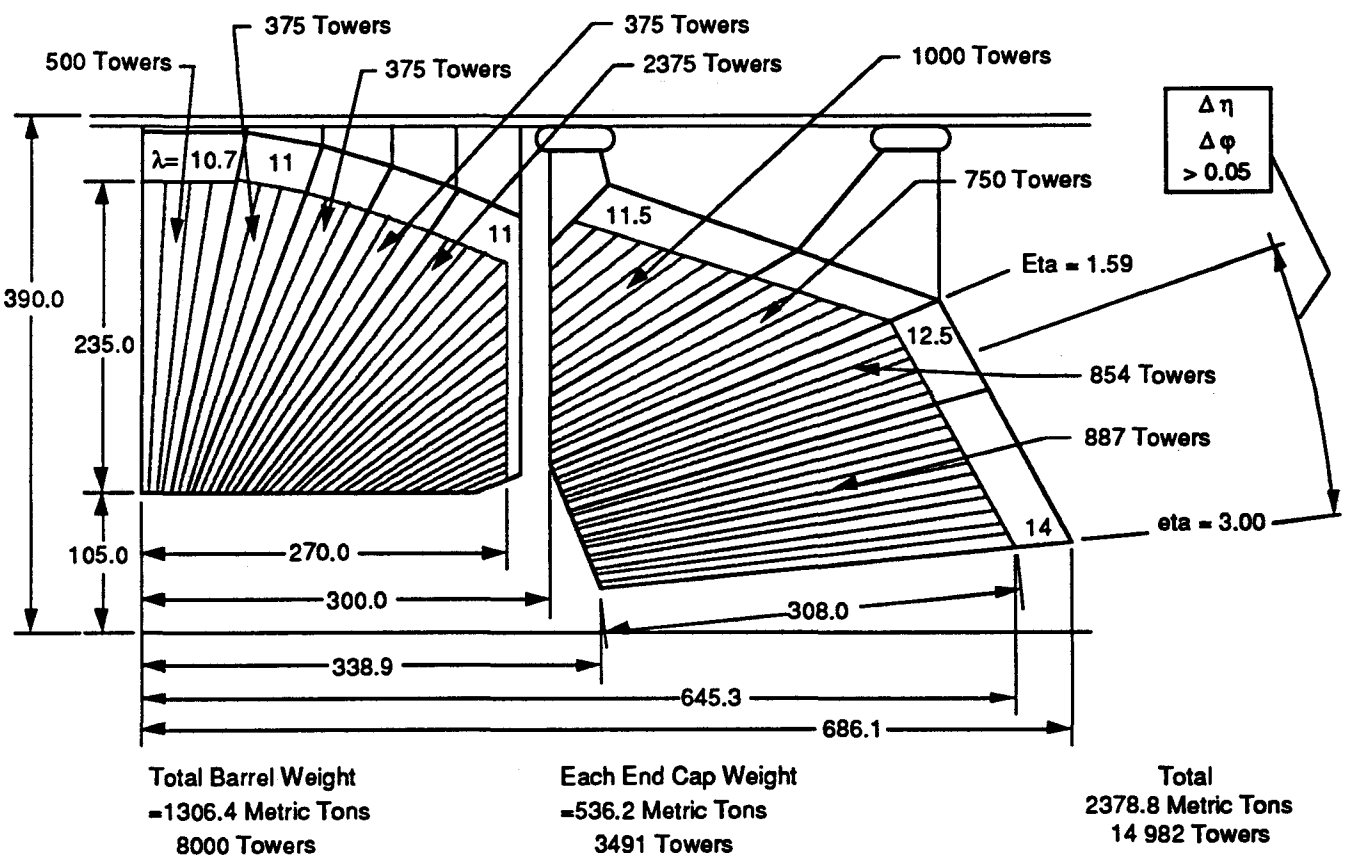

Figure 2-5 Quarter section of baseline SPACAL option (dimensions in cm).

and is still improving. Existing plastic scintillating fibers have been demonstrated to withstand integrated doses of more than 1 Mrad within calorimeter modules, even before accounting for annealing and recovery [8]. This is already sufficient for most of the calorimeter (see Fig. 2-1), while further progress is expected to extend the reach of this technology to more forward regions.

A calibration beam at the SSCL will be used to obtain absolute calibration of some of the completed EM calorimeter modules in the 2–3 years before pp operation commences. This calibration will be used as a measurement of variation between towers and to provide an initial calibration. The EM sections of the calorimeter will be calibrated *in situ* by using $Z \rightarrow ee$ decays from pp interactions. Inclusive Z production rates are sufficient to give over 10^6 dielectrons per SSC year in the barrel calorimeter alone ($|\eta|<1.5$). With cell size 0.05×0.05, this is about 500 e's per cell. The Z mass should then be determined with a precision of about 100 MeV per cell per year, well under the 0.5% requirements. All EM cells will be calibrated this way and with the absolute scale fixed using M_Z. The beam-calibrated modules will be a reference and starting point.

The absolute calibration requirements for the HAD section are not as stringent as for the EM section. It is planned to calibrate some of the detector modules in the test beam and to cross calibrate the remainder by E_T balance and energy flow uniformity. The calibration will be fixed with respect to the EM section using QCD events with a single photon recoiling against a HAD jet. This technique has been demonstrated to be effective by CDF [9].

Calibration of time-dependent variations of scintillating fiber calorimetry is accomplished through three basic methods: (1) radioactive sources, (2) UV and visible light sources, and (3) beam signals. UA2 [10] and CDF [11] have shown that this combination can give calibration with a precision of 1.0%. A set of fixed and moveable radioactive sources will be built into the calorimeter structure. The performance of the optical components of the readout chain, including photomultiplier gains, light transmission, and time offsets, are best monitored and controlled through a UV laser-based light pulsing system. The optical stability required here has been achieved in other large experiments [12], so that with proper care the systematic error requirements of the EM section are manageable.

2.3.2 Recent R&D Results

In addition to the published results available at the time of our EoIs from the SPACAL collaboration [3], there are now new beam test results from the operation of a 13 ton (instrumented) SPACAL prototype [5], as seen on the separator tab. This prototype has a diameter of 5.5 λ and a depth of 9.5 λ, which is large enough to contain HAD showers. It was constructed of 1 mm diameter fibers and lead in the volume ratio 1:4. Beam tests were performed with electrons and pions in the energy range 5–150 GeV, as well as with "jets" (simulated by placing a thick target in the test beam upstream of the calorimeter at two different distances).

New information learned in these tests that is relevant to the calorimeters being proposed follows:

1) **Compensation**—The measurement of e/π, as mentioned in Sect. 2.3.1, was between 1.1 and 1.05. It is anticipated that it can be more nearly 1.0 by reducing the volume ratio of scintillating fiber to lead from 1:4 to 1:5.
2) **Hadronic Energy Resolution**—Hadronic energy resolution for single pions is measured to be $\sigma_E/E = 28.9\% / \sqrt{E} + 2.6\%$. The constant term is about 1.5–2% for "jets" and is understood to result about equally from the attenuation of light in the fibers and $e/\pi \neq 1.00$. It is expected that the constant term for jets will be about 1% when the e/π ratio is changed to 1.00 (see item 1).
3) **Electromagnetic Energy Resolution**—The EM energy resolution is measured to be $12.4\% / \sqrt{E} + 1.3\%$, consistent with other published results. The constant term in the EM resolution is caused by the measured ±1% variation in the sampling fraction as the impact point of electrons is changed over the equilateral cell. The stochastic term and the

constant terms are measured to be reduced by about 20% if the angle between incident electrons and the fiber axis is increased from 3° to 5°. Also, the constant term is expected to be reduced if the fiber diameter is reduced from 1 mm to 0.5 mm, because four times more fibers then participate in the shower development.

4) **Signal Speed**—The e/π ratio and HAD energy resolution have been measured as a function of the ADC gate width at 80 GeV—both reach their final values for gate widths as short as 35 ns.

5) **Electron-Pion Discrimination**—A careful study of electron-pion discrimination using the SPACAL array of monolithic towers has been carried out. Several techniques using the lateral shower spread or time development of the showers have already demonstrated the ability to identify isolated electrons. Studies are underway to develop similar techniques for finding electrons in or near jets [13].

2.3.3 Future R&D

Having selected low-temperature casting with separate PMT readout of EM and HAD sections as the production technique of choice, there must be a demonstration that the performance that has been achieved with laminated devices can be preserved and extended. In addition to constructing and testing of full-scale prototypes, there must be greater understanding and control of radiation damage processes, more detailed designs for readout and calibration systems, further development and testing of the methods for calorimeter mass production, and a detailed engineering design that provides structural stability while facilitating assembly and access.

The baseline production design for cast fiber calorimeters contains some novel techniques that will require experimentation to optimize fixturing, tooling, choice of materials, and to better estimate production rates and dimensional tolerances. The integration of EM and HAD sections into an optically linked tower requires uniform mass-coupling splices of many fibers, and the performance of these couplings must be tested in real devices. This work must be carried out in concert with simulations and physics studies to determine specifications for device uniformity, geometry, and composition through a cost and benefit analysis.

Because of the special importance of electrons and photons to the physics goals of the detector, it is important to pursue alternative approaches to the baseline EM calorimetry, all of which are to be tested in front of the 13 ton SPACAL prototype.

1) One option being considered is the readout of 0.5 mm scintillating fibers at the boundary between EM and HAD calorimeter segments with vacuum phototetrodes. The tetrodes would be complemented by bipolar-shaped amplifiers, optimized for low noise. This option preserves compensation in the EM section and gives unambiguous longitudinal segmentation. The consequences of particles from HAD showers traversing the electrode structures of the tetrodes must be investigated. It is planned to build a few small EM modules with tetrode readout and test them both normal and reversed (the tetrode in front).

2) Another variation being investigated is increasing the fiber packing fraction from 1:5 by volume to 1:1 by volume, as in JETSET [6], and using 1 mm diameter scintillating fibers. Readout would be performed with phototetrodes as above. This increases the light yield and should decrease the constant term if fiber spacing and uniformity are well-controlled. The consequent loss of compensation in the EM section will be tested.

3) Studies are underway to investigate the replacement of the SPACAL EM section with a silicon option with either lead or tungsten absorber, as in the EEoI. The sampling frequency is chosen so as to obtain an energy resolution of $< 10\% / \sqrt{E}$.

Selection of compatible materials with appropriate mechanical, optical, and radiation-hardness properties will require careful study. Radiation damage has a complex and profound dependence on choices of materials and production techniques. The complex issues of radiation chemistry; the role of the gas atmosphere and, in particular, oxygen in the annealing process; and the effect of calorimeter construction techniques on the radiation hardness of the resultant modules all require further study. Substitution of 115° C Pb/Bi alloy for the 70° C Pb/Bi/Sn/Cd alloy, for example, eliminates neutron-absorbing cadmium and provides a path for oxygen to reach fibers (because fibers must be inserted into holes in a previously cast block), but somewhat complicates the fabrication process. Similarly, the selection of the best radiation-hard epoxy with desirable mechanical and optical properties requires investigation. Prototype calorimeter towers with various test fibers will be irradiated. Long-term exposure of calorimeter modules through gradual irradiation over many months is planned, including measurements of the demonstrated capacity of plastic scintillating fibers for annealing and recovery.

This program of test beam work will require electron, pion, and muon beams at high and low energy. The program will also require high-intensity beams for radiation studies.

A full design of a scintillating fiber calorimeter will require a number of thorough studies that have thus far received only preliminary work. Tolerances in the fabrication of individual towers and in their assembly must be accounted for together with the physics consequences of cracks and nonuniformities. Also, a more detailed design of support structures, readout systems and cables, calibration hardware, and provisions for assembly and access must be made. Experience with prototype devices must be used to optimize production techniques, form better estimates of production schedules, and determine the structural integrity of fiber towers and their support structures.

2.4 LIQUID ARGON LEAD CALORIMETER

2.4.1 Baseline Design

LAr calorimeter technology is a relatively mature field. However, there are still details that need to be explored to optimize the system. Its established features—radiation hardness, ease of calibration, cost effectiveness, and long-term operating experience—make it an attractive technique for the SSC. The EEoI proposed the use of uranium plates as the radiator material because of the uniform response to electrons and pions [14]. However, in downscoping the calorimeter design, the baseline absorber has been changed from uranium to a lead-steel sandwich material that appears to be a reasonable and affordable alternative. The unit cells now proposed are shown in Fig. 2-6 and the basic properties are listed in Table 2-3.

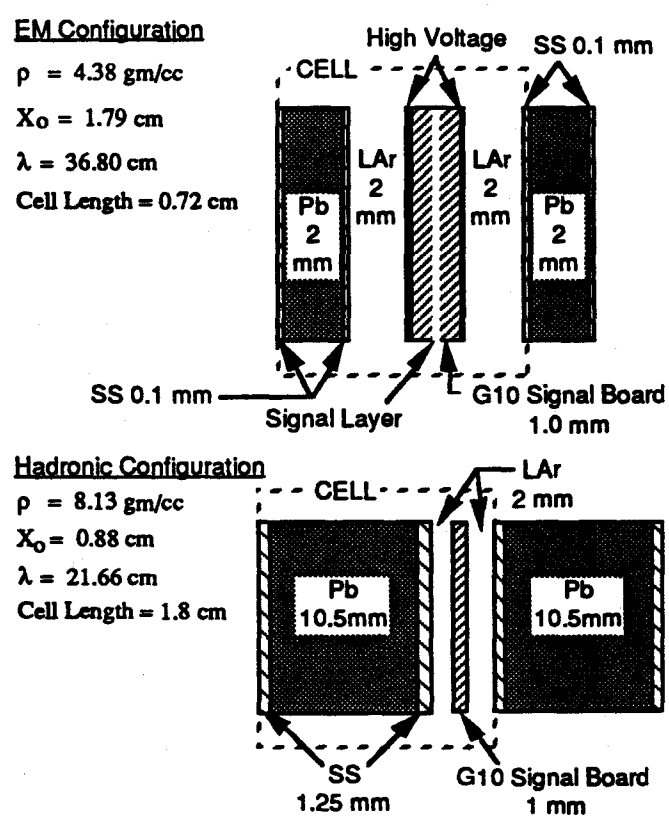

Figure 2-6 Unit liquid argon calorimeter cells. Honeycomb is used in argon gaps.

Table 2.3 Specifics of Liquid Argon Design

	EM Section	Hadronic Section	Total
Total X_0	25	225	250
Active Thickness (λ)	1.212	9.11 (90°)	10.34 (η = 0) 14.5 (η = 3)
e/μ	0.77	0.635	
Sampling Fraction	0.213	0.0482	
$\Delta\eta \times \Delta\varphi$	0.035	0.07	
Thermal Noise in ΔR = 0.2 (100 ns) (in GeV)	0.15	1.60	1.61
Number of Channels	56400	61920	120,320
	X_0 = 1.79 cm λ = 36.8 cm	X_0 = 0.88 cm λ = 21.66 cm	Weight (MT) 3075

The basic cell of the HAD section is comprised of a lead steel sandwich 13 mm thick followed by a 2 mm LAr gap, a 1 mm G10 readout board, and another 2 mm argon gap. The change from uranium to lead reduces the overall density by ~20%, and may affect the e/π and energy resolution. This configuration should still provide 50%/$\sqrt{E}$ HAD resolution and the required thickness for total shower absorption although a larger radius is required. While the e/π ratio has not been well measured in a lead calorimeter, we believe it to be about 1.2 at 11 GeV from SLD measurements [15]. Calculations support a similar value [16,17]. The LAr subsystem group will make a precise measure of e/π with 12 mm lead plates next spring, with the apparatus shown on the separator tab. One may perhaps improve e/π by suppressing the electron response through the use of an optimal thickness of iron cladding on the lead plates [16]. The addition of allene may boost the HAD response compared to the electron response [18]. Both approaches will be tested in the LAr subsystem tests [19].

The modules being designed are similar to the SLD style except that the transitions between them are nonprojective to eliminate cracks. To obtain sufficient EM resolution to search for $H \rightarrow \gamma\gamma$, we have reduced the thickness of the EM absorber plates to 2 mm; NA34 [20] has achieved a resolution of 7.5%/$\sqrt{E}$ and a systematic term of 0.5% with a similar arrangement of plates. To properly weight the energy lost in the 4.1 cm (η = 0) and 6.1 cm (η = 2) aluminum in the vacuum and argon vessels, the appropriate number of massless gaps at the front of the EM calorimeter will be added electrically to the first EM longitudinal sample. The first HAD section following the EM is ~20 X_0 deep so that any energy leaking into the HAD section would be added. A calculation has shown that using silicon pads just in front of the cryostat, massless gaps, and the HAD section preserves the energy resolution (Fig. 2-7) [21].

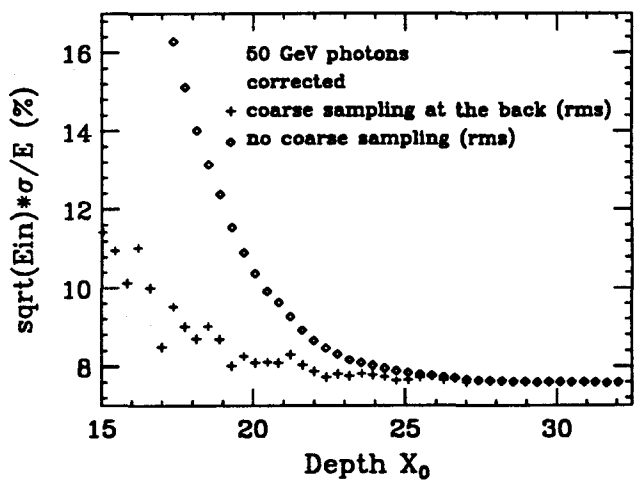

Figure 2-7 Energy resolution for 50 GeV γ vs depth for the LAr baseline calorimeter including corrected energy from the silicon pads in front of the cryostat, and the massless gaps in front of the EM. The diamonds represent the resolution without the addition of the first HAD section energy; the pluses include the first HAD section energy.

Quantitative studies of the speed of response achievable in liquid argon calorimeters and the pileup effects at luminosities from L =10^{33} to 10^{34} $cm^{-2}s^{-1}$ have been performed [22]. The key findings in these studies are:

1) An integration time (or charge measurement time) of t_m = 48 ns (three bunch crossing intervals) is realistic for hadron calorimeters on the basis of the charge transfer time from the electrodes to the amplifiers and of the fraction of the induced charge observed to

obtain a sufficient signal-to-electronic noise ratio. Pure liquid argon operated at a low electric field of 10 kV/cm (2 kV on a 2 mm space between electrodes) is assumed. The resulting calorimeter response has an effective width of ≈ 5 bunch crossing intervals. This bipolar shaping is equivalent to gated integration of the signal from a scintillator calorimeter for $2.5 \times 16 = 40$ ns, and integration (averaging) of the baseline for 40 ns. For purposes of determination of the pileup noise, these two gates are equivalent to an overlap of events from five bunch crossings.

2) The effect of pileup caused by minimum bias and two-jet events and of the electronic noise has been evaluated for typical calorimeter configurations and sampling ratios (11 λ deep with a sampling ratio 5% in the hadronic part). For a trigger tower of $\Delta\eta = \Delta\phi = 0.32$, the standard deviation in transverse energy, at $\eta = 0$ varies from $\sigma(E_T) \approx 1.3$ GeV at $L = 10^{33}$ $cm^{-2} s^{-1}$ to 2.6 GeV at 10^{34} $cm^{-2}s^{-1}$. These values decrease significantly as η increases. The timing uncertainty is $\sigma_t E_T \approx 75$ GeV ns at $\eta = 0$. Thus the assignment of energy to a particular bunch crossing will have uncertainties of 1 ns and 3 ns at 75 GeV and 25 GeV respectively. These values also decrease as η increases.

3) EM sections have a lower capacitance and a higher sampling ratio (larger signal), and they can be operated with shorter signal processing times. An integration time of $2 \times 16 = 32$ ns, and an effective width for pileup of less than $4 \times 16 = 64$ ns has recently been shown to be practical. This may be of particular interest for high-resolution, high-granularity EM calorimeters in the forward direction.

The new arrangement of the central and end calorimeters is shown in Fig. 2-8 [23] with properties listed in Table 2-3. The barrel has become slightly longer and deeper than in the EEoI. This is done to optimize the total weight because the end calorimeter can be made slightly smaller in radius by making the barrel longer. We have not performed a complete engineering design of the new configuration, but are confident, on the basis of our past work [24], that the design is viable from structural, thermal, and assembly points of

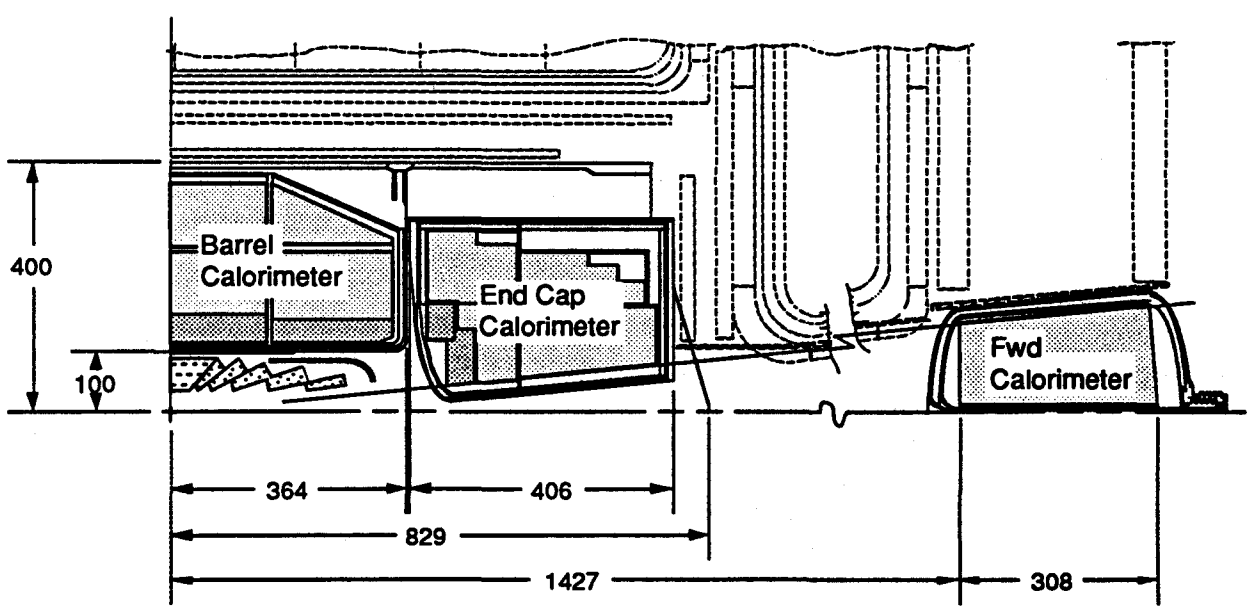

Figure 2-8 Quarter section of LAr baseline (dimensions in cm).

view. The number of active and total absorption lengths versus η is shown in Fig. 2-9. This has been derived from the 3-D CAD model of the calorimeter. The resulting resolution is displayed in Fig. 2-10, calculated as we have in the past [24]. The transition between the central and end calorimeters has been shown not to degrade the missing p_T performance of the calorimeter, although the $\eta = 3$ transition could be more of a problem not unique to LAr (see Sect. 6.3.1.6). The forward calorimeter must be located at a substantial distance from the end cap calorimeter to reach a coverage out to $\eta = 5.5$ (if closing the end calorimeter down to the beam, the coverage would only be to $\eta = 4$). Also, by withdrawing the forward calorimeter, the radiation dose to most of the forward calorimeter is reduced.

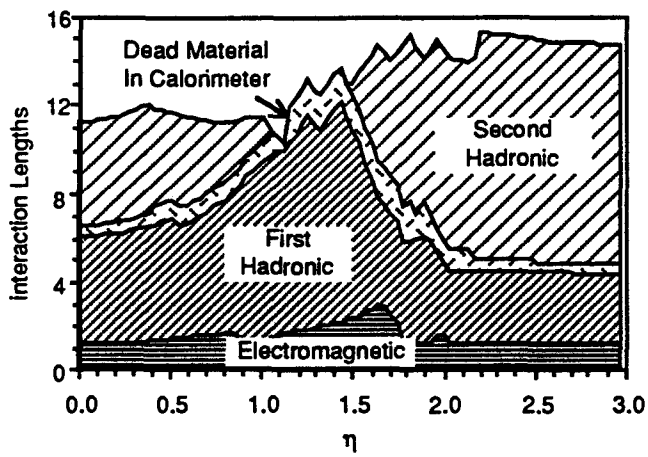

Figure 2-9 Active and total absorption lengths vs η for the LAr option.

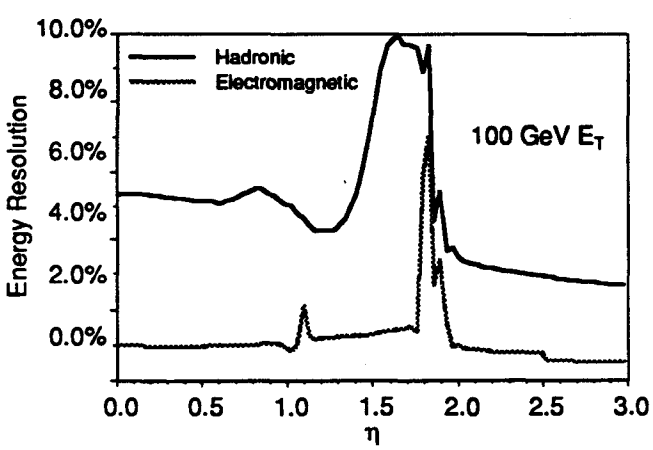

Figure 2-10 Fractional energy resolution for the LAr design for 100 GeV p_T hadrons and electrons.

2.4.2 Recent Progress and Future R&D

A new concept for LAr calorimetry called the "accordion" has been beam tested [25]. This idea optimizes the speed and hermeticity of a calorimeter by using the signal boards to transport the charge longitudinally in the calorimeter to the preamps. This allows low inductance ganging of connections to be easily achieved. The EM prototype tested at CERN this last summer had extraordinary performance. The energy resolution for electrons using 2 mm lead plates clad with 0.1 mm stainless steel was measured to be $(10.2\% \pm 0.5\%)/\sqrt{E} + 0.03\% \pm 0.05\%$. The position resolution for 125 GeV electrons was measured to be 0.700 ±0.015 mm. The signal/noise for minimum ionizing particles was 30/1—with 100 ns shaping. While the baseline is still a parallel plate stack, the design of a projective accordion stack has been started.

Progress on a concept called BRITE PADS has also been reported recently [26]. This idea uses shaped pads capacitively coupled to finely pitched strips that reduce the number of separate readout channels, while at the same time giving better resolution. A bench test of a prototype system gave promising results. Such a system could have significant effect on the cost and performance of the calorimeter.

We are also looking into the possibility of replacing the G10 in the EM section with lead tiles. These tiles would be bonded to the honeycomb spacing material for strength and positioning. If this can be achieved, then the EM section can be reduced by 33% in thickness and the EM resolution improved even further.

Other R&D projects are underway including studying requirements of cooling of the preamps, developing high-density feedthroughs, and detailed design of the modules.

2.5 FORWARD CALORIMETER

Many physics signatures relying on detection of missing energy and tagging of forward jets—such as $H \to l\,l\,j\,j$, $H \to l\,l\,\nu\,\nu$, $H \to l\,l\,\tau\,\tau$, and SUSY—require a high-quality forward calorimeter system. These regions present some formidable problems that must be considered carefully in designing an

optimal system. The forward calorimeter region has the largest rapidity coverage per unit area (and per shower size), must withstand the most intense radiation doses, and must deal with energies approaching the beam energies of the colliding protons. As a result of these rather severe performance criteria the technology choice for calorimetry in this region is likely to be quite different from those presented in the preceding sections.

We consider liquid argon as a credible baseline choice that will function in this region. However, care must be taken to position the preamps outside of the small high-radiation volume (Fig. 2-2). Lead is the default absorber, but studies will be done to verify its performance.

We are pursuing alternative technologies that hold much promise: liquid scintillator-filled fibers, high-pressure gas, and radiation-hard crystals.

2.5.1 Liquid Scintillating Fibers

One strong contender for solving these technical problems is the liquid-filled capillary calorimeter module (CAPCAL) that uses scintillating liquids contained in radiation-hard capillaries, which are then embedded in a high-density absorber, either lead or tungsten. Liquid scintillators have been observed to withstand higher doses of radiation than their solid counterparts [27] with comparable light outputs. Further, these liquids offer the possibility of being circulated through the forward calorimeter module, where the scintillator's light output response can be monitored and the liquids can be purified and recycled to maintain long-term stability over the period of several SSC runs [27,28]. Based on scintillation counting technology, CAPCAL also provides the high-speed response and energy resolution required for these systems, and provides a comparable level of performance to that of the central calorimeters.

Studies are in progress to evaluate the performance and sensitivity of various liquid/coating combinations for use in forward calorimetry [29], and on a liquid scintillator/glass capillary solution to this same problem [30].

The device currently being contemplated is a tungsten plug containing nonprojective channels coated with magnesium fluoride (n = 1.37) and filled with a radiation-hard liquid scintillator (e.g., 3 HF). The light from the channels is read out at the back of the calorimeter in the same fashion as the signals from the SPACAL calorimeter discussed earlier. This forward system will be a conical-shaped plug located approximately 15 m from the interaction point, with dimension of approximately 3 m in diameter. The choice of tungsten as the absorber provides a shorter absorption length than does lead, thereby reducing the lateral spread of the showers and improving E and missing E_T measurements in this region. A tungsten absorber at this position should provide shower containment to $\eta = 5.2$ and coverage to $\eta = 5.5$.

Tests have shown that the light output from liquids can be as large or larger than that from solids, depending on the choice of fluors [31, 32]. Work is in progress on the radiation hardness for a mineral oil-based liquid scintillator. Findings thus far indicate that the light output and attenuation lengths in typical prototype lead/scintillator modules to be unaffected by doses of radiation up to 1 Mrad. A glass capillary/lead glass version of a forward calorimeter module should be ready for testing by the end of the year [30].

The near-term effort will involve the study of the radiation hardness of the various components planned for use in this system; the study of the monitoring and circulation of the liquids in such a system and how to maintain a constant efficiency/resolution over the course of operation at the SSC; and the building and testing of a full-sized liquid-filled tungsten prototype to examine carefully the performance of such a device.

2.5.2 High-Pressure Gas and Crystals

As discussed in the EEoI, we are developing this option for the forward calorimeter. Designs are being developed using tubes filled with high-pressure gas as well as a regular sandwich geometry as for liquid argon. The signal collection time is much faster compared to liquid argon, while the sampling ratio is less. Beam tests of high-

pressure gas prototypes are scheduled for this winter at Protvino, USSR [33].

Another interesting idea will be beam tested in Protvino using extremely radiation-hard crystals of $KMgF_3$ that are read out with a gas chamber [34].

2.6 TRIGGER

The Level 1 calorimeter sum begins on the ADC boards where analog sums are formed. Sums are formed into trigger towers of $\Delta\eta = \Delta\phi = 0.2$. In the case of LAr, the pulses are clipped to produce short pulses suitable for use in real-time trigger sums. After this first analog sum, the trigger electronics for the LAr and the SPACAL options are the same.

The analog sum signals are routed to special trigger boards (Fig. 2-11). Each sum signal is digitized by a flash ADC with a nonlinear reference chain. The FADCs have 12 bits of dynamic range and eight of resolution. The FADCs are strobed every bunch crossing, after which the Level 1 calorimeter trigger is fully pipelined, with a new input every 16 ns. The FADC outputs are first linearized using memory look up units (MLUs) that generate values suitably weighted for X and Y transverse energy sums of 12 bits each. Flag bits corresponding to programmable thresholds are also generated for each tower. The transverse energy sums will be formed using either a binary adder tree, as shown in Fig. 2-11, or a linear pipeline adder. The end result will consist of the total transverse energy, the missing transverse energy, isolated EM showers, plus pattern and threshold information.

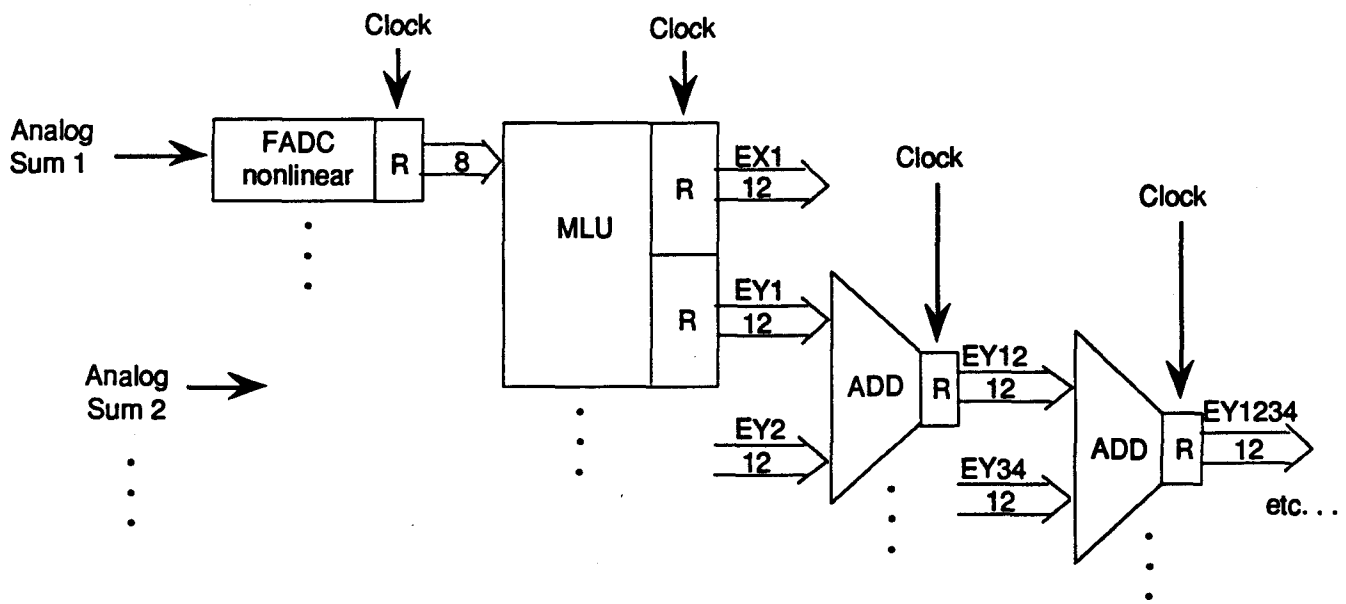

Figure 2-11 Level 1 trigger for the calorimeter.

REFERENCES

1. I.L. Azhgirey and N. V. Mokhov, "Radiation Doses and Background Particle Fluxes in EMPACT Experiment at the SSC," EMPACT/TEXAS Note 329, October 31, 1990.
2. T. Kamon, "Search for the Intermediate Mass Higgs," EMPACT/TEXAS Note 340(1990). Also see similar work in C. Seez *et al.*, "Photon Decay Modes of the Intermediate Higgs;" Proceedings of the ECFA Workshop on LHC, Aachen, October 1990.
3. D. Acosta *et al.* (SPACAL collaboration), Nucl. Instr. and Meth. A294, 193 (1990); R. Desalvo *et al.* (SPACAL collaboration), Nucl. Instr. and Meth. A279, 467 (1989).
4. T. Coan *et al.*, "The Manufacturing Engineering of a Hermetic Cast Fiber Calorimeter," Proceedings of the Symposium on Detector R&D for the SSC, Fort Worth , October 1990.
5. R. Wigmans, "Recent Results from SPACAL," Proceedings of the Symposium on Detector R&D for the SSC, Fort Worth, October 1990.
6. D.W. Hertzog *et al.*, Nucl. Inst. and Meth. A294, 446 (1990).
7. J. Brogan *et al.*, "Status of EMPACT/TEXAS SPACAL Calorimeter Engineering Design," EMPACT/TEXAS Note 339 (1990).
8. D.W. Hertzog *et al.*, "Can a Pb/SSIFI Calorimeter Survive the SSC," Proceedings of the Workshop on Radiation Damage of Plastic Scintillator, Tallahassee, Florida, March 1990.
9. "Inclusive Jets Studied at CDF," CDF collaboration presented by S. Bertolucci, Proceeding of the 8th Topical Workshop on Proton-Antiproton Collider Physics, Castiglioni della Pescaia, Italy, September 1989; and J. Huth, "Jet Energy Measurement-CDF Experience," Proceedings of the Workshop on Calorimetry for the SSC, Tuscaloosa, Alabama.
10. UA2 Collaboration, Phys. Lett. B241, 150 (1990).
11. S.R. Hahn *et al.*, Nucl. Instr. and Meth. A267, 351 (1988); and S. Bertolucci *et. al*, Nucl. Instr. and Meth. A267, 301(1988).
12. Y. Kubota and C. O'Grady, Nucl. Inst. and Meth. A279, 73(1989); and J. Berger *et al.*, ibid, 343(1989).
13. H.P. Paar, "Beam Tests of a 13 Ton Lead and Scintillating Fiber Calorimeter," Proceedings of the Symposium on Detector R&D for the SSC, Fort Worth, October 1990.
14. HELIOS (NA34) Data, SSC Detector R&D at BNL, BNL Report 52244 , p. 15 (1990).
15. R. Dubois *et al.*, IEEE Trans. Nucl. Science, NS33, 194 (1986).
16. P. M. Mockett and M. Boulware, "Electromagnetic Shower Sampling Efficiency in Liquid Argon Sampling Calorimeters and the Sampling Efficiency Dependence on Low-Z Cladding of High-Z Absorber Plates," Proceedings of the Symposium on Detector R&D for the SSC, Fort Worth, October 1990.
17. J. E. Brau and T. A. Gabriel, "Monte Carlo Investigation of Compensation," SLD-New Detector Note #119 (May 22, 1984).
18. D. F. Anderson, Nucl. Instr. and Meth. A245, 361 (1986).
19. G. S. Abrams *et al.*, "Progress Report on Work Done in FY90 and Request for FY91 Funding for Research and Development of a Liquid Argon Calorimeter for the SSC," submitted to the SSC Laboratory, Sept. 1990.
20. H. Burhhardt *et al.*, Nucl. Instr. and Meth. A268, 116 (1988)
21. K. Pitts and J. Brau, "The Effect of a Preradiator on the Energy Resolution for the EMPACT/TEXAS Liquid Argon Calorimeter," EMPACT/TEXAS Note 341 (1990).
22. W. E. Cleland *et al.*, "Signal Shaping and Noise for Liquid Argon Calorimetry," Proceedings of the Symposium on Detector R&D for the SSC, Fort Worth, October 1990; V. Radeka, "Speed and Calorimetry for the SSC," Proceedings of the Symposium on Detector R&D for the SSC, Fort Worth, October 1990; H. A. Gordon, "Liquid Argon Calorimetry for the SSC, "Proceedings of the Symposium on Detector R&D for the SSC, Fort Worth, October 1990.
23. L. Mason *et al.* "Design of the EMPACT/TEXAS Liquid Argon Calorimeter," EMPACT/TEXAS Note 351 (1990).
24. T. Adams *et al.*, "An Engineering Design of a Hermetic Liquid Argon Calorimeter for the SSC," submitted to Nucl. Instr. and Meth. (1990).
25. B. Aubert *et al.*, "Liquid Argon Calorimetry with LHC-Performance Specifications," CERN/DRDC/90-31 August 1990.

26. P. M. Mockett and V. Cook, "BRITE PADS," Proceedings of the Symposium on Detector R&D for the SSC, Fort Worth, October 1990.
27. R. C. Webb *et al.*, " Proposal to Investigate a Liquid Scintillator Alternative to Scintillating Fiber Calorimeter for the SSC," Generic SSC R&D proposal submitted to DOE, September 1989.
28. S. Dye *et al.*, "A Calorimeter-Based High-Rate Detector for the SSC," Expression of Interest submitted to the SSC Laboratory, May 1990.
29. The SSCintCAL Collaboration, "Scintillating Calorimetry for the SSC: A Progress Report and Request for Funds from the SSCintCAL Collaboration," submitted, September 1990.
30. Y. Pischalnikov *et al.*, "CAPCAL–Forward Calorimeter for EMPACT," EMPACT/TEXAS Note 296 (1990).
31. A. Sanzgiri *et al.*, "Tests of a Prototype Liquid Scintillator Based, Scintillating Fiber Electromagnetic Calorimeter," presentation at the Fort Worth Symposium on SSC Detector R&D, October 1990.
32. W. Worstell *et al.*, "Cast Lead-Eutectic Solid and Liquid Scintillator Fiber Shower Calorimeters," Proceedings of the Symposium on Detector R&D for the SSC, Fort Worth, October 1990.
33. I. Kotov, N. Fediakyn, "Forward Gas Calorimeter for EMPACT/TEXAS," EMPACT/TEXAS Note 295 (1990).
34. A. F. Busulutskov, "Calorimeters Based on $KMgF_3$ Crystals," EMPACT/TEXAS Note 297 (1990).

3.0 MUON SYSTEM

3.1 INTRODUCTION

The muon system for EMPACT/TEXAS was reviewed as part of the descoping program. All aspects were scrutinized carefully to understand the origins and interdependences of costs and their relationship to physics performance. In particular, the possibility of using iron toroids was reexamined including detailed design, costing, and performance evaluation—and found to be inadequate for our goals. We have reexamined the detailed mechanical design of the magnet, the choice of magnet parameters such as field integral and strength, the choice of detection system technology and geometric deployment of detectors, as well as the interaction of these elements with other parts of the detector. We have arrived at a new baseline system without serious degradation of the physics potential of the system. A crucial element in this process was the development, by our industrial partners, of a detailed cost parameterization of the toroidal magnet. The development of tools for simulation of backgrounds and punchthrough has given a much clearer understanding of this central problem and results in considerably increased robustness of the proposed system. Further steps will involve detailed global interactive optimization between the muon system and the calorimeter and tracking systems. To finally make the technology choices that still remain open at this point in the system design, a large body of performance information is required from the R&D effort already in progress.

3.2 SUPERCONDUCTING TOROIDS

3.2.1 Toroid Design and Descoping

The air-core toroids were reconfigured and downsized to establish a cost-effective and optimal momentum resolution. The muon system is shown in Figs. 1-4 and 1-6, indicating the key dimensions of the toroids and muon detectors. With respect to the EEoI, the central toroid inner radius was increased by 1.15 m to allow space for the separation of the inner muon chambers and for the enlargement of the calorimeter. The outside central toroid radius was unchanged and the peak field was held at 1.5 T. The length of the end toroid was reduced by 0.5 m, the peak field was reduced from 4.5 T to 3.5 T, and the total magnet system stored energy was reduced from 2.9 GJ to 1.9 GJ. Table 3-1 summarizes the overall parameters of the superconducting toroid magnet system for the LoI.

Table 3-1 Toroid system parameters.

Item	Central Toroid	End Toroid
Coil Type	Discrete	Discrete
No. of Coils	72	72
Conductor	NbTi/Cu Al Stabilized	NbTi/Cu Al Stabilized
Type of Stabilization	CICC	CICC
Total Number of Turns	1276	788
Maximum Field (T)	1.5	3.5
Current (KA)	32	32
Current Density (A/cm^2)	3048	3048
Stored Energy (MJ)	835	514
Coil Centering Force (M Nt)	0.79	2.6
Conductor Length (Km)	44.8	15.8
Conductor Weight (M Ton)	125	44
Winding Geometry		
Inner Radius (m)	5.4	1.6 Average
Outer Radius (m)	7.5	8.6
Length (m)	15.5	3.9

The LoI toroid system was developed using a bottoms-up cost analysis and cost parameterization of the EEoI baseline design [1] performed by Grumman, General Dynamics, Ansaldo, Oak Ridge National Laboratory (ORNL), and Princeton Plasma Physics Lab (PPPL). The work was based on extensive experience in the design and fabrication of aluminum structures; design, fabrication, and winding of large superconducting magnets; and design and operation of the Large Coil Task (LCT) facility. A large number of superconducting magnets have been built worldwide for plasma fusion, MHD, and accelerators. Table 3-2 lists the size and peak field of existing fusion magnets.

This group has concluded that constructing the air-core toroid system for EMPACT/TEXAS is well within state of the art. The detector magnets are considerably larger, but have lower fields and forces, fewer constraints, and are far less challenging in terms of engineering and fabrication.

Table 3-2 Superconducting fusion toroids.

Magnet	Size (m)	Field (T)
NASA Bumpy Torus (1971)	1.5 x 0.2	3.3
T-7 Tokamak (USSR, 1979)	2.4 x 0.7	4.8
LCTF (ORNL, 1987)	2.5 x 3.5	9.0
Tore Supra (France, 1989)	2.3 x 0.7	9.0
T-15 Tokamak (USSR, 1990)	2.5 x 0.7	9.0

3.2.2 System Conceptual Design

The conceptual design of the toroid system follows the original aluminum design concept set forth in the EEoI [2]. This approach uses azimuthal webs that tie the inner and outer winding and also connect the end faces. This allows the larger radial inward force acting on the inner winding to be supported, in part, by the outer winding and also improves the overall stability of the structure.

The baseline sub-element of the central toroid is a two-layer 5° segment (compared to the single-layer EEoI design). For the central toroid, the conductor makes a transition from two layers on the inner radius to a single layer on the outer radius. Spacers are used to support the layers in the transition areas. A closure member is then welded to the bobbin to form an integral structure and the complete assembly is vacuum impregnated. The 5° coil sub-elements are joined together by bolting at a flange interface located along the outer perimeter of the coil. The end toroid follows the same configuration and assembly approach as the central toroid.

Other configuration options were also considered that may reduce the coil winding cost and offer greater access for muon detector alignment equipment. One option, developed for a 9° segment of the end toroid, involves using discrete coil windings of constant width joined together with intercoil structure as shown in Fig. 3-1. A web structure, as described above, connects the inner and outer coil legs.

3.2.3 Superconductor

The aluminum stabilized NbTi/Cu, cable-in-conduit conductor (CICC) has been reevaluated and remains unchanged from the EEoI concept [3]. The choice of conductor is based on achieving a small number of radiation lengths within a conservative design approach. The use of aluminum for the stabilizer and conduit meets the requirement of minimizing radiation lengths, and a conservative design is achieved with a CICC based on conservative operating parameters. A copper-stabilized CICC conductor with an aluminum conduit, or an optional thin stainless steel conduit, is being considered as an alternative approach.

In a large magnet, no matter whether it is a toroid or a solenoid, there will be conductor movement and cracking of the resin system. Bench tests demonstrated that this movement can result in an energy release about 50–70 mJ/cc [4]. To develop a conservative design, we have specified a stability margin value for the conductor to be 150 mJ/cc, although it is quite unlikely that this energy density would be suddenly inserted into a well-designed coil. The LCT experience [5] showed that coils with similar margins operated reliably in the presence of epoxy cracking and frictional heat from sudden slippages. The present calculated margin

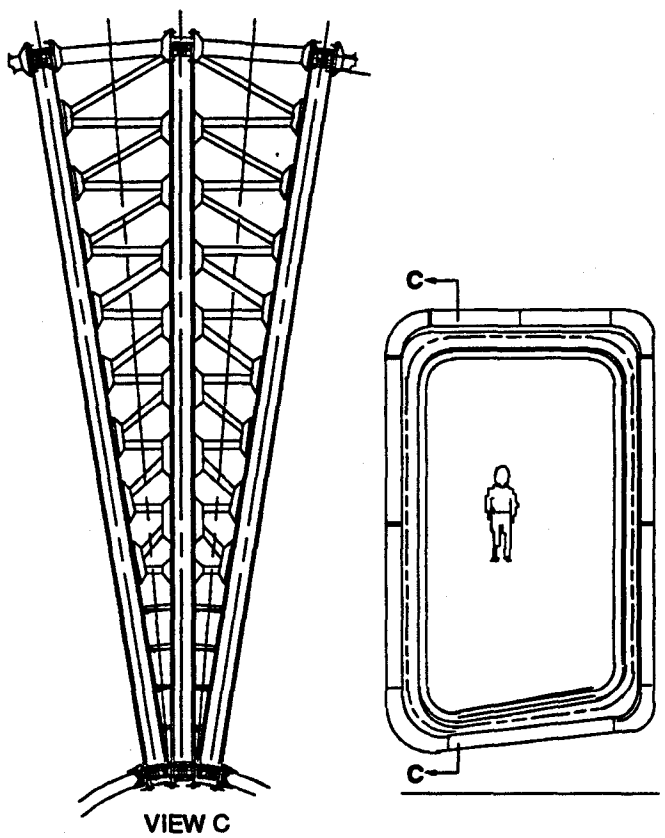

VIEW C
CROSS SECTION VIEW
LOOKING OUTBOARD

Figure 3-1 9° Discrete coil option.

for the baseline CICC conductor is 200 mJ/cc of cable space.

Pure aluminum was selected as the stabilizer material and an aluminum alloy sheath was selected as the structural conduit. The use of aluminum is an extension of prior practices, but gives the advantages of less multiple scattering, a higher conductivity for the stabilizer, and a lower expected cost. To minimize risk, conservative parameters were used in sizing the conductor. The design current is 50% of critical and we have used a residual resistivity ratio (RRR) for aluminum stabilizer of 1360. With a degraded resistivity ratio value of 400, resulting from manufacturing or high-field conditions, a hot-spot temperature of 120 K is still achievable with only minor changes in the dump-time constant and stabilizer area.

Each of the three toroids must be capable of surviving a quench. Reliable and redundant detection and protection circuits are routinely used with superconducting coils and will be employed. An initial quench protection system was sized for 1 GJ of stored energy with a dump-time constant of 19.5 seconds. The dump resistance is 0.113 ohms and the terminal voltage is 3.6 kV. Advantage was taken in that some of the current is shared by the aluminum structure. In the unlikely event that one of the coils is damaged, it should be possible to operate the toroid with a failed coil that is electrically bypassed.

3.2.4 Assembly

One key feature of the toroid design is the high multiplicity of identical coil elements. These coils will be fabricated by industry, and the requirement for 72 identical central coils and 144 identical end coils provides savings, reliability, spares, and a high degree of optimization in fabrication techniques. The coils will be fabricated and tested before shipment to the site. The central coils will be assembled, tested, and shipped as 45° units. The baseline approach is to assemble the central toroid below ground, building up from the 45° units. The end toroids will be assembled above ground and installed in the hall.

The dewar for the central and end toroids consists of a rib-stiffened aluminum structure that surrounds the complete toroid coil array. The central toroid dewar, magnet, and muon chambers are supported from tie rods to two fixed overhead frame structures, minimizing interference with the coverage of the muon chambers. The rods pass through an extended dewar to reduce thermal leaks. The end toroid dewar, magnet, and muon chambers are similarly supported, except that the support frames are mounted on rollers that permit axial movement of the total end assembly for installation, maintenance, and repair of otherwise inaccessible systems as illustrated on the back cover.

The central toroid inner radius has been increased to allow space for two separated muon chambers, thereby establishing a line-line measurement. The increased inner radius has also allowed simplification of the overall dewar construction and assembly of the central toroid system. The outer dewar cylinder can be completely assembled and a cold wall system installed and tested, permitting the insertion of a fully assembled magnet system using the assembly fixture sized to install the calorimeter. The magnet and dewar will be suspended from the overhead support structure and electrical and coolant lines will be connected before installing the dewar end closure structure.

The design process has been augmented by finite element analysis of the dewar and magnet structure, facilitating refinement of component sizing. Three-dimensional analysis of the 5° magnet segments under the magnetic pressure is shown in Fig. 3-2.

The dewar structure under combined gravity and pressure loads loads is shown in Fig. 3-3. This work, together with two-dimensional stability calculations, has provided the confidence necessary to proceed with the design.

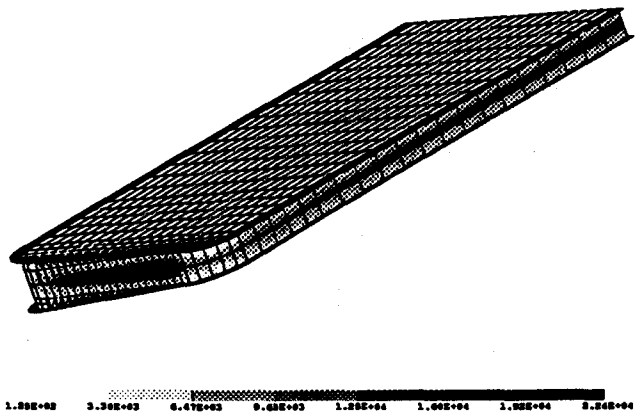

Figure 3-2 3-D finite element analysis of 5° coil sector.

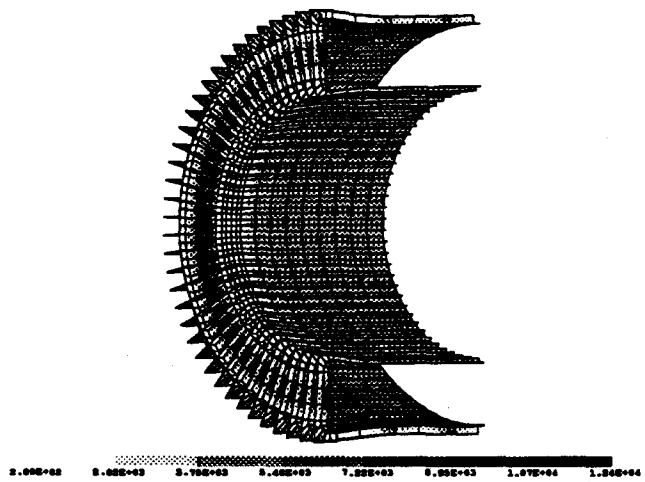

Figure 3-3 3-D finite element analysis of dewar structure.

3.3 MUON DETECTORS BASELINE CONFIGURATION

Limited streamer tubes operating in a drift mode have been selected as a baseline for the muon detection system and as the basis for costing. Such tubes give pulses of about 0.1 volts with 10 ns rise times, easily providing time resolution at the nanosecond level. Intrinsic resolution has been measured at below 100 μm up to drifts near 1.5 cm [6, 7]. There is significant experience in production of these tubes [8, 9, 10]. Quality control and yields in mass production have improved considerably in recent years, resulting in economical detectors for large areas [10, 11]. The wires will be positioned in the chamber to achieve a precision with respect to outside fiducials of 50 μm. The wire positions may be checked using x-ray tomography [12]. The chamber fiducials will be located with respect to each other with a precision of 25 μm.

To achieve the desired spatial accuracy and to provide a reasonable assembly system, the large detection layers (Fig. 3-4) are segmented into chambers. These chambers are typically 1 m wide, 0.125 m high, and of various lengths; they contain 4 wire layers. A chamber cross section is shown in Fig. 3-5.

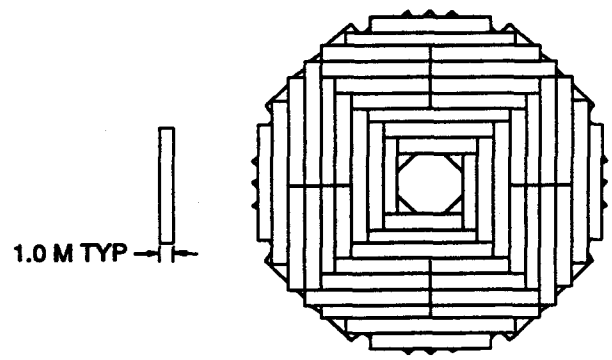

Figure 3-4 A schematic layout of the muon chambers for the end cap.

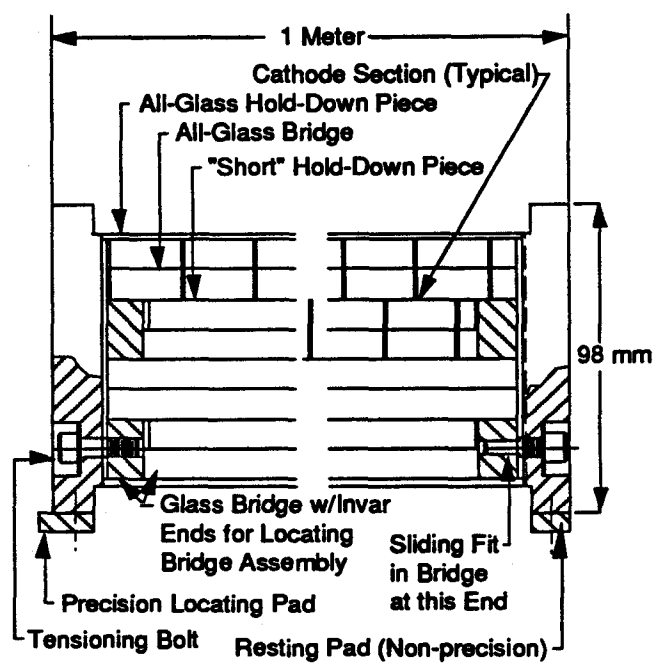

Figure 3-5 A cross sectional view of the muon chamber showing the housing with the outside positioning pads, the bridges, the wires, and the cathode planes.

The main elements of the chamber are: wires in 4 layers on a 2.5 cm pitch; precision bridges holding the wires in place to the required tolerances; and sheets of U-shaped cathodes surrounding each wire. Drift measurements are made with respect to wire positions; these are held to 25 μm by bridges made of stable insulating material that have been precision grooved to accept the anode wires and clamped in place by a second piece glued to the first. These bridges are precision located with respect to two fiducial pads on the outside of the chamber wall. The cathodes are formed by a comb of thin conductor and clamped between the bridges. At the bridge points the side walls are machined away to allow passage for the bridge. The cathodes are extruded or roll-formed aluminum to minimize material. The wire and metal cathode acts as a cable to transmit the pulse to the electronics with the speed of light and without degradation in rise time.

3.3.1 Muon Detector Program

A vigorous program of muon detector R&D is underway in the U.S. and USSR. This program focuses on development and comparison of techniques suitable for the SSC environment, development of methods for mass production and calibration, and an extensive program of bench and beam tests of prototype detectors.

There are a number of track measurement schemes that may satisfy the high-accuracy, large area, and reasonable cost requirements for an SSC detector. Drift tubes with specially profiled cathodes and high-accuracy wire alignment are used in the baseline design. The bend-plane positions will be measured using the drift time. A combination of drift time and charge strip readouts will be used for the nonbend plane to provide unambiguous space points. An alternative is to use the same type of drift tubes without precision wire alignment but still with sufficient rigidity to ensure stable wire positions. This requires calibration of each wire position, and the difficulty of doing this must be balanced against the lower construction costs.

Preliminary tests using laser pulses have established intrinsic resolutions and dependence on drift time as shown in Fig. 3-6 and 3-7 [13].

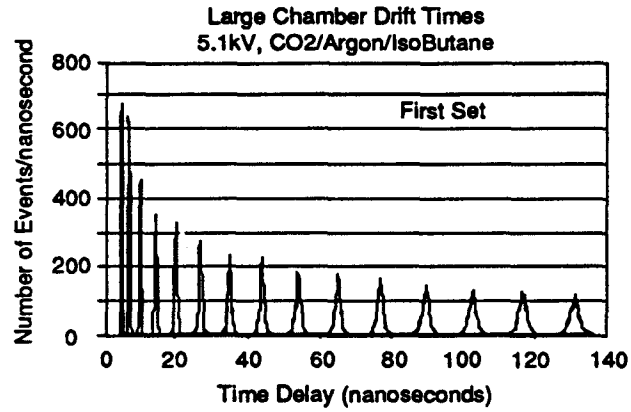

Figure 3-6 A typical laser run on a 2.5 cm square cross section tube showing the time distribution of pulse arrivals from a laser beam sent through the tube at 635 μm spacings.

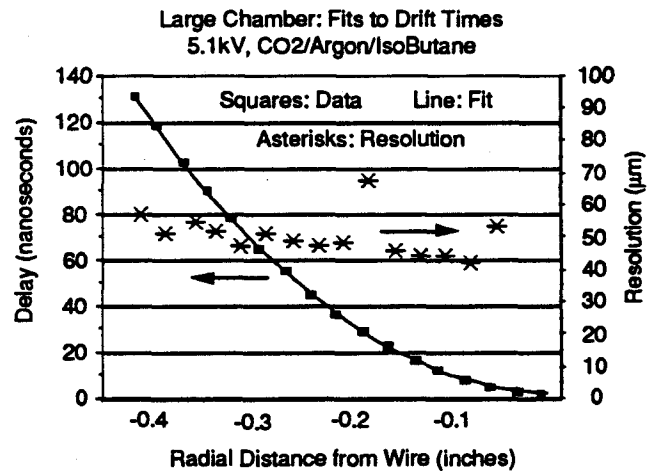

Figure 3-7 Dependence of drift time (left axis, squares) and spatial resolution (right axis, asterisks) versus distance to anode wire.

Figure 3-8 shows an x-ray scan of an aluminum streamer tube that can determine wire position to better than 20 μm [12]. This work will be extended to demonstrate feasibility of determination of positions within a stack of chambers.

Profiled cathode tubes with analog strip readout for the bend coordinate have the advantage that strip readout is almost insensitive to detector geometry deviations and gas mixture changes, and that the precision comes from fabrication of large area cathode planes rather than the wire positions. Resolutions of 50 μm have been obtained with small wire cathode chambers [14,15], while resolutions of 400 μm have been achieved with external pickup

strips [12,16]. Preliminary results using x-rays indicate that the intrinsic resolution is much better, as shown in Figs. 3-9, 3-10, and 3-11 [16].

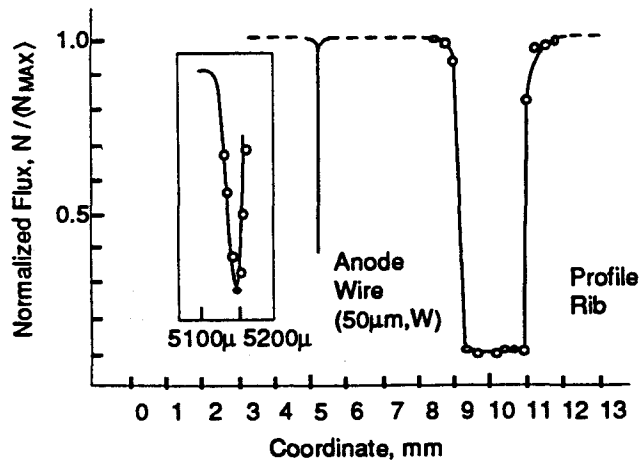

Figure 3-8 X-ray scan of an Al extruded tube in a plastic envelope. Modulation of x-ray flux shows the determination of wire position with an accuracy better than 20 μm. Insert shows the wire position on a finer scale.

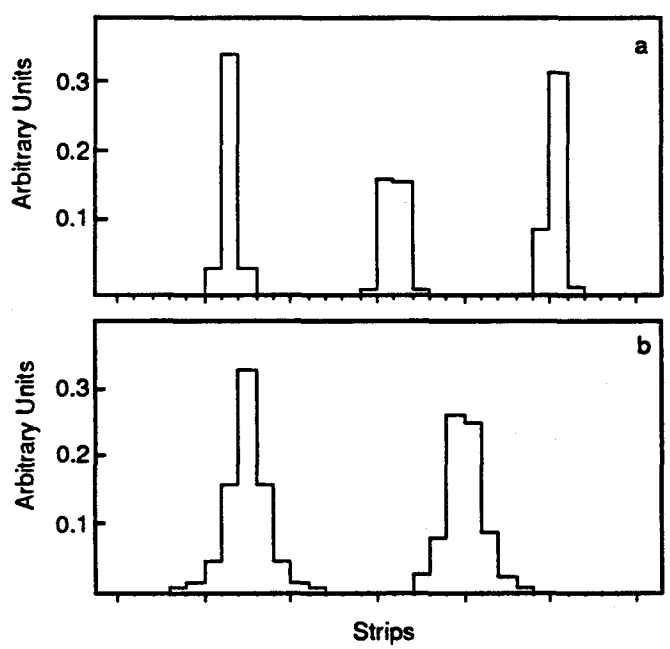

Figure 3-9 Charge distribution on strips perpendicular to anode wires. Data have been obtained with 1 cm strips and 1 cm cell Iarocci tubes: (a) Al tube; (b) plastic high-resistivity tube.

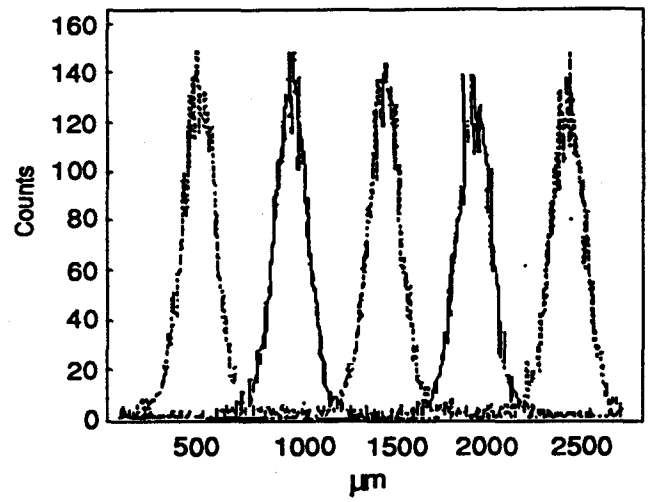

Figure 3-10 Measured position distribution obtained with 1 cm wide strip readout. Data have been taken with x-rays and in proportional mode. Peaks are spaced 500 μm apart.

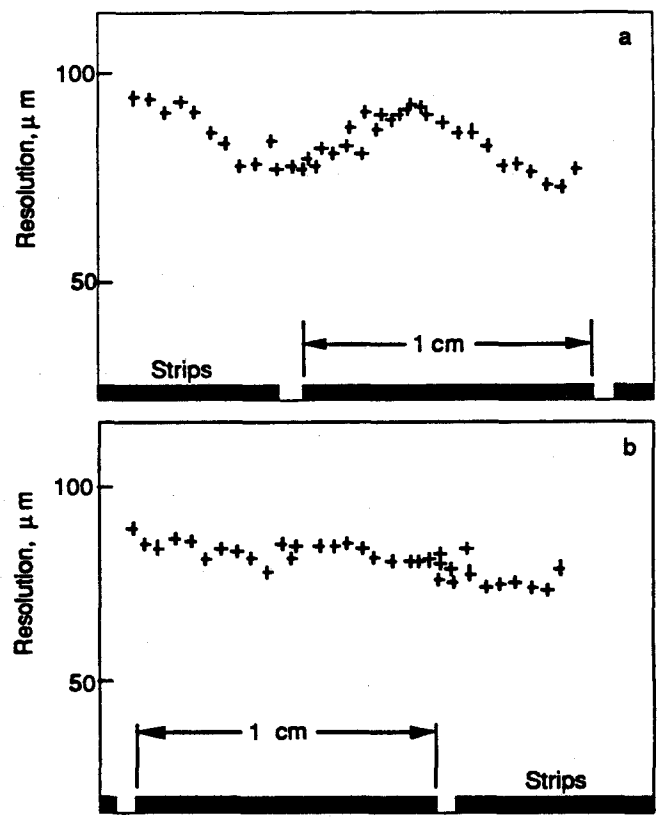

Figure 3-11 Strip readout spatial resolution vs avalanche position along anode wire: (a) low-resistivity tubes; (b) high-resistivity tubes.

Finally, multiwire drift chambers are a well-understood technique and the almost complete absence of material is an obvious advantage of this approach. These chambers may be competitive in the forward-backward regions where they would hang vertically.

All of these techniques are currently being explored. The R&D may point to the symbiotic combination of different approaches. For example, strip readout is already assumed for some nonbend coordinate measurements and for track matching, and "tomography" may be used with the baseline LoI scheme for checking wire alignment accuracy in prepared detector units.

3.3.2 Chamber Assembly and Support

The superconducting air-core toroids are surrounded by pairs of muon detectors supported from overhead frames. Figure 3-12 shows the overhead support of the central detectors. Each detector pair consists of two superlayer panels joined by a rigid truss structure. The trusses have adjustable fittings that can be varied to align fiducial marks using conventional metrology. This operation takes place in alignment fixtures located in the surface assembly facility as part of the muon detector construction.

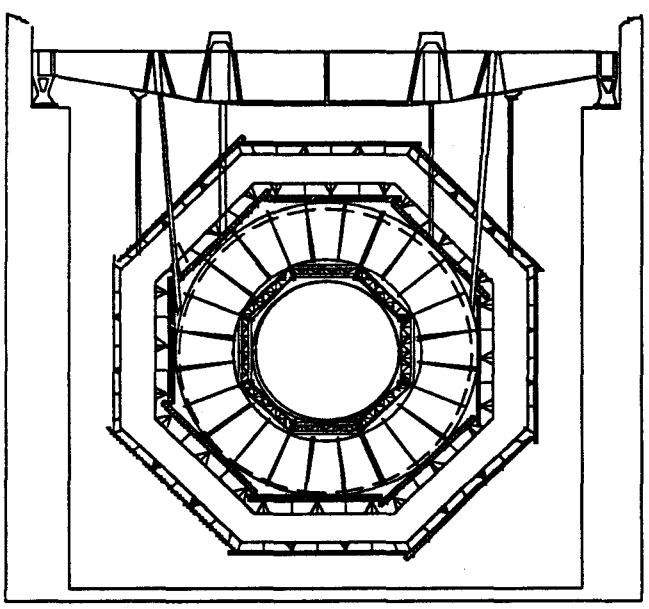

Figure 3-12 Support structure for central detectors.

A superlayer consists of an array of muon chamber modules that are oriented in bend-plane and nonbend-plane directions. These are held together with thermally stable material so that residual temperature gradients less than 5°C will have a negligible effect on the position of the chambers. Structural members form a lattice support on the upper and lower surface of the superlayer and are attached to a frame structure around the superlayer edge. Tie-bolts through the interstices formed by bend- and nonbend-plane chambers join the upper and lower layers at 1 m intervals. Finite element analysis is being generated to ensure that superlayer structural stiffness and overall support stiffness is commensurate with the alignment requirements for allowable deflections.

3.3.3 Muon Chamber Alignment

The accuracy of the muon momentum measurement is dependent on the relative positions of the muon detector elements. The concept currently under development [17, 18] is based on an electro-optical laser system that will continuously monitor, in 6 degrees of freedom (DOF), positions of fiducial markings placed on the external surfaces of each muon superlayer with an accuracy of 25 μm. Material selection and manufacturing techniques will guarantee that the location of each internal detection plane is known to within 50 μm relative to the superlayer external fiducials. The alignment system assumes access to the external pair of chambers but not the internal pairs. Only passive optical elements (i.e., mirrors) are located on the inner layers, whose positions are determined by means of laser beams directed through lines-of-sight provided through the toroid volume.

A combination of five optical devices are proposed that together will measure the position of a set of four superlayers in 6 DOF. These devices are constituted of off-the-shelf light sources, sensors, and mirrors, used in state-of-the-art precision metrology. The chambers will be aligned in a fixture above ground, giving an ideal measurement that the alignment monitoring system will reestablish when the muon detector modules are installed underground. The alignment system will provide

continuous monitoring of the superlayer positions relative to the ideal.

3.3.4 Electronics

A block diagram of the muon drift wire readout is shown in Fig. 3-13. For limited streamer mode operation, electronic amplification is probably not needed and the signals are fed directly to a chamber-mounted discriminator card that employs custom-designed discriminators optimized for large pulses. The discriminator signals are transmitted differentially through twisted pairs to FASTBUS-size time-to-digital converter (TDC) cards housed in off-detector racks.

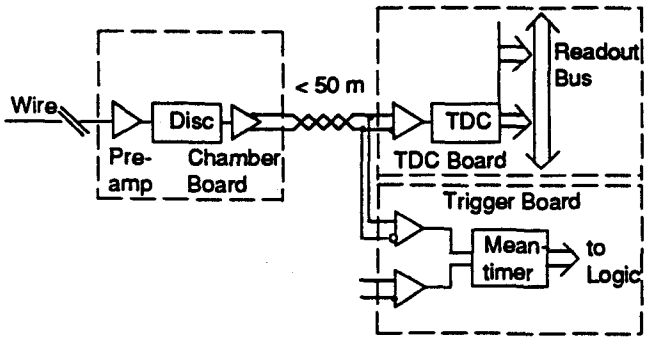

Figure 3-13 Block diagram of the muon driftwire electronics.

The TDCs are digital custom CMOS monolithics [19] with a resolution of 0.5 ns (least count) and a multihit resolving capability of 32 ns. The operation of the chip is effectively that of a 32 μs deep pipeline, although the internal arrangement of the logic is somewhat different. With current technology a single chip can accommodate 8 TDC channels and a single TDC card can accommodate 128 channels. Advances in technology will likely result in improved performance and greater packing density.

Signals from the charge strips can be encoded using the same multihit TDC scheme with suitably modified preamp/discriminator cards. When combined with the driftwire information from the same chamber, this information provides correlated space points for pattern recognition. If only leading edges are recorded, the spatial resolution will be determined by the strip width. By using a time-over-threshold discriminator and encoding trailing edges as well, modest improvements in spatial resolution can be obtained by calculating the center of gravity of the induced charge.

The muon trigger scheme is based on measurement of the exit angle of tracks as they leave the air-core toroids, as described in the EEoI. Identification of high-p_T tracks [20, see also Sect. 3.4.3] is accomplished by looking for coincidences between superlayers along corridors that correspond to stiff tracks. In the outer chambers, the rates are comparatively low so that logic can be performed using pulses stretched to take into account the 200 – 300 ns arrival time dispersion caused by drift-time variations. For synchronization with the rest of the experiment, however, the muon trigger system must produce a pulse with a time jitter of less than one bunch crossing time (16 ns) with respect to the actual time of the event. This is done by instrumenting a fraction of the outer muon superlayers with "meantiming" circuits that compensate for the drift time by calculating the average arrival time for pulses with staggered cells. With a flat gas conventional analog meantiming circuits will work. However, for ohmic gases a digital meantimer (DMT) [20] with table lookup is needed to compensate for the nonlinear time-distance relation. The synchronous pulse, gated by the high p_T signature, is then routed to the Level 1 "decision box" for participation in the Level 1 trigger.

Such a scheme is shown in block diagram form in Fig. 3-14.

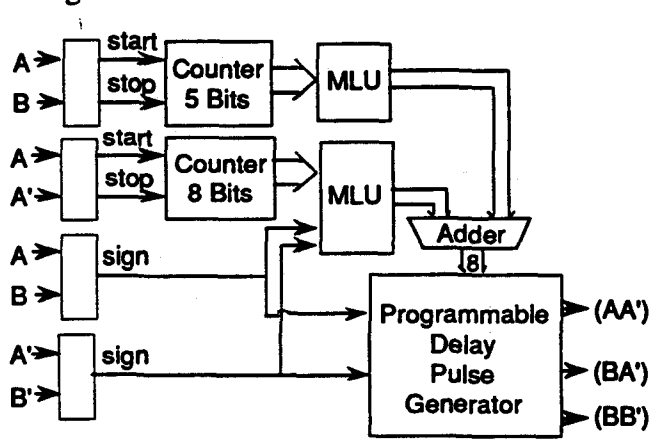

Figure 3-14 Block diagram of the digital meantiming (DMT) circuit for the muon trigger.

The DMT has two inputs and produces a single output pulse, delayed by an amount that depends on the difference in arrival times of the inputs. The DMT is implemented on a chip using the same precision timing technology as the TDC chip described above. Two DMTs are required for each trigger cell, one to eliminate wire propagation delay variations and a second to eliminate drift-time variations. The first meantimer is also programmed to compensate for the flight path and calibration variations between muon chambers.

3.4 MUON SYSTEM PERFORMANCE AND ROBUSTNESS

Robustness of the muon system has been studied in terms of the resolution for low- and high-momentum muons, the ability to trigger on high-p_T muons, and the ability to reconstruct a muon track in spite of hadronic and electromagnetic backgrounds.

3.4.1 Muon Backgrounds

3.4.1.1 Beampipe/Spray Backgrounds—One of the major backgrounds in the forward muon system is the spray of secondary particles from the small angle beampipe region. A large number of secondary particles are generated in this region as the primary particles go through a relatively large thickness of the beampipe at the small incident angles. To prevent these secondary particles from entering the forward muon detection systems, lead shielding has been added to the inner face of the muon system along the beam line. With a 5 cm lead shield, the secondary charged particle rate entering the muon systems is reduced by a factor of 45. Figure 3-15 shows the rates of charged particles entering the forward muon system as a function of the lead shield thickness [21].

To further reduce the background from this source, the possibility of using a cone-shaped beampipe was investigated. In this configuration, the effective thickness of the beampipe for the small angle region is reduced with a consequent additional reduction in the background. The effect on the SSC beam of such an irregularly shaped beam pipe has been investigated [22] and found to be negligible. It is anticipated that optimization of the beam pipe and shield can effectively eliminate this source of background.

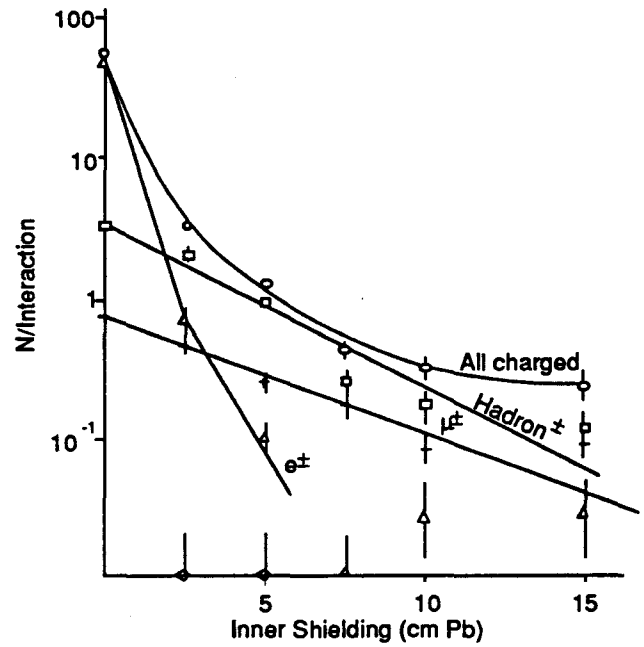

Figure 3-15 The rate of charged particles entering the forward muon system as a function of the lead shield thickness. Also shown are the curves for hadrons, muons, and electrons. The data are normalized to one beam-beam interaction, 50% minimum-bias events plus 50% mini-jet events.

3.4.1.2 Hadronic Punchthrough—The punchthrough probability as a function of depth, the punchthrough momentum and multiplicity spectra, and other characteristics were calculated by following the development of a GEANT simulated cascade generated by single-incident hadrons in their passage through segmented absorber material. This study of hadron punchthrough [23] has yielded a punchthrough shower profile that was incorporated into simulations of physics processes in the form of probability tables. This method provided the EEoI results, indicating that the depth of the calorimeter in the current design (at least 11 λ at 90° and about 15 λ in the end cap) is sufficient to reduce the rate of hadron decay and punchthrough particles with $p_T > 5$ GeV/c after the calorimeter to less than that for prompt muons from c, b quarks.

An effort to refine the probability tables is underway, and the simulation will be verified in upcoming test beam runs.

The debris from a hadron shower exiting the calorimeter tends to lie within 20 cm of the projected position of the parent hadron track, and these outgoing particles tend to be at large angles relative to the initial direction of the parent hadron. The outgoing angular distribution is shown in Fig. 3-16 for three bins of outgoing particle momentum.

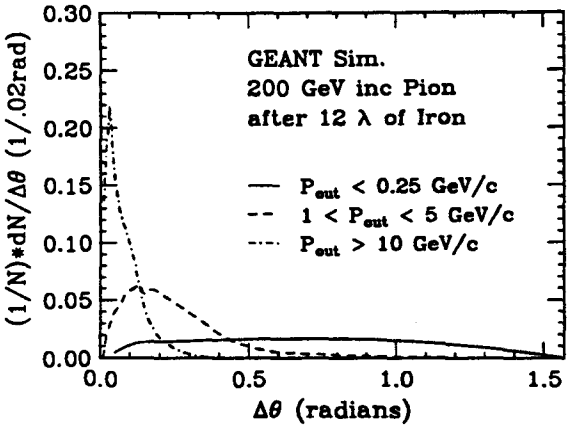

Figure 3-16 Angle between incident pion and punchthrough particles after the calorimeter.

3.4.1.3 Muon Radiation Backgrounds—As the energy of the muon increases, the energy loss caused by radiation, pair production, and interactions as it passes through the calorimeter will increase. This will give rise to showers of particles accompanying the muon exiting the calorimeter, potentially obscuring the muon position measurement in the planes immediately following the calorimeter. Various studies have been made of pair production and bremsstrahlung from high-energy muons and two independent simulations were performed, one using GEANT [23] and the other an analytic estimate of the muon energy loss followed by EGS simulation of the electromagnetic particles [24]. Figure 3-17 shows the probability that a muon will emerge from a substantial thickness of iron with one or more accompanying tracks. The trend towards higher probability with increased muon energy is clearly seen. Figure 3-18 shows the mean multiplicity of extra tracks as a function of incident muon energy; the trend is toward increasing multiplicity with increasing muon energy; at 1 TeV/c there are 3–4 extra particles on average.

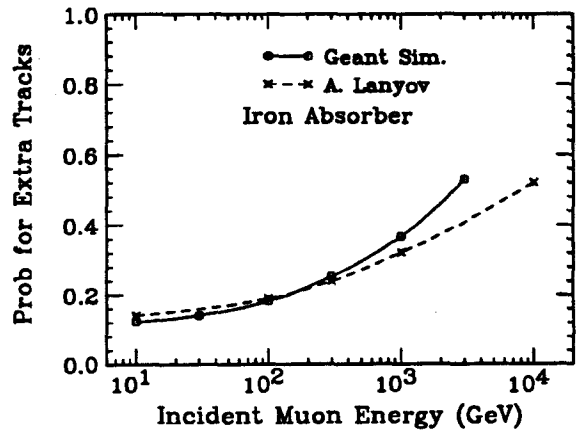

Figure 3-17 Probability for one or more extra particles accompanying the muon after iron absorber.

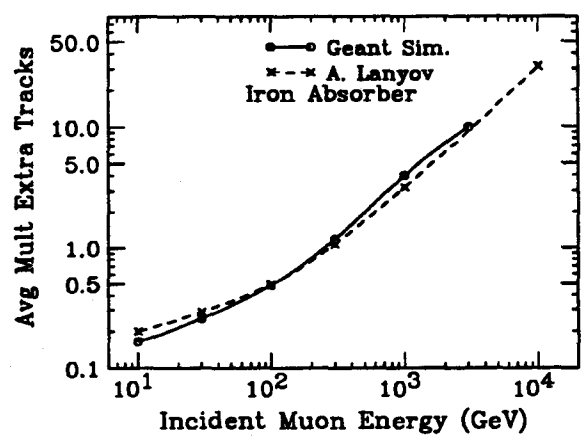

Figure 3-18 Mean multiplicity of extra tracks accompanying the muon after iron absorber.

The momentum distribution of the accompanying particles for thick iron absorber is shown in Fig. 3-19. The addition of low-Z material after the absorber was suggested [25] to suppress the bremsstrahlung component of the muon radiation. It was found by GEANT simulation that the probability of one or more extra particles was little changed by the addition of graphite. However, there was a significant reduction in the mean multiplicity suggesting the suppression of e^+e^- pairs (but not delta rays) by the low-Z material.

This is seen in the dashed histogram in Fig. 3-19 (for the same number of incident muons), which is for an iron absorber followed by 6 cm of carbon with density of 1.7g/cm^3. The addition of aluminum to a high-Z material shows a similar effect, and the baseline design has a minimum of 7.5 cm of aluminum in the calorimeter support tube.

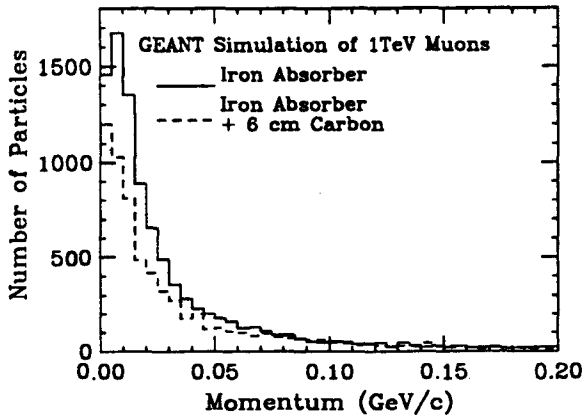

Figure 3-19 Momentum of extra particles accompanying the muon after the absorber with and without carbon filter.

Figure 3-20 shows the distribution of the outgoing angle of the accompanying particles relative to the incident muon direction. This distribution is very broad primarily as a result of the low energy and hence large scattering of these particles. Because the accompanying particles exit from the calorimeter very near the muons (within a few mm), the separation of muons from background is improved by providing a 10 cm drift space before the muon system.

If not corrected, the energy loss by the muon in the material preceding the muon spectrometer will degrade the resolution. Two separate simulations were performed [26, 27], and they are in agreement. Figures 3-21 and 3-22 show, for two values of the incident muon energy, the energy loss distribution and fraction of muons losing more than a given energy in 400 X_0 of lead. It will be important for this energy to be measured in the calorimeter and added to the muon momentum measurement in the toroid spectrometer to obtain the best possible mass resolution.

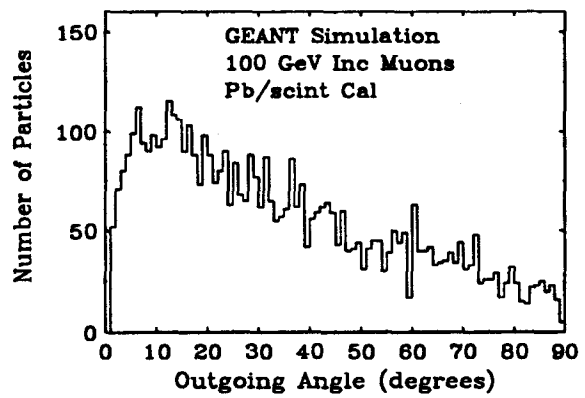

Figure 3-20 Outgoing angle of particles accompanying the muon relative to the incident direction.

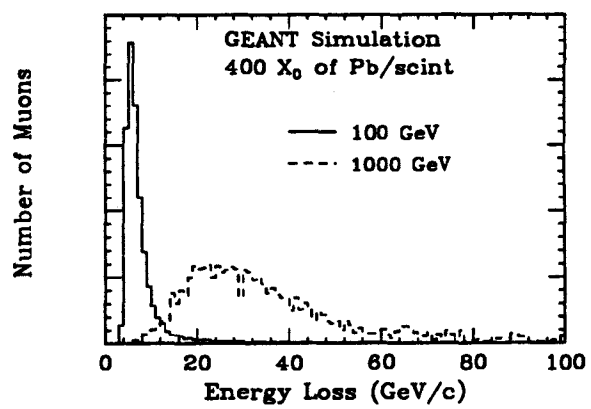

Figure 3-21 Energy loss of 100 and 1000 GeV muons in Pb/Scintillator calorimeter.

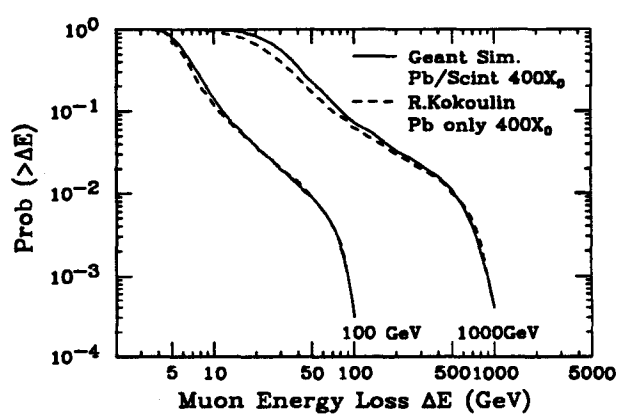

Figure 3-22 Probability that a muon will lose energy > ΔE (GeV) for two values of incident energy.

3.4.2 Rates and Pattern Recognition

The two issues that must be considered for robustness of the muon system are (1) whether the baseline limited streamer tubes stand the particle flux; and (2) if the accompanying flux of hadronic and EM debris obscure muon tracks.

The maximum count rate in the first muon chambers is in the forward regions, where rates reach 91 tracks (muon plus event background) per second per cm^2 at luminosities of 10^{34} cm^{-2} s^{-1}. For standard cell sizes of 2.5 cm this translates to 228 Hz/cm of wire. Limited streamer tubes have been operated reliably at rates over 250 Hz/cm with no significant effect on pulse height and have been run up to 1000 Hz/cm. There is considerable margin once the rates are better established, because if operation with standard cell size is questionable, it can be reduced in the small regions near $\eta = 2.5$. Limited streamer tubes with cell sizes down to 0.4 cm have been successfully operated [28].

To test the robustness of the muon system in the face of the hadronic and electromagnetic backgrounds, two severe cases were studied: very high p_T heavy-top events having energetic jets close to a muon trajectory, and a very heavy Z′ decaying to muons that may radiate. Despite the fact that many of the muons are accompanied by extra tracks, detailed analysis shows that most muons can be cleanly reconstructed.

Two hundred top (250 GeV mass) events were generated with the p_T (jet) > 1 TeV/c, and with at least one semileptonic b decay to a muon. The probability for the secondary particles from the hadronic punchthrough to accompany the real muon hits at the first muon detector after the calorimeter is large for these high-p_T jets. A total of 107 out of 217 muons from b or c decays had at least one secondary particle caused by hadronic punchthrough or muon radiation in a cone of R = 1 around the muon. The worst event among these is shown in Fig. 3-23. Eight drift planes in the bend view before the air-core toroid are shown. Each superlayer station provides two space points with a single-track resolution of 200 μm in the bending plane and 1 cm in the nonbend plane. The minimum distance between the first measuring station and the calorimetry is 10 cm. The physical cell size is 2.5 cm. With 2.5 mm double-hit resolution electronics, an effective cell size of 1 cm^2 is assumed for the purpose of pattern recognition. Defining a clean cell as a cell hit only by a single track, only 3 out of 217 muon tracks are completely overlapped by other tracks, and the majority of the tracks (199) are free of any overlap.

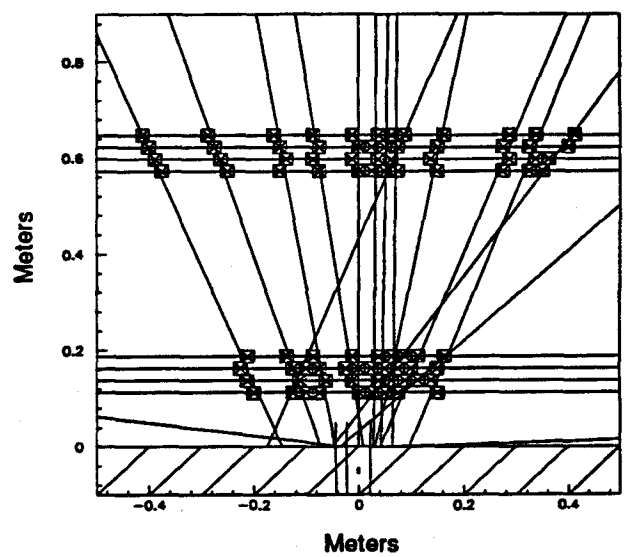

Figure 3-23 Muon track (vertical at 0) coming out of the calorimeter accompanied by the secondary particles resulting from hadronic punchthrough or muon radiation in a 250 GeV high-p_T top event.

One hundred 4 TeV Z′ events were generated, each decaying to a pair of muons. A total of 90 muons had at least one secondary particle caused by muon radiation. The worst event among these is shown in Fig. 3-24. Only 12 out of 200 muon tracks are completely overlapped by other tracks, and 164 tracks are free of any overlap.

In summary, for high-p_T top events, 1.4% of the muons from b or c decay with p_T > 10 GeV/c were lost because of the presence of the secondary particles from hadronic punchthrough and muon radiation, while 91.7% of them had 8 of 8 clean hits. For very high mass Z′ events, 6% of the muons were completely lost because of the presence of the secondary particles from muon radiation while 82% of them had 8 of 8 clean hits. Table 3-3

summarizes the muon track-finding efficiencies for the events discussed above.

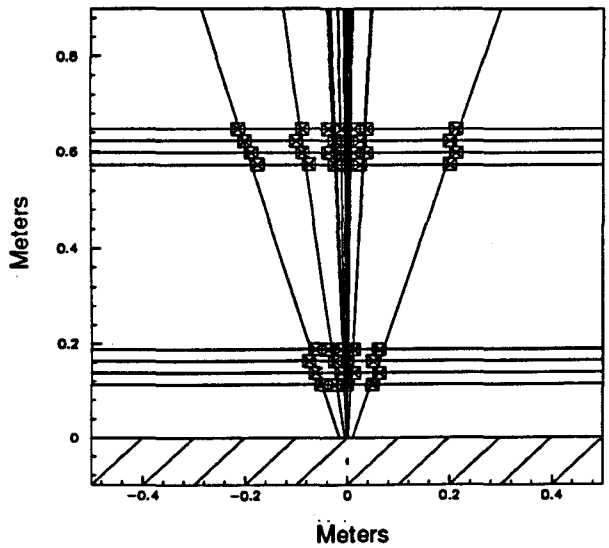

Figure 3-24 Muon track (vertical at 0) coming out of the calorimeter accompanied by the secondary particles resulting from muon radiation in a 4 TeV Z′ event.

Table 3-3 The track-finding efficiencies are summarized for the muons from the b or c decays in 250 GeV high-p_T top events and in 4 TeV Z′ events. The corresponding values are also shown for the case with no double hit capability (i. e. 2.5 cm cell size) and for two different requirements of a good muon track.

Cell Size		8 Good Hits Required	4 (Super Layer 2) Good Hits
2.5 cm	Z′	75.5 %	85.0 %
	t	87.6 %	94.0 %
1 cm *	Z′	82.0%	92.0%
	t	91.7%	96.8%

* Effective cell size with double hit electronics

3.4.3 First-Level Muon Trigger

The magnetic properties of air-core toroids result in a simple triggering scheme, because the magnetic bend is almost independent of polar angle for constant p_T. Because hadrons are filtered by the calorimeter and low-p_T muons are swept away by the toroid, the trigger will simply require tracks after the toroid to point back to the interaction region within a certain tolerance. The tolerance determines the effective p_T cut of the trigger. As the luminosity increases, the tolerance can be tightened, resulting in a higher p_T cut, to keep down the trigger rate.

The trigger design considered for EMPACT makes use of measurements after the toroid. For the muon baseline design, the detectors are drift cells of size 2.5 cm. The outer two layers of cells are separated by 3 m. From a hit in the first layer, one can determine the cell in the second layer that would be hit by a straight track pointing back to the interaction region. Tables 3-4 and 3-5 show the corresponding p_T for a track hitting the second layer DIFF cells away from this cell. Also shown is the cross section for producing particles in the muon system that satisfy the trigger requirement, including sources from prompt muons, decays, and punchthrough particles, but not including spray from the beam pipe. Further simulation study is underway to consider the rate of occupancy of nearby cells.

Table 3-4 Probability and cross section for a muon of p_T to satisfy various DIFF≤ n conditions in the central region.

DIFF	Pt (10% eff)	Pt (90% eff)	σ (μb)
≤ 1	24	44	0.008
≤ 2	16	24	0.08
≤ 3	13	17	0.2
≤ 4	11	15	0.3
≤ 5	9.5	13	0.5
≤ 6	8.5	11.5	0.7
≤ 7	8	10.5	0.8
≤ 8	7	10	1.1

Table 3-5 Probability and cross section for a muon of p_T to satisfy various DIFF≤ n conditions in the end region.

DIFF	Pt (10% eff)	Pt (90% eff)	σ(μb)
≤ 1	21	35	0.02
≤ 2	14	19	0.2
≤ 3	10.5	14.5	0.5
≤ 4	8.5	11.5	1.2

The first-level muon trigger is formed by the coincidence of a hit in the first layer with all hits in the second layer with a certain DIFF value. By changing DIFF, one can change the trigger level.

At a luminosity of 10^{33} cm^{-2} s^{-1} the first-level muon trigger can easily be kept under 10^4 Hz. At a luminosity of 10^{34} cm^{-2} s^{-1} the first-level trigger rate can still be kept under 10^4 Hz with DIFF ≤ 5 and 3 in the central and end regions respectively. These values correspond to p_T cuts of around 11 and 12.5 GeV in these regions. The first-level muon trigger is flexible and robust.

3.4.4 Muon System Performance

System performance was explored using the current track parameter program developed for the EEoI [29]. In addition to the general behavior of the momentum resolution, two specific indices of the performance of the system were used for descoping and robustness studies:

- The mass resolution for muon decays of Z^0's resulting from the decay of a heavy (800 GeV) Higgs,
- The invariant mass resolution for a heavy multi-TeV Z′ decaying to muons.

The first involves muons typically in the 100–300 GeV region and probes the low-energy performance of the system, while the second involves muons in the 500–5000 GeV region and monitors the high-energy behavior of the system.

These quantities had been studied for the preparation of the EEoI, and results were presented for a range of possible magnets including the EEoI baseline. Separation of the first two superlayers, which in the EEoI design for the central toroid were collected into one compact group, tends to improve the resolution and mitigates the effect of decreasing the depth of the field region [30]. In addition to the spacing between the first two superlayers, the parameters that were varied in these studies were: [31]

1) The maximum field in the central and end toroids;
2) The thickness of the central and end toroids;
3) The outer radius of the end toroid;
4) The separation of the two superlayers before and after the toroids;
5) The cell size in the muon detectors.

The new baseline system presented in this LoI was arrived at by balancing the figure of merit indices against pattern recognition performance, robustness, and cost. The important changes in the system parameters that emerged are:

1) In the end toroid, the maximum field has been decreased from 4.5 T to 3.5 T and the thickness decreased from 4.0 m to 3.5 m;
2) The thickness of the central toroid has been decreased from 3.0 m to 2.0 m;
3) The cell size of the muon detectors has been increased from 2.0 cm to 2.5 cm;
4) The number of layers in the first superlayer after the toroids has been decreased from 16 to 12;
5) The number of nonbend plane layers after the toroids has been halved;
6) The two superlayers before the central toroid have been separated and moved further away from the calorimeter;
7) Space point measurement has been added in the superlayers using strip readout in conjunction with the wire readout to assist in pattern recognition and track identification.

Figures 3-25 and 3-26 show the momentum resolution of the EEoI system and the current baseline.

To investigate the response of the system in the event of a failure of the first superlayer to provide a useful or unambiguous track, studies were made of the performance with an inefficient first layer. The momentum resolution of the system in the case of complete failure of the first superlayer is shown in Fig. 3-27.

The effects of random misalignment or uncompensated displacements of detector wires within a detector layer or of a whole group of detector layers has been discussed in detail [32, 33]. In Figs. 3-25, 3-26, and 3-27 the effects of random misalignments for the the wires within a superlayer (σ_{INT}), and for the superlayers with respect to each other (σ_{EXT}), of 50 and 25 μm respectively have been included.

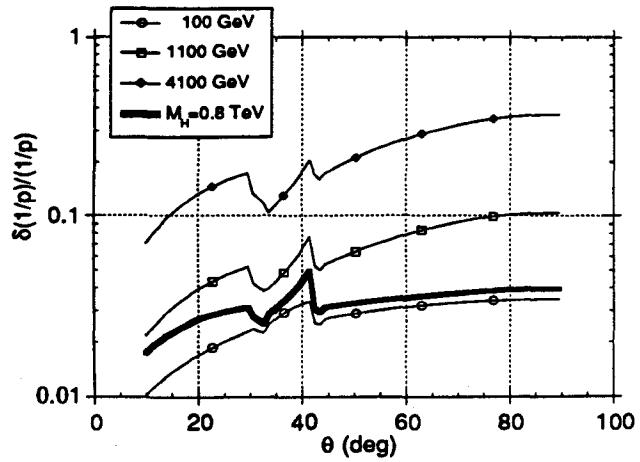

Figure 3-25 Momentum resolution for the EEoI baseline muon system.

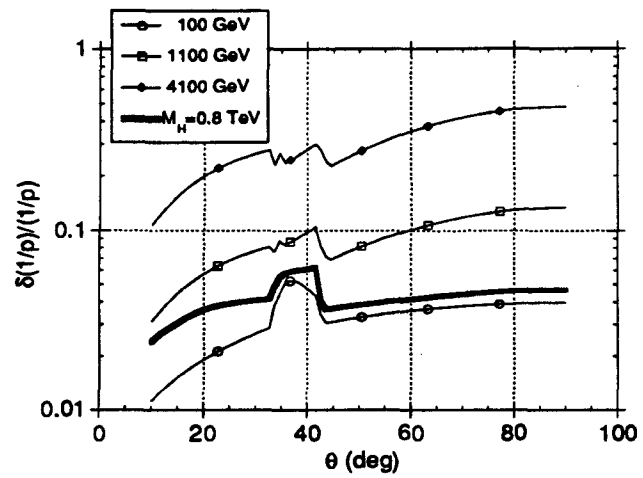

Figure 3-26 Momentum resolution for the LoI baseline.

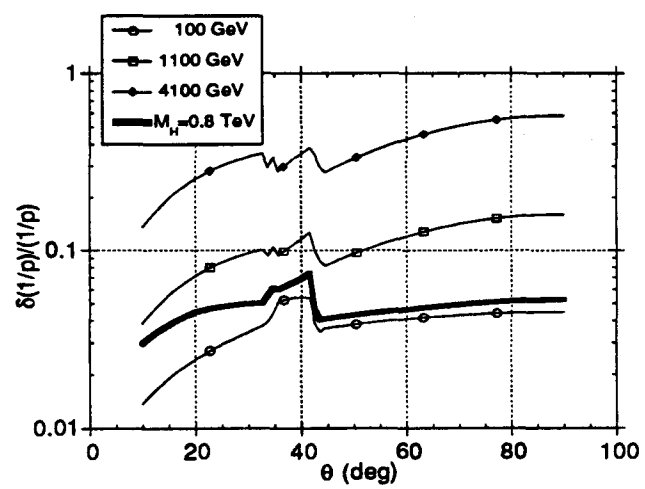

Figure 3-27 Momentum resolution for the LoI baseline missing signal from superlayer No. 1.

In Table 3-6 the mass resolution for the Z^0's from an 0.8 TeV Higgs is listed for the EEoI system, the new LoI baseline, and several other cases of interest.

Table 3-6 Z^o mass resolution for 0.8 TeV Higgs mass for various conditions.

	dM/M (%)	Conditions
1-	2.30 ± 0.13	EoI Parameters
2-	2.97 ± 0.17	Descoped System Parameters (LoI)
3-	3.40 ± 0.20	LoI - Missing 1st Superlayer
4-	3.16 ± 0.18	LoI σ_{int} = 100μm; σ_{ext}= 50μm
5-	3.07 ± 0.18	LoI σ_V= 400 μm; Including Azimuthal Variation Of Coil Structure
6-	6.78 ± 0.40	LoI - Missing 1st and 2nd Superlayers; σ_V= 400 μm
7-	8.36 ± 0.49	Iron Core Toroid - 1.8 Tesla, 2m Thick Barrel; 3m Thick Ends

In general, the mass resolution is worse by 30–50% for the new baseline because of the need to reduce costs. However, the system has been made more robust. The high-energy resolution is mainly limited by the measuring system (i.e., by the single-point resolution, the number of detector layers, the separations between the superlayers, the quality of the alignment, etc.) while at low energies the limitation is primarily caused by multiple scattering. The degradation in the high-energy performance can be partially overcome if a measurement of the event vertex can be made with sufficient precision. This effectively gives another measurement of the trajectory at the event vertex with a corresponding large lever arm. In Fig. 3-28 the variation of the momentum resolution at 4.1 TeV with the precision of the vertex determination is given. It is clear that a vertex determination in the several hundred μm region will improve the resolution significantly. Recent beam tests of the straw TRD systems obtain angular resolutions consistent with 400 μm vertex precision [34, 35]. In Fig. 3-29 the effect on the Z′ mass resolution of the imposition of various vertex constraints is shown. The 100 μm curve corresponds to the improvement one could get with a high-quality pixel vertex detector.

In Fig. 3-30 the momentum resolution of the downscoped system including the 400 μm vertex constraint is given. This figure, rather than

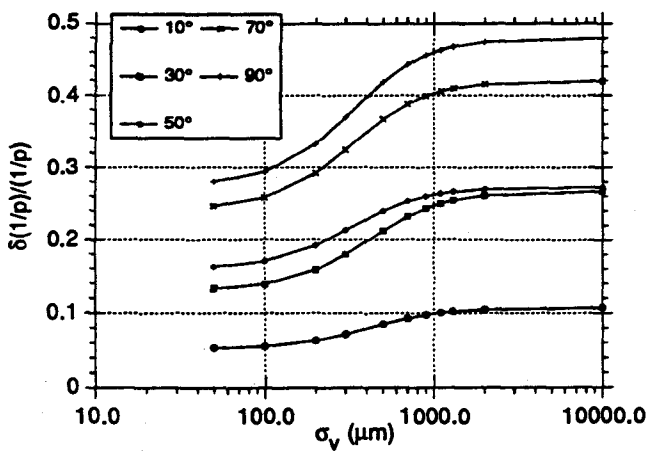

Figure 3-28 Momentum resolution for a 4.1 TeV muon as a function of the precision of the vertex constraint.

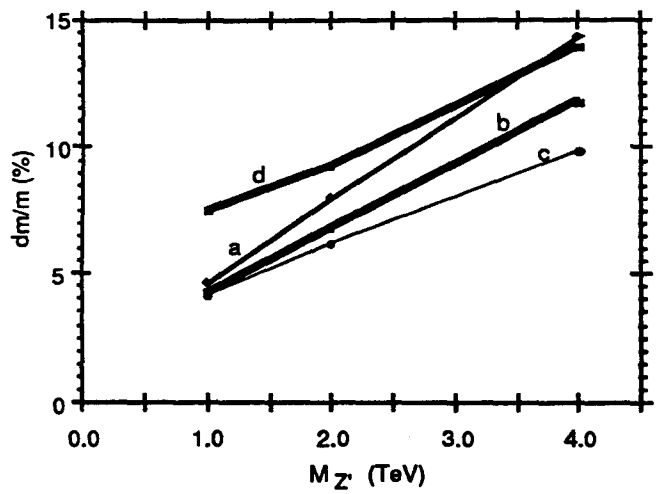

Figure 3-29 Mass resolution for $Z' \rightarrow \mu^+ \mu^-$; (a) σ_V = 10,000 mm; (b) σ_V = 400 mm; (c) σ_V = 100 mm; (d) σ_V = 400 mm and missing superlayers No. 1 and No. 2.

Fig. 3-26, represents the true baseline resolution for the muon system.

The most stringent test of robustness of the muon system occurs if the first two superlayers fail. In that event there still exists a point-line measurement of the tracks with the inclusion of the vertex measurement. Figure 3-31 shows the momentum resolution of the system without superlayers 1 and 2, using only the vertex measurement with resolution 400 μm before the toroid. Entry 7 in Table 3-6 gives the effect on the Z^0 mass resolution and the curve in Fig. 3-29 shows the effect on Z' mass resolution. It is clear that while performance of the system is significantly degraded at low energies the high-energy behavior is essentially retained. Because it is the highest momentum muons that are most likely to occlude their own tracks, this provides a significant demonstration of the overall robustness.

Figure 3-32 summarizes some of the effects on the momentum resolution that have been discussed in this section for 500 GeV muons.

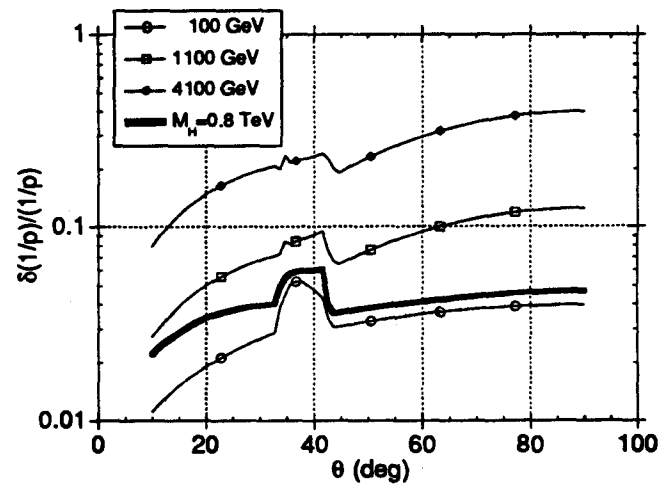

Figure 3-30 Momentum resolution for the LoI baseline system including a vertex constraint of 400 μm.

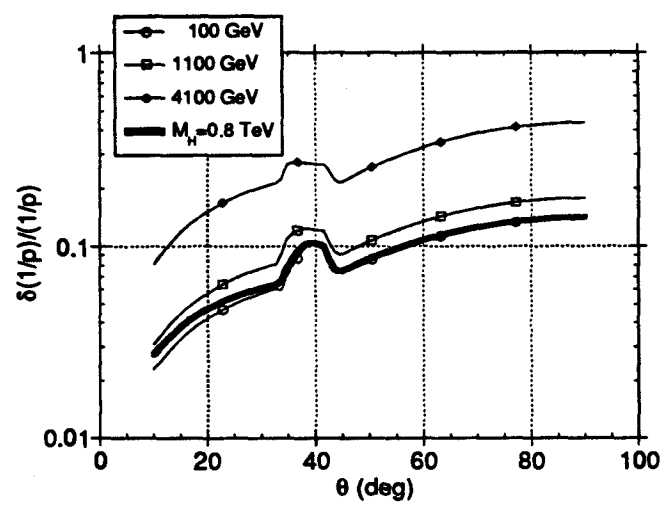

Figure 3-31 Momentum resolution for LoI with missing superlayers No. 1 and No. 2.

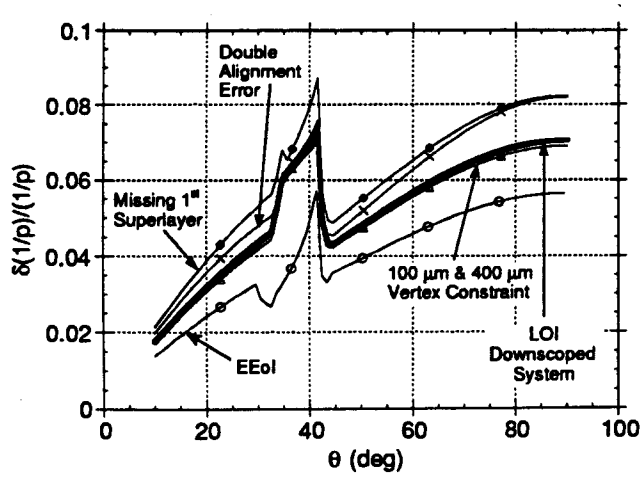

Figure 3-32 Momentum resolution of various system configurations for 500 GeV muons.

REFERENCES

1. F. Halfen, *et al.*, "EMPACT Cost Study," EMPACT/TEXAS Note 353 (1990).
2. P. Bonanos, "Toroid Conceptual Design," EMPACT/TEXAS Note 183 (1990).
3. J. Luton, "Feasibility of Low-Mass Conductor for Toroidal Superconducting Magnets for the SSC Detector," Proceedings of Symposium on Detector R&D, and EMPACT/TEXAS Note 213 (1990).
4. Y. Yanagai *et al.*, Cryogenics V29 #7, p. 253-257, July '89.
5. P. N. Haubenreich *et al.*, "The IEA Large Coil Task," Fusion Engineering & Design, Vol. 7, Nos. 1 & 2, September 1988.
6. K.Fujii *et al.*, Nucl. Instrum. & Methods **A225**, 23 (1984).
7. F. Gasparini *et al.*, Nucl. Instrum. & Methods **A267**, 87 (1988).
8. G. D. Alekseev *et al.*, "The Results of Mass Testing of the Plastic Streamer Tubes for DELPHI Hadron Calorimeter," submitted to Nucl. Instrum. & Methods.
9. A. C. Benvenuti *et al.*, Nucl. Instrum. & Methods **A290**, 353 (1990).
10. D. Hungerford *et al.*, "Operation of Limited Streamer Mode Production Line Chambers with Non-flammable Gases," Nucl. Instrum. & Methods. **A286**, 155 (1990).
11. R. Weinstein, "Comments on Wastage for Streamer Chambers," EMPACT/TEXAS Note 360 (1990).
12. Yu. Bonyushkin *et al.*, "Proposal for Tomograph Coordinate Calibration of Drift Tube Packages," EMPACT/TEXAS Note 241 (1990).
13. H. W. Kendall *et al*, Testing of Drift-Streamer Mode with a Laser Beam," EMPACT/TEXAS Note 358 (1990).
14. G. Charpak *et al.*, Nucl. Instrum. & Methods **A167**, 455 (1979).
15. L. S. Barabash *et al.*, Preprint IHEP 83-182, Serpukhov (1983).
16. Yu. Bonyushkin *et al.*, "Strip Readout and Detector Tolerances," (to be published); Yu. Bontyushkin *et al.*, "Readout for EMPACT Muon System Detectors: Strip Readout Studies," EMPACT/TEXAS Note 327 (1990).
17. J. J. Connelly, "A System Concept for Aligning the EMPACT Muon Detector Chambers for the Super Conducting Supercollider," EMPACT/TEXAS Note 225 (1990)
18. R. Solomon, "Error Analysis of Alignment Concept," EMPACT/TEXAS Note 365 (1990).
19. T. Majors, *et al.*, "EMPACT/TEXAS Electronics Cost Estimate," EMPACT/TEXAS Note 338 (1990).
20. Yu. Bonyushkin *et al.* "First-Level Muon Trigger," EMPACT/TEXAS Note 328 (1990).
21. A. Kulik, "Forward Muon Rates and Shielding" EMPACT Note 330 (1990).
22. W. Chou, SSC Technical Note (1990).
23. R. R. McNeil, "Punchthrough Simulation Studies for a Precision Muon Spectrometer Based on Superconducting Air Core Toroids," EMPACT/TEXAS Note 240, (1990).
24. A. V. Lanyov, "Characteristics of Electromagnetic Showers," IHEP Preprint IHEP 89-145, (1989); submitted to Nucl. Instrum. & Methods.
25. R. K. Adair, "Radiation from Muons Passing Through Matter," EMPACT/TEXAS Note 182, (1990).
26. R. P. Kokoulin, "Calculation of Energy Losses of Muons Through Iron and Lead," EMPACT/TEXAS Note 333 (1990).
27. R. R. McNeil, "Radiation of Muons in EMPACT/TEXAS," EMPACT/TEXAS Note 357 (1990).
28. K. Lau *et al.*, "Streamer Chambers for Muon Tracking at the SSC," to be published in the Proceedings of the Symposium on Detector R&D for the SSC, Ft. Worth (1990).

29. L. Rosenson, "Momentum Resolution and Track Reconstruction Quality for the EMPACT Detector," EMPACT/TEXAS Note 224 (1990).
30. R. K. Adair, "Iron Toroids," EMPACT/TEXAS Note 273 (1990).
31. L. Rosenson, "Studies of the EMPACT/TEXAS Muon Spectrometer Directed Towards Robustness and Descoping," EMPACT/TEXAS Note 354 (1990). One important improvement in the scope of the program is the inclusion of the azimuthal variation of material in the magnet; viz. the 72-fold periodicity of the coil structure including the supports.
32. "EMPACT Responses to SSC PAC Questions," EMPACT/TEXAS Note 244 (1990).
33. L. Rosenson, "The Effects of Misalignment on the Track Reconstruction in EMPACT," EMPACT/TEXAS Note 239 (1990).
34. A. Romanyuk, "TRD/Tracker: Beam Test Results of a Prototype," EMPACT/TEXAS Note 292 (1990).
35. V. Polychronakos, Paper presented at Symposium on Detector Development for the SSC, Fort Worth, Texas, October 1990.

4.0 TRACKING AND PARTICLE IDENTIFICATION

4.1 INTRODUCTION

Tracking in EMPACT/TEXAS has two primary functions: to observe the event topology-charged particle multiplicity and primary vertices and to provide particle identification capability. These functions are supplemental to the primary goals of the study of electrons and jets by high-performance calorimetry and of muons in the air-core toroid system. Particle identification goals are the separation of photons from electrons and from neutral pions, the separation of electrons from other charged particles and from photon conversions, and possibly the identification of high-momentum tracks in a transition radiation detector (TRD). Leptons will be key to much of the most exciting SSC physics, and this detector is designed for optimal lepton performance.

The optimization of the tracking and particle identification system will be done by selecting from a range of proven technologies. Where detector systems have redundant or complementary capabilities, trade studies will assess the capability of the combined tracking and calorimetry systems to deliver the required tracking efficiency and resolution, particle identification, and calorimetric energy resolution. Tracking system components under consideration include a TRD, silicon vertex detectors, gaseous pixel detectors, tracking by scintillating fibers or by scintillator-filled capillary tubes, a preshower detector of lead and either scintillating fibers or capillaries, and pads of either silicon or scintillator.

4.2 DESCOPING OF THE TRACKING SYSTEMS

The goal in descoping is to reduce the cost of the tracking and particle identification system while maintaining performance. Several possible approaches are shown, and the current concept should be recognized as a first cut at optimizing the tracking systems.

The present baseline tracking concept does not include a vertex detector. This represents a significant loss of capability because this system provided the ability to observe secondary vertices and to tag low-momentum particles by their scattering, as well as redundant particle identification and improvement of high muon resolution [1]. The azimuthal tracking functionality of the vertex system has been integrated into the preshower detector as discussed below. Interest in a vertex detector is still high; R&D will be pursued and cost and performance effectiveness reevaluated during the full system optimization.

The number of channels in the TRD has been reduced by 25% to approximately 290 000. The coverage has been reduced from $\eta < 3$ to $\eta < 2.5$, and redundancy in the various sections on the TRD also reduced. Refinement of mechanical issues and costs will be required before specifying an optimal system. In particular, development of an inexpensive mechanical design looks encouraging. However, to meet the required reduction it may be necessary either to increase the straw size by approximately 7%, from 4 mm to 4.3 mm, or to reduce the number of straw layers traversed by a particle from 48 to 44. Detailed study and simulations will be required to evaluate these alternatives.

Azimuthal tracking capability has been modified and integrated with the TRD/tracker. Pad detectors, either silicon or scintillator, tile the front face of the TRD and form a projective structure matched to the calorimeter towers. Outboard of the TRD an integrated tracker and preshower detector provides measurement of track position in r-ϕ and detailed information on electromagnetic shower development. A second layer of pad detectors following the preshower detector measures the energy flow entering the calorimeter. Adequacy of this overall design for pattern recognition will be studied by simulating the integrated systems.

4.3 BASELINE DESIGN

We have devised a baseline system specification for the tracking and particle identification system that meets the descoping goals with minimal sacrifice of detector capabilities. The design is shown in Fig. 4-1.

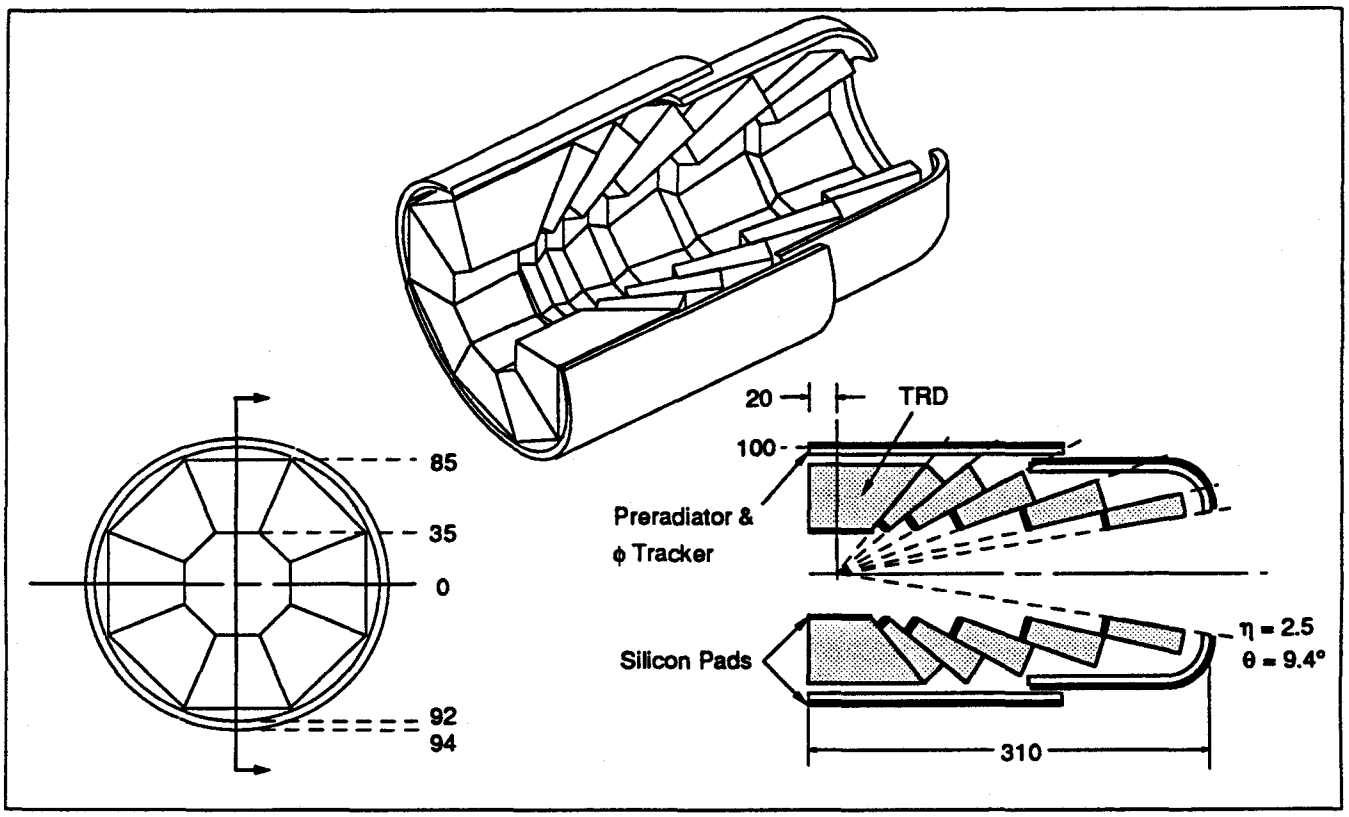

Figure 4-1 Side and beam views of tracking/particle identification system (dimensions in cm).

A tracking TRD and an integrated azimuthal tracker and preshower detector are sandwiched by layers of pad detectors that projectively match with the calorimeter towers.

The front pads mounted on the face of the TRD/tracker detectors may be silicon, with 300 μm of active material plus wiring and support structure totaling less than 1% X_0. Alternatively, these detectors could be 4 mm thick scintillator pads with embedded wavelength-shifting fiber coupled to clear fiber for readout. These plastic pads plus supports and packaging have approximately the same thickness in radiation lengths as the silicon devices. The pads in front of the TRD, in conjunction with pads just before the calorimeter, define roads to guide pattern recognition. The front pads also identify photon conversions and multiple particle pileup. The pads preceding the calorimeter provide a measurement of the energy flowing into the calorimeter, allowing effectively complete correction for energy deposition in the preshower detector and preserving excellent calorimeter resolution. There are 15 000 pads per layer in the fiber calorimeter option and 31 000 pads per layer in the LAr option (due to the finer segmentation).

The tracking transition radiation detector is based on azimuthally oriented proportional straws embedded in polyethylene foam that provides mechanical support and is the radiator in which particles with high Lorentz γ will emit transition radiation. The straws will detect the passage of ionizing particles and the x-ray transition radiation. This detector provides highly redundant tracking in the r-z plane [2]. The design in Fig. 4-1 is based on modules that provide complete coverage to $\eta = 2.5$. The modules form a series of stacked octagonal prisms. The modules on each side of the interaction region project to a point displaced from the origin by 20 cm, which is 4 σ in the event vertex distribution. This avoids potential problems where tracks can slip through the interfaces between modules. This design incorporates approximately 290 000 channels. The performance of the prototype TRD/tracker has been measured in beam tests.

Based on the test results the TRD/tracker has been estimated to have resolution of approximately 400 μm on the z position of a track at the entrance to the calorimeter. This provides rejection capability against false electron candidates caused by overlap of EM showers and low momentum hadrons. The resolution of the z position of a track extrapolated back to the beam line is approximately 400 μm/ $\sin^2(\theta)$. The vertex position, defined by several tracks, is known with better than 400 μm precision. This vertex resolution increases the lever arm for the input track to the muon system and thereby increases the precision of the muon momentum measurement at high momenta.

By measuring the transition radiation yield, the TRD/tracker rejects low-momentum pions with a rejection power better than 10^{-2} while maintaining 90% efficiency for electrons. It also identifies photon conversions and Dalitz pairs with high efficiency. The test results have been used to study simulations of the TRD. The measured energy loss distributions versus impact parameter of the track (with respect to the straw center) were input to the Monte Carlo simulation. The x-ray yields calculated in the Monte Carlo were checked against the test distributions.

Figure 4-2 plots the resulting hadron rejection power versus momentum, including the effects of overlap events as well as a high p_T events. The performance meets TRD design goals. Simulation of performance at higher luminosity is in progress.

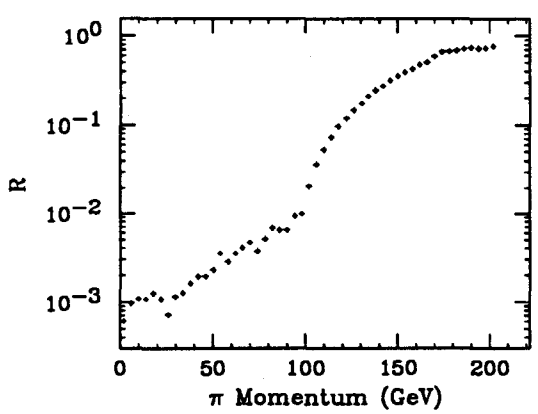

Figure 4-2 TRD pion rejection vs momentum from Monte Carlo including test results.

Outside the TRD/tracker is a preshower detector and azimuthal tracker. This concept has been studied in several variations using scintillating fibers [3], silicon detectors [4], scintillator-filled capillary tubes [5], or silicon pads [6,7]. For evaluation purposes, a system consisting of a 3 X_0 thick structure of 1 mm diameter scintillating fibers and lead is being considered. A cross section is shown schematically in Fig. 4-3.

It consists of a triple layer of axial fibers followed by three superlayers of fibers interleaved with lead. Each superlayer consists of three double layers of fibers that run axially and at +15° and -15° stereo angles, providing pattern recognition power and longitudinal position information. Two X_0 of lead follow the first superlayer and one X_0 of lead follows the second superlayer. A superlayer of fibers measures a track in the r-ϕ plane with precision of order 200 μm and in the r-z plane with precision of order 1 mm, complementing the coarse azimuthal measurement and more precise r-z measurements of tracks in the TRD. The tracking triple layer and the first superlayer together can track particles back to the beam line with typically 1 cm uncertainty in the transverse position. In this conceptual design, the barrel preshower detector fibers are split at the midplane so that each barrel fiber covers $\Delta\eta \sim 1.5$ and each end cap fiber covers $\Delta\eta \sim 1.0$. There are 36 000 fibers in each half-barrel superlayer and 32 000 fibers in each end cap superlayer; the triple layer counts as half a superlayer. The total fiber count is approximately 476 000.

The preshower detector recognizes false electron candidates that arise from the accidental overlap of charged particles and electromagnetic showers within the shower position resolution of the calorimeter. The resolution on shower origin has been studied in similar preshower detector tests. Resolution of better than 200 μm on shower position has been obtained [3]. Matchup of shower position and track position with this precision provides a high level of overlaps rejection that is largely independent of and complementary to the rejection power supplied by the transition radiation.

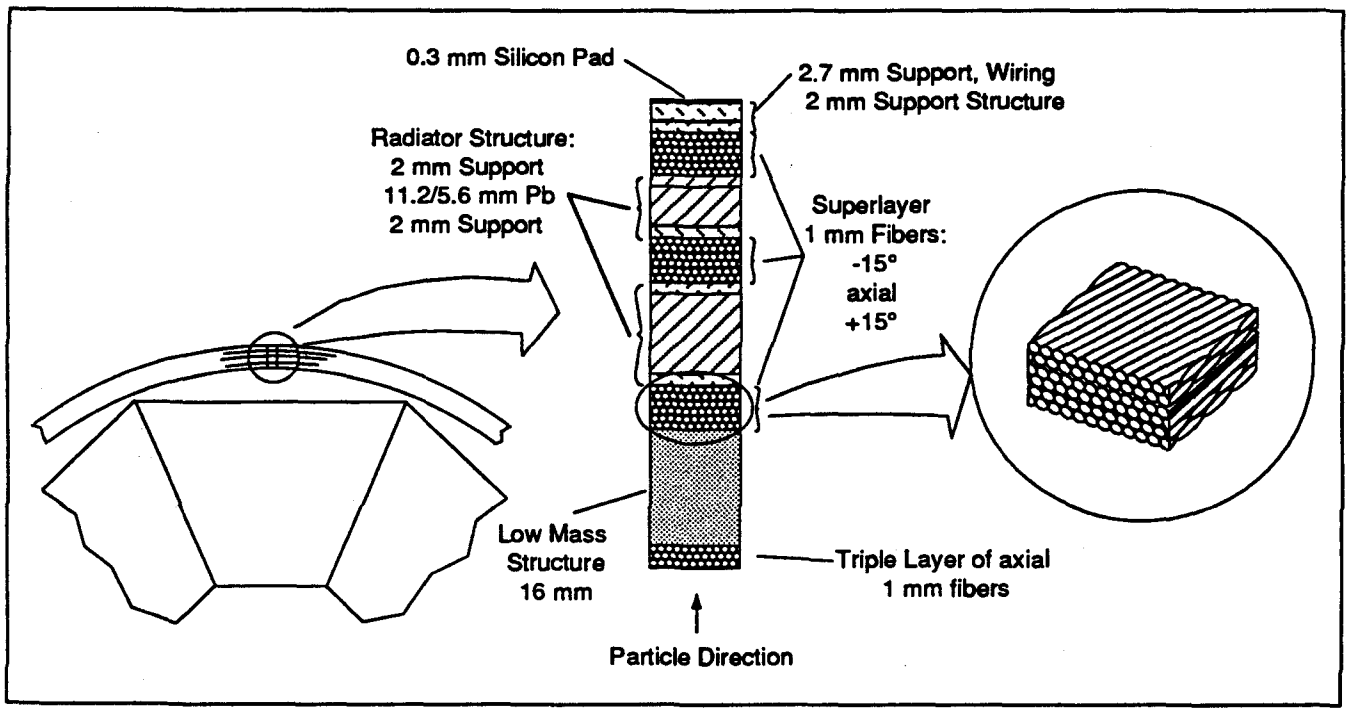

Figure 4-3 Details of the preshower detector/azimuthal Tracker.

The preshower detector contributes to the study of the two-photon decay of the light Higgs in two ways: (1) by providing a measurement of the electromagnetic shower position that, when combined with the position measurement in the calorimeter, can help reconstruct the event vertex and allow reconstruction of the two-photon mass and (2) by helping reject the π^0 background.

Shower position resolution of 1 mm is expected for isolated showers in the electromagnetic calorimeter. With a measurement less than the 200 μm level in each stereo view in the preshower detector and a lever arm of order 20 cm between the measurements in the preshower detector and the calorimeter, photon origin at the beam line can be reconstructed with a precision of 0.5 cm, which would contribute to reconstruction of Higgs decay candidates. The rejection of π^0's is accomplished by observing the origin and development of electromagnetic showers; cuts on moments of the longitudinal and transverse energy distribution provide some discrimination power between showers of a single photon and the two photons of a π^0. A detailed EGS Monte Carlo simulation of the preshower detector rejection of π^0's will be used to optimize the design of the preshower detector [8].

Integration of the pad layers, the TRD/tracker, and the preshower detector is not optimized. System optimization will require analysis of correlations and redundancy of the various components. A guiding principle in the system design is to minimize deleterious impact of systems on one another, while maintaining the highest level of complementary and redundant capabilities.

4.4 ELECTRONICS

4.4.1 Transition Radiation Detector Readout

Because of the large number of channels and high channel density, VLSI circuits will be developed to meet the TRD/tracker electronics requirements. In one concept, the signal processing for each channel proceeds through a preamp and shaper to digitization in two bits; this feeds a digital pipeline, which in turn feeds trigger processors and readout modules. The layout sketched in Fig. 4-4 is being considered for design purposes.

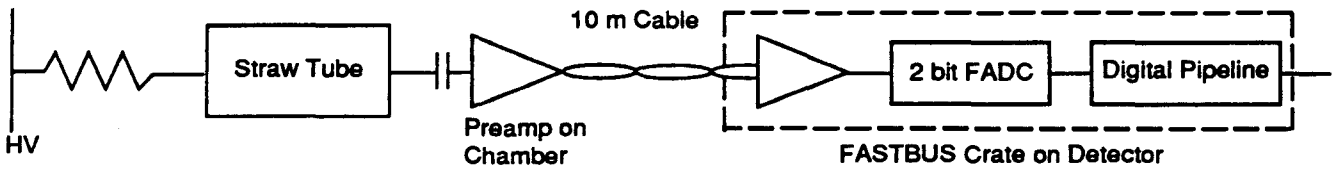

Figure 4-4 TRD electronics schematic.

The preamp is located at the straw end. A low-mass cable of order 10 m long carries signals to the shaper, digitizing circuit, pipeline, and processors, which are located in crates at the detector periphery.

The "cable-out" approach is a conventional and conservative design for which reliable costing can be done. The major challenge is to manage the cable plant. Available cabling is almost adequate for the task. With 30-gauge twisted pair, a gap of approximately 3 cm at 90 cm radius between the barrel and endcap preshower detectors would be required to bring out the TRD/tracker cables [9]. The thickness of this bundle is less than 0.5 X_0; most of the bulk is insulation. The design shown in Fig. 4-1 has an 8 cm gap between the barrel and end cap preshower detectors, sufficient to accommodate the TRD/tracker cabling and the optical fibers from the end cap preshower detector. Developing a custom cable is a straightforward option should commercial products prove too thick.

An attractive alternative to the conservative "cable-out" approach is to put the digitization and pipeline circuits on the chamber, giving performance advantages and minimizing cable plant. Another appealing alternative is to read out the proportional straws with optical modulators. In this approach, the proportional straw is attached directly to an electro-optic structure that drives an optical fiber running to the outside of the detector. This offers a low-mass compact solution to the cabling problem.

4.4.2 Readout of the Preshower Detector and Azimuthal Tracker

A number of approaches to the readout of the preshower detector are being considered. Given the large number of channels in these devices, it is important to develop a highly integrated and multiplexed readout to reduce system costs. In Europe and the USSR, systems using high-speed CCDs are under development for readout of a large number of imaging elements [10]. With optoelectronic delay and fast clear (1 μs), such a device can run at input event rates up to a 100 kHz. Readout times of order 1 ms are expected. Work is in progress to study the feasibility of this approach in the SSC environment. The separator tab preceding this section has a color image taken with a CCD system, showing the light from a minimum ionizing particle traversing an array of 30 μm inner diameter liquid scintillator-filled glass capillary tubes [11]. System resolution is quite impressive.

A similar approach to a highly integrated readout is a hybrid silicon detector/PMT such as the "pixie tube"[12]. An image intensifier stage is combined with a pixelized solid-state detector [13]. Photoelectrons are accelerated through a potential difference of order 10 kV and impinge on a pixel array of PIN silicon diodes, each with local intelligence. Single photoelectrons are estimated to give a signal 10 times the noise of the pixel. This highly integrated readout is fast, data-driven, automatically sparse, and has a linear response with excellent noise performance. Prospects for a very low per-channel cost make this technology especially important to pursue. Development is in progress in cooperation with industry [14].

Another technology under study applies avalanche photodiodes (APD) to the readout of tracking elements. These devices have some desirable characteristics, including high quantum efficiency and fast response time [15]. When operated in Geiger mode they are sensitive to single photons and produce signals of order 20 mV with no amplifier required. Alternatively, they can be operated in a linear response mode. The block diagram for such a system is similar to that shown in Fig. 4-4, and the per-channel cost is comparable. Work is in progress to develop arrays of APDs and to explore operation in the Geiger mode [16].

4.5 R&D RESULTS

4.5.1 TRD Prototype Beam Test Results

A straw tube TRD was tested this past June and July in the X5 test beam of the SPS at CERN. An event display is shown on the separator tab for this section. The detector consists of 4 TR modules each containing 20 x 3 straw tubes. The straw tubes are made of 64 μm thick polycarbonate and are placed in holes drilled in a polyethylene foam block that acts as the radiator. The foam has a density of 59 kg/m^3 and an average wall thickness of 5 μm. Previous tests of this foam shows an x-ray yield 85% of a regular stack of foils. The gas used in the straw tubes for most of the testing was 50% Xe, 50% CO_2. Later runs were made with a LeCroy 9424 digital scope connected to one channel just after a special, very fast preamp. The recorded waveform has been used to study the effect of the shaping amplifier.

Analysis of the data is in progress [17, 18]. The yield of high-threshold hits per straw traversal is shown in Fig. 4-5.

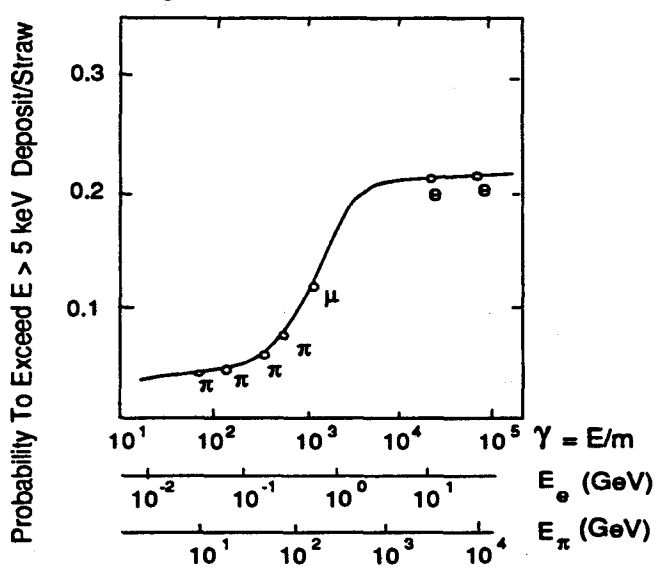

Figure 4-5 Probability of high-threshold hits vs Lorentz gamma.

Monte Carlo simulations of this detector configuration are in progress in an attempt to understand the TR x-ray yield and pion rejection for isolated tracks. These data are being used to tune the Monte Carlo program that simulates the full central TRD/tracker. Preliminary results show good correlation with earlier Monte Carlo results, as discussed in Section 4.3.

Tracking performance of the device was studied by comparing measurements of line fit slopes and intercepts, using the hits in even-number and odd-numbered columns separately. The results (Fig. 4-6) demonstrate track slope determination to a mrad and intercept determination to better than half a mm. The SSC detector performance should be at least this good per track, and multiple tracks can be used to define the vertex z position with even more precision. As discussed in Sect. 3.4.4, measurement of the vertex position to a precision of 400 μm dramatically improves the precision of muon momentum measurement at high momentum.

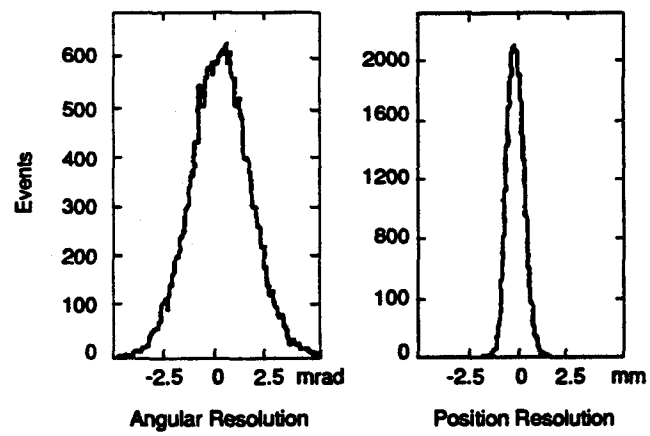

Figure 4-6 TRD angular and projected position resolution from beam tests.

Waveforms from the test beam were digitized at 400 MHz and recorded. We have used these data to emulate the performance that would be achieved in readout electronics with different integration times. The results of one study are shown in Fig. 4-7. For integration times of order 10 ns, a factor of 2.5 improvement in two-pion rejection is seen in comparison with performance at longer integration times. This work will be an important input into the design of the next prototype tests scheduled for the coming summer. Detailed understanding of pulse shaping is required for prediction of TRD performance at the high occupancies associated with operation at high luminosity.

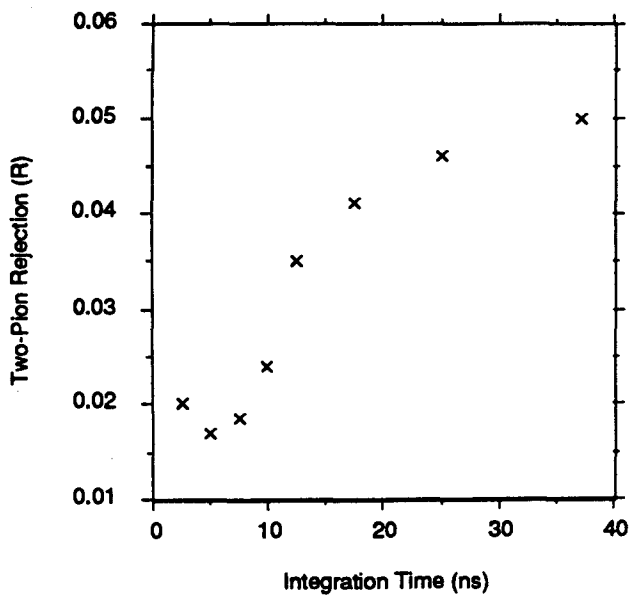

Figure 4-7 Two-pion rejection in TRD vs effective integration time.

4.5.2 Mechanics of TRD Construction

Some progress has been made in the development of alternative construction techniques for the TRD proportional chamber array. It is advantageous from several points of view—mechanical complexity, assembly time, cost—to simplify the structure and eliminate the straws. Progress has been made in developing molded polyethylene structures. Half cylinders are molded into the foam, and an aluminum coating is vacuum deposited by standard industrial process. The foam is the transition radiator and provides structure for the entire detector. The aluminization provides both a continuous cathode surface and a barrier against xenon permeation into the foam. A sketch of the foam structure is shown in Fig. 4-8.

Circuit boards are glued to the ends of the molding in a manner that permits open stringing. In mass production, stringing could be done by robotic equipment that places wires at high speeds—15 meters/minute—and can servo wire placement with optical sensors to meet the accuracy required [19].

A prototype of such a proportional detector has been built. Performance measured with radioactive sources is comparable to what is achieved with straw proportional chambers. While the good performance is very encouraging, much additional work remains to be done; it will be important to verify the beam performance of such a device and to study the uniformity achievable in mass production.

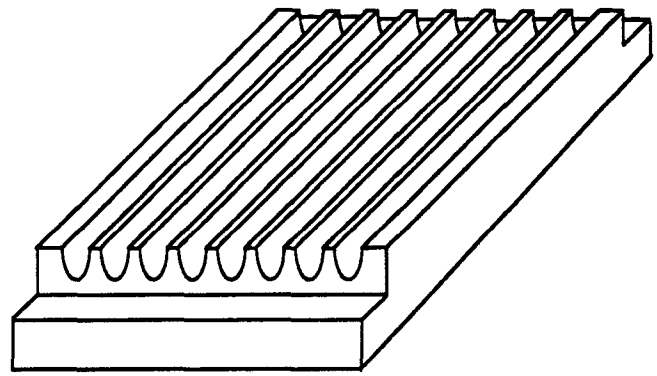

Figure 4-8 Molded polyethylene foam structure for strawless TRD design.

4.5.3 Preshower Beam Test Results

A fine-grained scintillating fiber preshower detector has been built and tested in a beam of pions and electrons [3]. The detector had eight superlayers separated by 1/4 X_0 lead sheets; the super layers consisted of pairs of fibers at 0, +15, and -15 degrees from axial, as discussed in Sect. 4.3. Shower centroid resolution was measured by comparing the centroid position in the fourth superlayer with the prediction from a line fit to the centroids in the other superlayers; this gave a resolution of better than 200 μm. Analysis of test results has shown that sampling later in the shower development contributes most to particle identification and shower position resolution, and that samples early in the shower development contribute less. The layout shown in Fig. 4-3 as a baseline preshower detector design is based on these test results and the results from Monte Carlo studies of several alternatives [7, 20]. Optimization will be pursued by both additional beam tests and continuing Monte Carlo studies.

4.5.4 Performance of a Pixel Vertex Detector

We have studied the possible performance of a pixel vertex detector [21], that incorporates three layers of pixel detectors [22], with 6000 cm^2 of detectors. The high-resolution tracking capability of this detector in both azimuthal and longitudinal directions allows reconstruction of primary and secondary vertices and improvement of momentum measurement precision at high momentum. Low-momentum tracks can be tagged, by observation of their scattering in the several percent of radiation lengths in the detectors, and eliminated from consideration in finding secondary vertices. It was found that particles under 1 GeV/c could be rejected with greater than 95% efficiency, while particles with momentum above 10 GeV/c were retained with greater than 97% efficiency. This tagging also aids in rejection of π/γ overlaps as a source of false electron candidates, providing a functionality redundant with the TRD in this respect.

4.6 PRINCIPAL R&D EFFORTS

The technical developments needed to realize the tracking technologies are challenging. Principal areas for futher R&D follow.

Transition Radiation Detector:

- Study performance of a 1200 channel prototype scheduled for the coming summer. The tests will consider the importance of pulse shaping and integrating times, and the pattern recognition and particle identification capabilities of a detector of realistic scale.
- Development of manufacturing techniques and designs for mass production of radiator and detector assemblies.
- Study of optical modulators for readout of proportional signals, offering an elegant solution to the readout of densely packed channels.

Preshower Detector:

- Development of readout technologies for scintillating fibers is crucial to the viability of the fiber approach. The pixie tube readout offers high capacity and low per-channel costs and needs to be pursued with vigor. Development of techniques for high-speed operation of CCD-based systems should be continued, with application to both the readout of scintillating fibers and scintillator-filled capillaries. Fast clearing is of special importance there. Development of APDs with multiple device packaging is important for tracking applications (Geiger operation) and as an alternative readout for preshower fibers.
- The silicon detector preshower technique should be pursued [23]. The good detector resolution and straightforward manufacturability of this approach make it appealing; development of low-cost detectors and pad structures is important.

Vertex Detector:

- Research during the coming year will include collaboration in prototype tests of pixel devices; development of mechanical designs; and study of pattern recognition, tracking, and vertex finding. We hope to find a way to include this detector within the constraints of the budget limitations. The vertex detector adds to the scope of the physics that can be achieved and provides redundancy for the other systems.

REFERENCES

1. "EMPACT - Responses to PAC Questions," EMPACT/TEXAS Note 244 (1990).
2. "The EMPACT Experiment at the SSC," SSC-EoI-0006 (1990).
3. P. Cushman, ECFA Study Week on Instrumentation Technology for High-Luminosity Hadron Colliders, Barcelona, Spain, 14-21 September 1989, p. 187; P. Cushman *et al.*, presented at the SSC R&D Symposium, Fort Worth, TX, October 1990; J. Alitti *et al.*, Nucl. Instr. Meth. **A273**, 135 (1988); D. R. Wood, Nucl. Instr. Meth. **A289**, 331 (1990).
4. D. J. Munday *et al.*, CERN/DRDC/90-27, 2 August 1990.

5. S. Golovkin *et al.*, EMPACT/TEXAS Note 312 (1990); O. V. Buyanov *et al.*, EMPACT/TEXAS Note 313 (1990); A. G. Denisov *et al.*, IHEP preprint 90-96, Protvino (1990); A. Artamonov *et al.*, CERN-EP/90-58.
6. G. Bashindzhagyn, "Silicon Preconverter for the Barrel Calorimeter of EMPACT/TEXAS," EMPACT/TEXAS Note 298 (1990).
7. K. Pitts and J. Brau, "The Effect of a Pre-radiator on the Electromagnetic Energy Resolution for the EMPACT/TEXAS Liquid Argon Calorimeter," EMPACT/TEXAS Note 341 (1990).
8. A. S. Johnson, "π^0 Rejection in Preshower Monte Carlo," EMPACT/TEXAS Note 337 (1990); P. Cushman, private communication.
9. T. Majors *et al.*, "EMPACT/TEXAS Electronics Cost Estimate," EMPACT/TEXAS Note 338 (1990).
10. O. V. Buyanov, EMPACT/TEXAS Note 313 (1990); T. Gys *et al.*, CERN 89-10, V. 1, 255 (1989).
11. S. V. Golovkin, "Tracking and Preshower Detectors Based on the Capillaries with Liquid Scintillator for the EMPACT Experiment," EMPACT/TEXAS Note 294 (1990).
12. D. R. Winn *et al.*, presented at the SSC R&D Symposium, Fort Worth, TX, October 1990; P. Cushman, private communication; G. Alverson *et al.*, "Subsystem Proposal for Pre-Shower and Shower-Maximum Detectors," submitted to SSCL, September 1990.
13. See for example D. Nygren, "Silicon Tracking Devices for the SSC," Proceedings of the Summer Study on High-Energy Physics in the 1990s, Snowmass, July 1988.
14. P. Cushman, private communication; Positive replies to a Request for Proposals have been received from Hamamatsu, Burle, and Delft Electronische Producten.
15. R. J. McIntyre and A. W. Lightstone, Proceedings of the Workshop on Tracking Systems for the Superconducting Super Collider, Vancouver, Canada, July 24-28, 1989, p. F57.
16. S. Reucroft *et al.*, presented at the SSC R&D Symposium, Fort Worth, TX, October 1990.
17. V. Polychronakos *et al.*, presented at the SSC R&D Symposium, Fort Worth, TX, October 1990.
18. A. Romanyuk, "TRD/Tracker: Beam Test Results of a Prototype," EMPACT/TEXAS Note 292 (1990).
19. L. Scheiber, Advanced Interconnection Technology, Islip, NY, private communication.
20. P. Cushman, "Monte Carlo Studies of the Preshower Detector," EMAPCT/TEXAS Note 344 (1990).
21. V. Cook and P. Mockett, "A Precision Vertex Chamber for EMPACT/TEXAS," presented at the SSC R&D Symposium, Fort Worth, TX, October 1990.
22. S. Shapiro *et al.*, SLAC PUBs 5212 (May 1990), 5357 (October 1990) and 5358 (October 1990).
23. G. Bashindzhagyn, "Silicon Detector R&D Plans Moscow State University for EMPACT/TEXAS," EMPACT/TEXAS Note 345 (1990).

5.0 ELECTRONICS, DATA ACQUISITION, AND COMPUTING

5.1 FRONT-END ELECTRONICS

Electronic designs considered thus far have been based on current technology to provide a basis for cost estimation [1]. The conservative choice of technology assumes a minimum amount of circuitry will be detector mounted. Moreover, the designs assume circuit densities (channels per board) no greater than those of today's commercial products. These choices are not final, but are intended to provide a standard against which advanced technology designs can be evaluated.

Although the performance of the reference designs meets our requirements, new technologies may provide better performance at considerably reduced costs. A number of promising options exist, but it is too early to judge their technical feasibility and ultimate cost with confidence.

R&D options currently under study include placing the complete front-end (preamp through readout) on the detector [2], the use of electro-optic modulators [3,4], and the use of superconducting electronics [5].

The payoff from on-detector mounting will be greatest for the central tracker because the number of cables that must penetrate the detector will be vastly reduced. This approach may also prove advantageous for the calorimeter and muon detector electronics, where cabling and connector cost reductions may be realized. This gain, however, must be weighed against the simplicity of conventional rack mounting, which leaves the readout electronics concentrated in a small number of easily accessible locations, rather than distributed over the detector. Because the gains associated with on-detector mounting are greatest for the central tracking system and because this system will probably not participate in the Level 1 trigger, the development of on-detector electronics for the central tracker will be given highest priority.

The suitability of electro-optic modulators to the readout of SSC detectors is currently being investigated [3,4]. In this technique, externally generated laser light is piped into the detector through single-mode fiber-optic light guides, each of which services several channels. The light is split and modulated on a channel-by-channel basis by detector-mounted electro-optic modulators, driven by the electrical signals from the detector preamplifiers. The individually modulated signals are brought out on multimode fibers to externally mounted photodetectors. This technology has several advantages: high dynamic range, a high bandwidth, very low power dissipation at the detector, and a low mass compact solution to the cabling problem by using optical fiber to carry data to the outside. Recent results [5] indicate electro-optic modulators may be sensitive enough to allow direct connection to the detector's electrical outputs without the need for preamplifiers. Once again, the potential advantages are largest for the central tracking systems. Because the area required per fiber is a small fraction of a mm^2, cabling for the entire central detector can be reduced to a fiber bundle of only a few hundred cm^2. Finally, if the signals are carried on spatially coherent fiber bundles, triggering via optical pattern recognition may also be possible [3]. It remains to be demonstrated that reasonable per-channel costs can be achieved for large-scale systems [4].

Josephson junction devices may also play a role in the front-end and trigger electronics. They are inherently low power and radiation hard. One disadvantage is the need to interface both the mechanical connections (normally at 4 K) and the logic levels to the standard room-temperature devices. A combination 10-bit 100-MHz ADC and a 1 μs digital pipeline, consuming less than 1 mW of power per channel, has already been developed [6].

The current program will examine and evaluate these options.

5.2 LEVEL 1 AND LEVEL 2 TRIGGERS

A description of the Level 1 and Level 2 triggers can be found in the EEoI. Additional information on the first layers of the Level 1 trigger for the calorimeter and the muon systems can be found in Sect. 2.0 and Sect. 3.0 of this document.

5.3 READOUT AND THE LEVEL 3 RANCH

Level 2 will produce between 100 and 1000 events per second, each several MBytes in size. The readout system must therefore be able to transfer data to Level 3 at rates approaching 10 GBytes/sec. Level 3 must provide an additional event rejection factor of 100 before the data are sent to mass storage and monitoring programs using a large farm (ranch) of parallel processors.

The long timeframe before SSC operation and the very rapid escalation of the power of computer components make it difficult to design and cost a Level 3 system in any detail. The current explosion in silicon-based RISC processors will likely continue as gallium arsenide (GaAs), and perhaps superconducting electronics technologies come to fruition.

GaAs technology has in fact already matured to the point where digital VLSI ICs can be produced as a matter of routine. For example, working microprocessors have been produced for use in spacecraft control systems [7]. Part of this system is shown on the separator tab preceding this section. This processor, which is capable of running at clock speeds of 200 MHz, replaces a conventional processor and provides an 8-fold increase in speed while requiring less than one tenth the space. The problems faced in satellites are similar to the SSC detectors: enormous amounts of input data from varied sensors and a limited bandwidth on the satellite downlink to Earth.

The design problems presented by the readout and Level 3 system are well matched to the capabilities of digital GaAs technology. GaAs circuits have been fabricated at densities in excess of 50 000 FETs per chip, have been operated over an extended temperature range (-55 to +125°C), and have survived radiation exposures greater than 60 Mrad. The design work for the satellite processor can be extended to the Level 3 ranch. Although the current version is 16 bits, there is no difficulty in expanding the design to 32 bits. Nonproprietary Ada and C compilers are currently available and a FORTRAN compiler is being developed. Software developed for the earlier satellite microcomputers can be ported to the new digital GaAs processor without changes.

The speed advantages of GaAs may be even more important for readout and event building where flexibility of operating some circuit paths at speeds greater than 1 GHz may prove crucial. Figure 5-1 shows a generalized architecture of a single CPU in the Level 3 ranch. The figure indicates that a set of high-pincount GaAs VLSI microcontroller devices receive the incoming data stream. In the satellite application, such devices were used to perform complex arithmetic operations such as channel-to-channel correlations and threshold detection. Analogous functions in a system designed for event readout (data sparsification, gain correction, etc.) will offload processing requirements from the CPU ranch. Figure 5-1 also shows that a special integrated circuit will be developed to interface the GaAs processor to FASTBUS or any other required network. This will ensure that each processor can be loaded in "broadcast" mode, and that the processing capabilities of the CPU farm can be enhanced simply by adding additional units. This interface also allows downloading of events from the mass storage device for extended offline analysis.

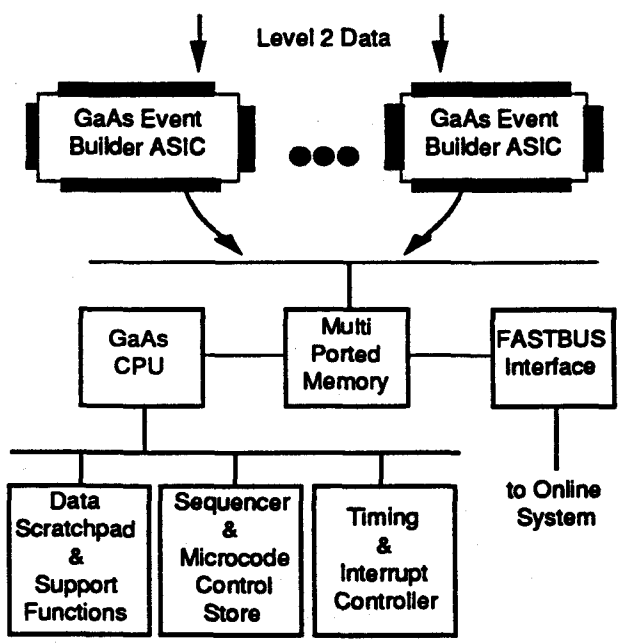

Figure 5-1 Generalized architecture of a CPU in the Level 3 ranch.

Josephson junction technology may also be employed in the readout and Level 3 ranch. A 128 x 128 crossbar switch capable of 2 Gbit/sec operation could considerably simplify the readout and is being developed [5]. Also under development is a 2-GFLOPS wafer-scale integration RISC processor.

5.4 ELECTRONICS COSTS

Detailed breakdowns of the front-end electronics costs and a description of the estimation methods can be found in Sect. 7.0. In view of the difficulties inherent in estimating costs of the more advanced technology options, the cost estimates are based on conservative and conventional designs where experience permits reliable estimates. New technologies will not be employed unless they are at least equally cost effective, thus the numbers resulting from this approach are upper bounds. Conservative design assumptions lead to conservative cost estimates.

For reasons previously stated, it is difficult to determine the cost of the Level 3 ranch with precision. The assumption of 75K MIPS at $100 per MIPS is already very close to being satisfied by commercially available RISC-based processors. Extrapolating price performance trends of the past 5 years would, in fact, result in considerably lower costs per MIPS.

The total cost of signal handling, starting at the detector elements and extending through to the Level 3 ranch, is approximately $100 per channel when averaged over all channels.

5.5 OFFLINE COMPUTING

5.5.1 Management

The large task of defining the future direction in offline computing has already begun. The code includes simulation, pattern recognition, offline reconstruction, and the online system. To deliver the necessary software in time will require management of manpower resources, computing hardware, and the enforcement of some minimal set of standards to which all code must adhere to achieve compatibility.

Software system managers for the various areas of code have been appointed: online, tracking and pattern recognition, calorimeter simulation, and reconstruction, etc. These people will be based at various U.S. institutions; in each case there will be a corresponding Soviet representative so that physicists in the USSR can coordinate activities.

5.5.2 Central Group

The collaboration is already at the point at which a central library of offline code needs to be maintained in a systematic manner. As soon as possible after the approval of the project, such a central code library should be established at the SSCL, using the new UNIX computing resources available in early 1991. The library will be updated with new versions of application code developed by physicists and programmers elsewhere, and periodically new "releases" will be made to the collaboration as a whole. Preliminary discussions have been held on how such a code distribution system might be arranged.

At least one full-time programmer will be needed to update the library and perform the releases. In addition, the central collaboration computing group should be in residence at the SSCL. This group will be responsible for structural (framework) aspects of the code. Low-level routines (utilities to read event files, unpack banks, and so forth) will be independent of the high-level routines, (jet-finding algorithms, etc.) so that either may evolve without major dislocation to the other.

The central group will initially consist of 3–5 programmers and 2–3 physicists, steadily increasing over the course of the project to 20–30 programmers and 10–15 physicists. There will be an overall software coordinator responsible for ensuring that the experiment has access to all the software systems that it needs to function adequately. This person will be resident at the SSCL as part of the collaboration's central computing group. The SSCL should provide adequate office space for these people, and a computer system tailored to program development, including a workstation for each person and several GBytes of disk storage accessible from all stations.

5.5.3 Standards

To take full advantage of new hardware technology and to expedite the development and maintainability of software will require the establishment and enforcement of a set of well-thought-out software standards. These standards have been defined and are embodied to a large extent in the simulation code already written. Standard event formats, common blocks, and subroutine naming conventions will be defined as soon as possible, so that programs can be slotted together in a modular manner.

Codes will be developed in a machine-independent way, allowing full advantage of the computing resources that are spread over a variety of operating systems: VMS, UNIX, VM, Cray UNICOS, etc. Machine-independent code will also facilitate the migration of offline reconstruction and Monte Carlo programs to the Level 3 ranch, allowing that powerful system to be fully utilized.

5.5.4 Networking

Offline computing is one area in which large contributions are expected to be made from physicists "at home" in their universities and laboratories, and not at the SSCL. The effectiveness of this mode of operation is determined by the quality of networking available between member institutions.

Networking must provide the following facilities:

- Distribution of project documentation and mail;
- Access to central program libraries;
- Database-read operations from remotely running programs;
- Cooperative software development and analysis projects;
- Bulk data transmission (DSTs, engineering CAD files, etc);
- Task-to-task communication.

Within the U.S. existing ESnet connections among collaborating institutions, and between them and the SSCL, are of reasonably high standard (a number are T1 lines), and an effective communication tool at present. Nonetheless, a careful review of network needs must be undertaken as bandwidth requirements undoubtedly rise.

One way to enhance connectivity among the institutions is to form an advanced engineering design network for the SSC with the assistance of the Texas National Research Laboratory Commission [8]. This calls for a high-bandwidth network based on ESnet for the distribution of engineering and simulation data that would encompass a number of EMPACT/TEXAS institutions (but be available for general SSC detector use).

Among Soviet institutions, connectivity is, at present, of a much lower standard, although an internet link to CERN was established last month. It is hoped this will change by 1993 with the inception of a project centered at Moscow State University known as "Radio MSU." This is a digital star network with 2 Mbps bandwidth that will transparently link local area networks at high-energy physics centers. Communication between the USSR and U.S. can presently be made through land lines from the Moscow IAS center to CERN, but this link is not very reliable and speed is limited to 4800 bps. A satellite link is the preferred option, and the possibilities are being worked on at this time by JINR (Dubna). Discussions have been held with the Swiss PTT about creating a link from Dubna to CERN using two channels on an INTELSAT VA-F10 communications satellite. The procedural problems seem to have been overcome and restrictions on the export of communications equipment are no longer a hindrance. Currently, progress is governed by availability of funds. Initiation of a satellite link to Dubna for general high-energy community use has been proposed and financial assistance from the SSCL is requested. The cost is estimated to be $80 000 startup and $80 000 per year for the link via CERN; it may prove simpler to locate a suitable ground station within the U.S. instead of using CERN.

5.5.5 Offline Computing Hardware

Computing hardware requirements for the short term will be focused on code development, physics simulation, and engineering design.

Institutional facilities and the central group system at the SSCL described above will be used for code development. Physics simulation over the next few years, will be run primarily using ISAJET and GEANT (or programs of similar complexity). Typical events will take approximately 130 MIPS-minutes to generate based on the current program. Large event records are anticipated: The size should be similar to DØ sizes where full Monte Carlo events are 2 MBytes each. Three types of simulation runs are foreseen:

Physicist Runs—500–1000 events on a workstation, with the aim of simulating some particular signal of interest. This would take 2 to 5 days on a 20 MIPS machine and fill 1–2 GBytes of storage (or a single 8 mm tape). This type of system will be available at most collaborating institutions.

Production Runs—10^5 events generated in about 8 weeks, with the aim of providing a large sample of events for development of filtering algorithms. This will require 160 MIPS (probably eight dedicated 20 MIPS nodes in a cluster), and four 1 GByte disks for staging and would write two 8 mm tapes per day for a total of 100 tapes. This type of system should be available at a number of the larger collaborating institutions.

Background Runs—10^6 events generated in about 8 weeks, with the aim of providing a very large sample of events to study rare backgrounds (e.g., calorimeter resolution fluctuations giving large missing transverse energy signals). This will require 1600 MIPS of CPU, 40 GBytes of staging storage, and write 20 tapes per day. This is only feasible at the SSCL using the new 5000 MIPS computer acquisition and would need a full-time data aide to handle bookkeeping tasks and tape handling. SSCL is requested to be prepared to support this level of use of the facility by the collaboration.

An analysis of computing needs for the DØ upgrade indicates a need for an offline reconstruction capacity of about 5000 MIPS for the anticipated recording rate of 10 events/second. In addition, if one assumes that comparable Monte Carlo statistics (10^8 events/year) will be needed once running, the total required offline capacity will approach 25 000 MIPS for EMPACT/TEXAS. Some of this capacity can be provided by the Level 3 ranch, but because that system will not be available while data is being taken, a substantial (10 000 MIPS) system dedicated to offline analysis will be needed.

REFERENCES

1. T. Majors *et al.*, "EMPACT/TEXAS Electronics Cost Estimate," EMPACT/TEXAS Note 338 (1990).
2. See, for example, A. Bhattacharya *et al.*, "Front-End Electronics Development for SSC Detectors," SSC Subsystem R&D Proposal (1989); C. Blocker *et al.*, SSC Progress Report/Renewal (1990).
3. M. Lowry, presented at the SSC R&D Symposium, Fort Worth, TX, October 1990; M. Lowry *et al.*, "A Proposal for Electro-Optic Front-End Electronics for the SSC," October 1990.
4. V. Radeka, presented at the SSC R&D Symposium, Fort Worth TX, October 1990; Report of the TRD Collaboration, SSC Subsystem Report, September 1990.
5. M. Lowry, private communication.
6. E. Stebbins, H. Caswell, and J. Wikswo, "Applications of Superconducting Electronics for the SSC," SSC R&D Symposium, Fort Worth TX, October 1990.
7. S. Espy and M. Schneiderwind, "System Upgrade of a Spaceborne Processor Using Digital Gallium Arsenide Technology," Government Microcircuits Applications Conference, November 1989; D. Krening and R. Schneiderwind, "A Behavioral Language Model Simulation of a GaAs CPU," Government Microcircuits Applications Conference, November 1990; S. C. Espy and M. J. Schneiderwind, "Meeting System Upgrade Criteria with Digital GaAs Microcircuits," Government Microcircuit Applications Conference, November 1990.
8. T. Bowen, *et al.*, "An Advanced Engineering Network for SSC Detector Design," Proposal to the Texas National Research Laboratory Commission, October 1990.

6.0 PHYSICS

6.1. INTRODUCTION

It is known from unitarity bounds on weak cross sections that there is new physics at mass scales ≤ 1 TeV. This new physics may only be a minimal Higgs boson of the standard model, or it may include more unexpected phenomena such as supersymmetry, quark compositeness, nonminimal Higgs doublets, new gauge bosons, or possibilities as yet unimagined. Whatever discoveries await us, the signatures are sure to be formed from combinations of the familiar quanta of the standard model: jets (quarks and gluons), electrons, muons, photons, W and Z bosons, and noninteracting particles (neutrinos, light supersymmetric particles) that are measured as missing transverse energy. None of these quanta can be neglected, because in many cases the signatures for new particles involve combinations of them. Therefore, EMPACT/TEXAS has been optimized with precision measurement of all these quanta firmly in mind. This balanced approach to electron, muon, jet, and missing-p_T decay modes augurs well for our ability to detect unknown and unexpected processes, while our high rate capability enables us to operate at higher than the design luminosity and thus to detect rare processes.

6.2. SIMULATION TOOLS

The simulation of physics processes requires two stages: event generation, in which the physics of a given interaction process is modeled; and simulation of the detector response. We have used the standard ISAJET [1] and PYTHIA [2] programs to generate pp events at the SSC. We have begun the modeling of the detector using GEANT, and some of the studies described below use the full rigor of this approach. We have made modifications to GEANT to increase the speed by parametrizing the low-energy tails of showers [3]. In many cases it is not necessary to use such a detailed simulation, and the detector resolutions are put in by smearing the particle momenta and direction according to the calculated resolutions.

This collaboration's simulation studies have been innovative in the use of a 3-D "CAD system" engineering model for physics purposes [4], taking advantage of the very detailed and faithful 3-D representation of the detector to estimate the calorimeter resolution as a function of incident particle energy and direction by tracing rays through the model.

The TRD/tracker system has a dedicated simulation package that uses results from 1990 beam tests at CERN. This does full geometrical and physics simulation and includes dE/dx losses and x-ray production mechanisms that are not supported by GEANT.

In the analyses presented here, events have been generated with ISAJET unless otherwise stated. The calorimeter segmentation is taken as $\Delta\eta = \Delta\phi = 0.05$ with resolutions from the CAD model for the central and end cap calorimeters and the transition between them at $\eta \sim 1.5$. This approach does not yet give good results in the $\eta \sim 3$ transition from end cap to forward calorimeters, because of the complicated shower development in nonhomogeneous materials. Though this region represents only a small loss of acceptance for jets, it potentially dominates the missing p_T resolution. Therefore, a full GEANT simulation has been run for single particles in this region to determine the resolution for study of missing p_T signatures and backgrounds [5].

Generally, jet finding is done using a cone algorithm similar to that of UA1 with a cone size $\Delta R = \sqrt{\Delta\eta^2 + \Delta\phi^2} \leq 0.7$. Muon resolutions given by parametrizations calculated for the muon system have been used.

As explained in the EEoI, development is continuing both on an overall GEANT-based simulation package (integrating the TRD and muon systems) and on simulation based on a 3-D CAD model. In the long term, these two approaches will converge in a project [6] to develop a CAD-to-GEANT geometry converter. Future GEANT versions will include a more CAD-like geometrical system [7] facilitating this development.

6.3. PHYSICS QUESTIONS

The guidelines for LoI preparation requested that the detector capabilities for certain physics processes be explained. The responses to these requests follow.

6.3.1 Higgs Boson

Describe the capabilities of the proposed detector for searching for a standard model Higgs in the following mass regions:

$$80 < M_H < 180\ GeV$$
$$M_H \sim 200\ GeV$$
$$M_H \sim 400\ GeV$$
$$M_H \sim 800\ GeV$$

The Higgs search will be approached in various ways depending on the Higgs mass. For $M_H > 2\,M_Z$ the preferred mode is $H \rightarrow ZZ \rightarrow l^+l^-l^+l^-$ (l = e or μ). This can be extended somewhat below $2\,M_Z$ using the off-shell decay $H \rightarrow ZZ^*$, but for most of the intermediate mass range, $80 < M_H < 150$ GeV, the rare decay $H \rightarrow \gamma\gamma$ will be used [8]. A high-resolution electromagnetic calorimeter design has been adopted for this purpose.

6.3.1.1 Search for Intermediate Mass Higgs via $H \rightarrow \gamma\gamma$

This is the most promising channel to discover the Higgs for $80 < M_H < 150$ GeV, and measurement of the $H \rightarrow \gamma\gamma$ branching ratio is important to understand electroweak symmetry breaking [9]. The signal is a pair of isolated high-p_T photons; good energy resolution is required because of the high background of QCD $\gamma\gamma$ events. There is also an enormous background of QCD jets that must be rejected through isolation cuts, but recent measurements at LEP indicate that this is indeed possible [10]. Because the $\gamma\gamma$ branching ratio is quite small, running at high luminosity may be important.

Our simulation of $H \rightarrow \gamma\gamma$ is based on ISAJET with the detector simulation described earlier [11]. The production is dominated by gg fusion through top quark loops. The ISAJET $\gamma\gamma$ branching ratio has been increased by a factor of two to account for the $O(\alpha_s)$ QCD corrections, which reduce the $b\bar{b}$ decays, and the background process $gg \rightarrow \gamma\gamma$ [12] has been added.

The total cross sections for the Higgs signal and the QCD $\gamma\gamma$ background are about 160 fb and 1.1×10^3 pb respectively for $p_{T\gamma} \geq 10$ GeV/c and $M_H = M_t = 140$ GeV. In our analysis the following cuts have been made:

$$E_{T\gamma} \geq 20\ GeV,$$
$$\eta_\gamma \leq 2.5,$$
$$M_{\gamma\gamma} \geq 80\ GeV,$$
$$|\cos\theta_\gamma^*| \leq 0.7,$$

where θ_γ^* is the angle of a photon in the $\gamma\gamma$ rest frame. These cuts reduce the signal to 70 fb and the background to 45 pb.

The remaining background rejection must come from the mass resolution. The EM calorimeter is planned to have a resolution $\Delta E/E = 7.5\%/\sqrt{E} \oplus 0.5\%$, giving a $\gamma\gamma$ mass resolution of less than 1% within the mass range of interest. The other important contribution to the mass resolution is the determination of the vertex position. If there is only one interaction within the bunch crossing, the TRD tracker gives the vertex to within 400 μm, a negligible error. If there are a few vertices, choosing the highest multiplicity vertex as the $H \rightarrow \gamma\gamma$ one is usually correct.

At a luminosity of 10^{34} cm^{-2}sec^{-1}, there are typically 15 minimum bias vertices. Therefore, even if the tracking is still functional, one needs to determine the vertex from the photons themselves. The imaging preradiator and EM calorimeter have position resolutions of about 0.3 mm and 1.0 mm respectively. This results in a vertex position determination with $\sigma = 4.8$ mm for the 90% of the events that have at least one photon in the central calorimeter; the resolution is poor if both photons are in the end calorimeter. The resulting mass resolution is shown in Table 6-1. Evidently the vertex resolution of ~5 mm from the photons will not degrade the Higgs mass resolution significantly. This vertex determination is also useful at lower luminosities to separate multiple vertices.

Figure 6-1(a) shows the resulting two-photon mass spectrum with signals at 90, 110, 130, and 155

GeV/c^2 for one SSC year. The vertex pointing smearing is 5 mm, and the efficiencies for the vertex selection and photon selection (ε_γ=0.85) are included. The background subtracted spectrum is shown in Fig.6-1(b).

Table 6-1 Mass resolution in GeV for $H \rightarrow \gamma\gamma$.

Mass	δz = 0.4 mm	δz = 5 mm	δz = 5 cm
80	0.7	0.80	1.66
90	0.83	0.85	1.85
100	0.91	0.94	2.05
110	1.01	1.03	2.29
120	1.06	1.11	2.47
130	1.12	1.17	2.63
140	1.18	1.21	2.88
150	1.24	1.29	3.13
155	1.27	1.31	3.19

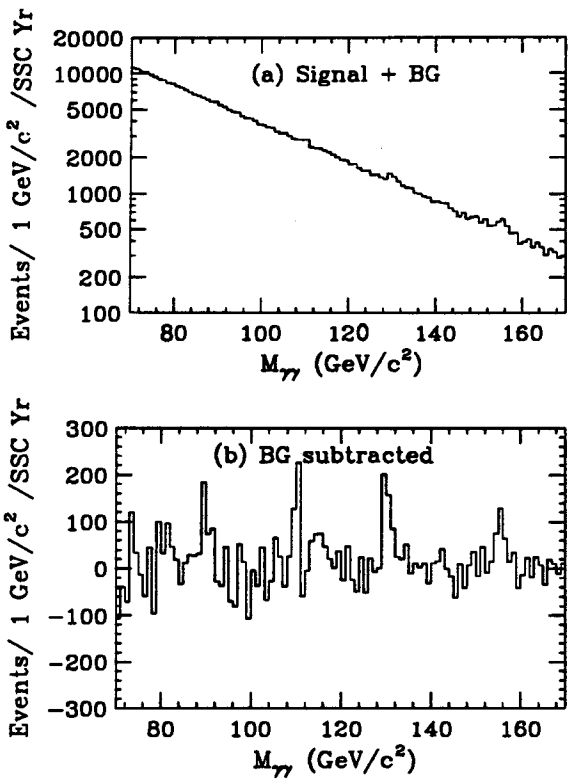

Figure 6-1 Invariant-mass distributions of photon pairs at an integrated luminosity of 10^{40} cm^{-2} for (a) signal ($gg \rightarrow H \rightarrow \gamma\gamma$), and background ($gg$, $q\bar{q} \rightarrow \gamma\gamma$), (b) with background subtraction. The event selection is made with $E_{T\gamma}$ >20 GeV, η_γ < 2.5 and $|\cos\theta_\gamma^*|$ < 0.7. Also included are the efficiencies of vertex reconstruction by a vertex pointing technique and two-photon selection due to an isolation cut, preradiator cut, etc.

The statistical significance for discovery may be expressed as $SS = N_S/\sqrt{N_{BG}}$, where N_S is the number of signal events estimated from the total number of events minus the number of background events (N_{BG}) in a window of $\pm 2\sigma_{mass}$. A summary of this study is given in Table 6-2.

Table 6-2 Significance of $H \rightarrow \gamma\gamma$.

Mass	N_S	N_B	SS	Δ(BR)
80	280	1.9×10^4	2.0	49%
90	320	1.4×10^4	2.7	37%
100	375	1.0×10^4	3.7	28%
110	427	7.7×10^3	4.9	21%
120	472	5.6×10^3	6.3	17%
130	500	4.1×10^3	7.8	14%
140	486	3.0×10^3	8.9	12%
150	401	2.1×10^3	8.7	13%
155	314	1.9×10^3	7.3	15%

Assuming a statistical significance SS > 5 is required for discovery, a Higgs in the mass region between about 110 and 155 GeV, will be found with an integrated luminosity of 10^{40} cm^{-2}. With an integrated luminosity of 10^{41} cm^{-2} and a vertex resolution of 0.5 cm, the reach extends down to 80 GeV. It must be recognized, however, that the signal-to-background ratio is very small.

If $H \rightarrow \gamma\gamma$ is discovered, it will be important to measure the branching ratio to verify the model. The statistical error in the rate for $H \rightarrow \gamma\gamma$ is given by $\sigma(N_S)/N_S = \sqrt{N_S + N_{BG}}\,/\,N_S$ and is shown in Table 6-2. Clearly, high luminosity is necessary to make even a relatively modest 5–10% measurement of the branching ratio.

The isolated $\gamma\gamma$ trigger rate is caculated to be 170 Hz after Level 1 and 7 Hz after Level 2, which should be quite manageable. This issue and others including the QCD jet background and the effect of pileup are discussed in detail elsewhere [12].

6.3.1.2 Search for Intermediate Mass Higgs via $q\bar{q} \rightarrow W\,H \rightarrow l\nu\,\gamma\gamma$

The low end of the intermediate mass range, 70 GeV/c^2 < M_H < 100 GeV, is very difficult, even at high luminosity. The process $q\bar{q} \rightarrow W\,H$ may be useful here [13]. The final state to be tagged is

$W \to l\,\nu$ with $l = e, \mu$, with the observation of an associated $H \to \gamma\gamma$ decay. The event rate has been calculated and is expected to be about 1 fb at the SSC. The principal background will be the standard model process $q\bar{q} \to W\,\gamma\gamma$. The background from misidentified electrons has not yet been studied.

Proposed cuts in the final state are:

$$E_{T\gamma},\ E_{T_l} \geq 20\ \text{GeV}$$
$$\eta_\gamma,\ \eta_l \leq 2.5$$

After the cuts, a large fraction of the signal events remains. The cross sections for $M_H = 70$, 100, and 130 GeV are estimated to be 0.45, 0.6, and 0.5 fb, respectively, and ~9 fb for the background events [13]. The selection efficiencies for photon, lepton, and neutrino are assumed to be $\varepsilon_\gamma = 0.85$, $\varepsilon_l = 0.85$, and $\varepsilon_\nu = 0.90$, giving a total efficiency $\varepsilon_\gamma^2\,\varepsilon_l\,\varepsilon_\nu = 0.55$. The estimate for ε_ν is based on CDF experience with W + jets events.

Figure 6-2 shows the $M_{\gamma\gamma}$ distribution for the signals ($M_H = 70$, 100, and 130 GeV) and the background at an integrated luminosity of 10^{41} cm^{-2}. The mass peaks for low mass Higgs are clearly seen. The statistical significance is calculated in the same manner as in Table 6-2 with the results given in Table 6-3.

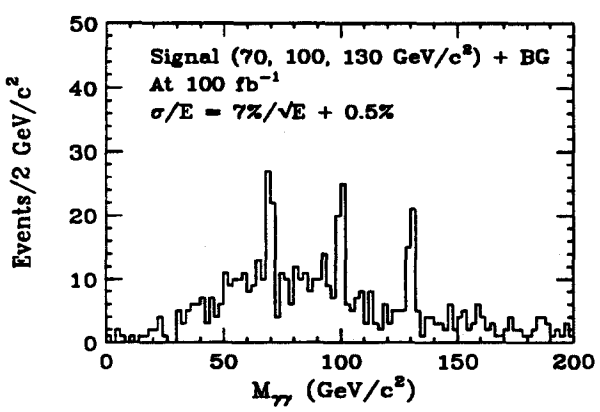

Figure 6-2 Invariant-mass distributions of photon pairs with $\Delta E/E = 7\%/\sqrt{E} \oplus 0.5\%$ at an integrated luminosity of 10^{41} cm^{-2} for $q\bar{q} \to WH \to l\nu\,\gamma\gamma$ (M_H = 70, 100, 130 GeV) and the standard model background ($q\bar{q} \to W\gamma\gamma$). The event selection is made with E_{Tl}, $E_{T\gamma} > 20$ GeV, η_l, $\eta_\gamma < 2.5$. The selection efficiencies for photon, lepton, and neutrino are also included.

Table 6-3 Significance of $HW \to \gamma\gamma l\nu$.

Higgs Mass (GeV/c²)	N_S (10 SSC yr)	N_B (10 SSC yr)	SS (10 SSC yr)	Branching Ratio Precision (10 SSC yr)
70	24	16	6.0	26%
100	32	13	8.9	21%
130	26	10	8.2	23%

These results should be compared with those in Table 6-2. Although the cross section is small, the smaller background actually improves the statistical significance at low M_H.

Figure 6-3 summarizes the discovery potential for Higgs in both $H \to \gamma\gamma$ and $HW \to \gamma\gamma l\nu$ channels. With an integrated luminosity of ~4×10^{40} cm^{-2} the entire range $M_H > 80$ GeV can be covered.

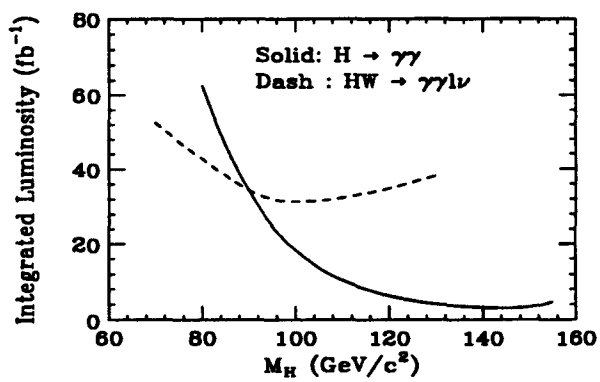

Figure 6-3 Integrated luminosity required for discovery of $H \to \gamma\gamma$ (solid) and $HW \to \gamma\gamma l\nu$ (dashed) as a function of M_H, requiring $\geq 5\sigma$ and ≥ 10 events.

6.3.1.3 $H \to ZZ^* \to l^+l^-l^+l^-$ (l = e or μ)

For $150 < M_H < 180$ GeV, we can search for the Higgs in the channel $H \to ZZ^* \to l^+l^-l^+l^-$ (l = e or μ)[14]. ISAJET was used to generate 1000 events for $M_H = 150$ GeV in the 4e, 4μ, and ee$\mu\mu$ channels. The lepton momenta were smeared with the standard electron and muon resolutions.

Four charged leptons are required with $p_T > 5$ GeV, $p > 6$ GeV, and $\eta < 2.5$. At least two of the leptons must have $p_T > 20$ GeV to allow a trigger. Two of the leptons must form a good Z having $|M_{ll} - M_Z| < 10$ GeV and the correct charge for muons. The other pair of leptons must have a mass between 10 GeV and 70 GeV. Finally, the leptons

must be isolated, with $E_T < 10$ GeV in a cone $\Delta R = 0.3$. Figure 6-4 shows the $H \rightarrow 4l$ signal and the $Z^0 b\bar{b}$ background for the $\Delta R = 0.3$ isolation cut. Within the Monte Carlo statistics all the background is eliminated for the $\Delta R = 0.4$ isolation cut. About 40 events are expected for an integrated luminosity of 10^{40} cm^{-2}. The statistics are quite limited, but the lack of background makes this an attractive channel for discovery of the Higgs in this mass range.

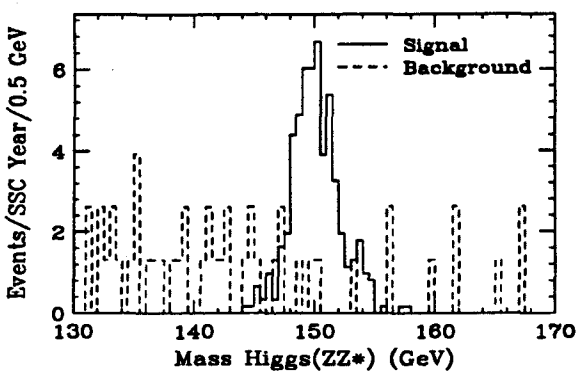

Figure 6-4 Reconstructed for $H \rightarrow ll$ mass and $b\bar{b}$ background for $\Delta R = 0.3$ isolation cut.

6.3.1.4 $H \rightarrow ZZ \rightarrow l^+l^-l^+l^-$ (l = e or μ)

For Higgs masses in excess of 200 GeV, the "gold-plated" channels $H \rightarrow ZZ \rightarrow l^+l^-l^+l^-$ (l = e or μ) are accessible. The discussion here primarily concerns the muon channel, because the electron resolution is certain to be good, and electron identification is not a serious problem with this well-constrained decay topology.

Samples of events for Higgs masses of 200, 400, 600, and 800 GeV were generated using ISAJET. The events were analyzed using the muon momentum resolution function described in Section 3.3, with the cuts $p_{T\mu} > 5$ GeV, $\eta_\mu < 2.5$, and $p_{TZ} > 50$ GeV. The combinations of oppositely charged pairs were chosen that gave masses closest to the Z^0, giving the Z^0 mass distribution shown in Fig. 6-5. This figure also shows the Z^0 mass for $H \rightarrow ZZ \rightarrow 4e$, assuming $\Delta E / E = 7.5\% / \sqrt{E} \oplus 0.5\%$. Good resolution is important to ensure good acceptance for Z^0's in the presence of high-mass dimuon backgrounds, especially if high-luminosity operation degrades information normally available from tracking or calorimetry [15].

Figure 6-6 shows the reconstructed 4μ invariant mass for Higgs decays and the ZZ continuum background for Higgs masses of 400 and 600 GeV.

The mass resolution can be improved somewhat by using a constrained fit, as shown in Fig. 6-7 and discussed in detail elsewhere [16].

For high p_T muons, one might sometimes lose the hit information in the first superlayer of muon chambers caused by muon bremsstrahlung or radiation in the calorimeter. If this happens, the $Z^0 \rightarrow \mu\mu$ resolution is only degraded from 2.4 GeV to 2.8 GeV.

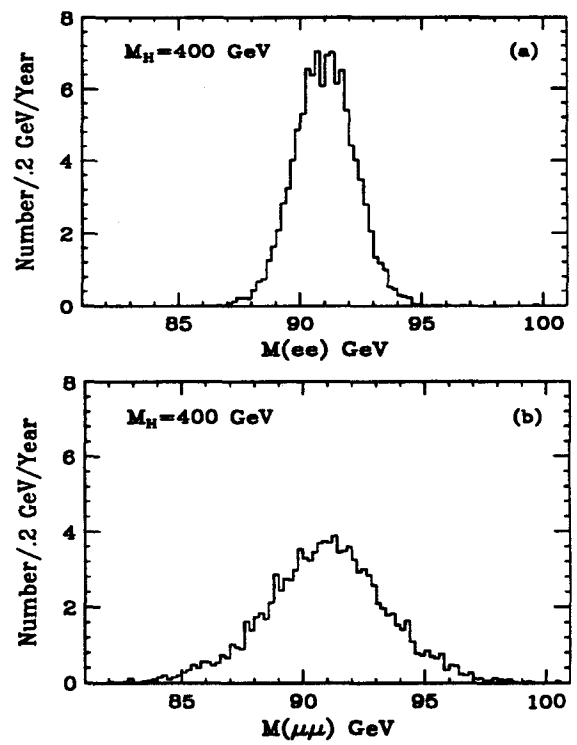

Figure 6-5 Reconstructed Z mass from from Higgs decay (a) ee pairs measured in the EM calorimeter and (b) $\mu\mu$ pairs measured in the air core toroid system.

6.3.1.5 $H \rightarrow ZZ \rightarrow l^+l^-\tau^+\tau^-$

The rate for 4e, 4μ, and $2e2\mu$ signatures is very small for heavy Higgs masses, at least for the standard machine luminosity. Events in which one Z decays to $\tau^+\tau^-$ can also be reconstructed. This gives a factor of two increase in the potential number of signal events.

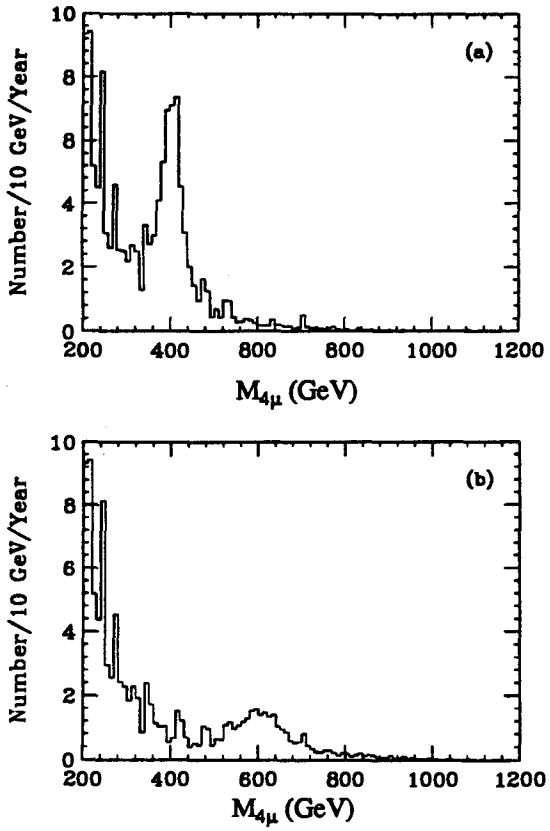

Figure 6-6 Reconstructed 4μ invariant mass for Higgs decays in the presence of ZZ continuum background for Higgs mass of 400 and 600 GeV. No mass constraints were used for the reconstruction of these events.

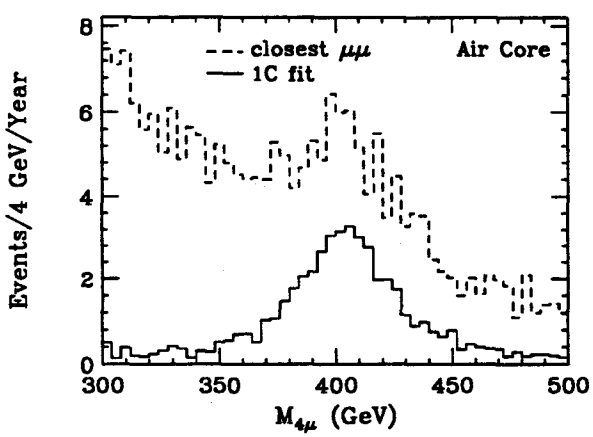

Figure 6-7 Reconstructed 4μ mass from 400 GeV Higgs decay using a constrained fit, with background muon pairs from $t\bar{t}$ production. Vertical scale is events for 10^{40} cm^{-2} integrated luminosity.

The τ decay products always include a ν_τ, and possibly other neutrinos that escape detection. However, the neutrino directions follow closely that of the parent τ, so their momenta can be deduced from the missing transverse momentum vector, which in a hermetic detector can be quite accurately measured. There are two neutrino energies to determine, and two components of missing E_T measured, enabling in general an unconstrained fit.

Only two sources of $Z^0\tau\tau$ events were considered: the Higgs events and the $q\bar{q} \rightarrow ZZ$ continuum. Because τ's could be identified from W decays at the SPS collider, it seems likely that the background for τ's will be very small at the very high p_T's of interest here.

ISAJET was used to generate 1000 events $H \rightarrow ZZ \rightarrow \mu^+\mu^-\tau^+\tau^-$ for $M_H = 600$ and 800 GeV. The τ decay products and other particles were simulated in a simple calorimeter. Jets with $\eta < 3$ were then found using a cone algorithm with $\Delta R = 0.2$, because the τ gives a narrow jet. A jet mass cut, $M_j < 4$ GeV, was imposed, and 70% of the E_T in $\Delta R = 0.5$ was required to be within $\Delta R = 0.1$. If more than two jets passed these cuts, the two with the lowest second moment of energy flow around the jet axes were used. For ττ masses with $|M_{\tau\tau} - M_Z| < 15$ GeV, the ττ mass was constrained to the Z^0 mass and the ττμμ mass was reconstructed. As shown in Fig. 6-8, the signal is clearly seen above the background for both 600 and 800 GeV Higgs.

6.3.1.6 $H \rightarrow ZZ \rightarrow l^+l^-\nu\nu$

The Higgs may also be discovered through the channels in which one Z decays to electrons or muons and the other to neutrinos. These channels have a factor of six more potential signal events than the four charged-lepton modes. The technique involves detecting the $Z \rightarrow \nu\nu$ through missing E_T in the event. If the missing E_T resolution of the calorimeter is not excellent, there will be a large background from QCD Z + jets events where the jets are mismeasured, leading to a false E_T signal. Therefore, it is important how well our calorimeter performs as a missing E_T detector. This channel is

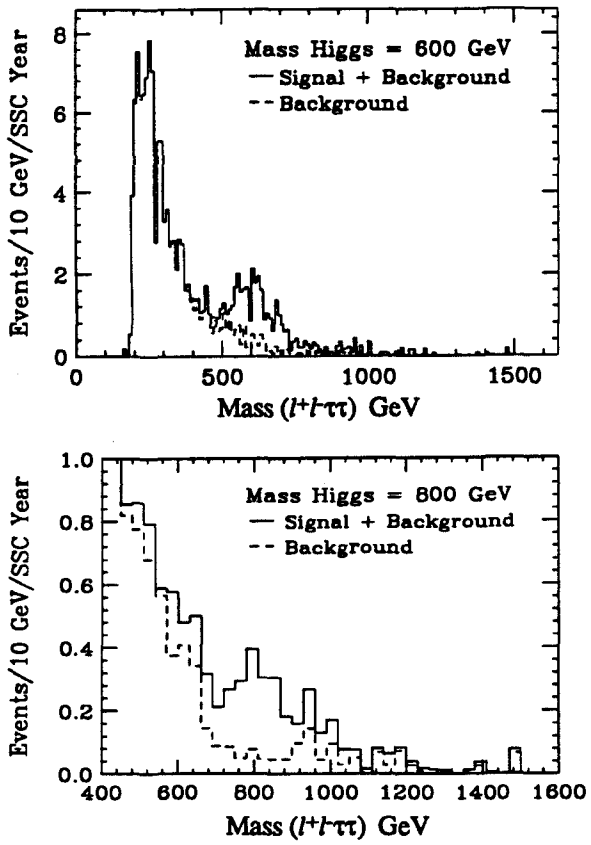

Figure 6-8 $\mu\mu\tau\tau$ invariant mass distributions from Higgs and $q\bar{q} \rightarrow ZZ$. (a) M_H = 600 GeV, (b) M_H = 800 GeV.

one of the most demanding in that regard, so it has been used as a principal benchmark for hermeticity.

The forward calorimeter coverage is split between end caps and forward calorimeter. This is done because previous studies [17] have indicated that to have sufficient missing E_T sensitivity, the calorimeter η coverage must extend up to $\eta \sim 5$. This is not possible without going quite far downstream. If, for example, the end cap calorimeter were simply closed down to the beam, showers around $\eta > 4$ would lose energy into the beam pipe because of the transverse shower size and the E_T uncertainty would be too large to attempt this search. Introduction of a forward calorimeter, however, necessitates a transition at $\eta \sim 3$. Figure 6-9 indicates the potential problem introduced by such a transition: showers can leak out of the sides of the "cone," leading to mismeasured E_T.

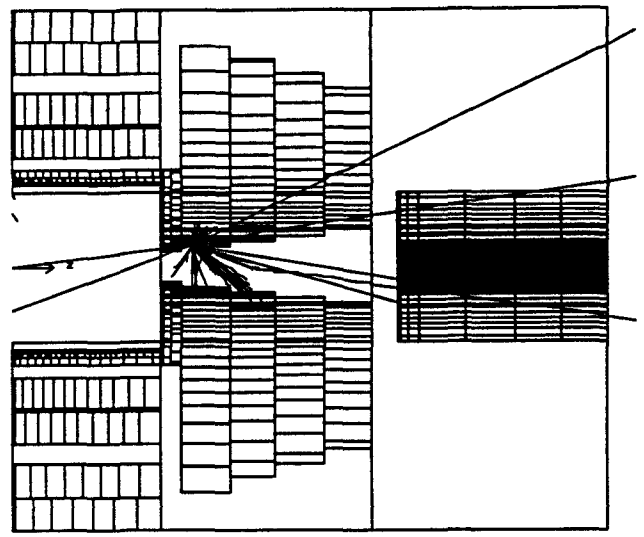

Figure 6-9 GEANT simulation of a single hadron shower in the end cap and forward calorimeter transition region.

Though it is visually dramatic, this leakage does not seriously compromise the hermeticity of the detector. To show this, GEANT was used to compile a library of showers in the region $2.5 < \eta < 3.5$. Then QCD Z + jets events were examined using this shower library to simulate the response of tracks in this region and the standard resolutions elsewhere. The resulting missing E_T distribution is shown in Fig. 6-10. Above about 50 GeV, the missing E_T mismeasurement is dominated by the decay of heavy quarks to neutrinos in the jets accompanying the Z. This sets a natural scale below which it is clearly not worthwhile to push the detector performance. With the $\eta = 3$ transition, the calorimeter measures E_T at this level.

Two other options have been investigated for the $\eta = 3$ transition, which are sketched in Fig. 6-11: an "inverse cone" and a cylindrical tube. These both spread the transition over a larger range of rapidity, while not creating such an extreme problem at exactly $\eta = 3$. For both of these cases, the missing E_T distribution is indistinguishable from that for the standard cone. The projective cone minimizes the η region over which the problem occurs and so probably simplifies the vetoing of bad events.

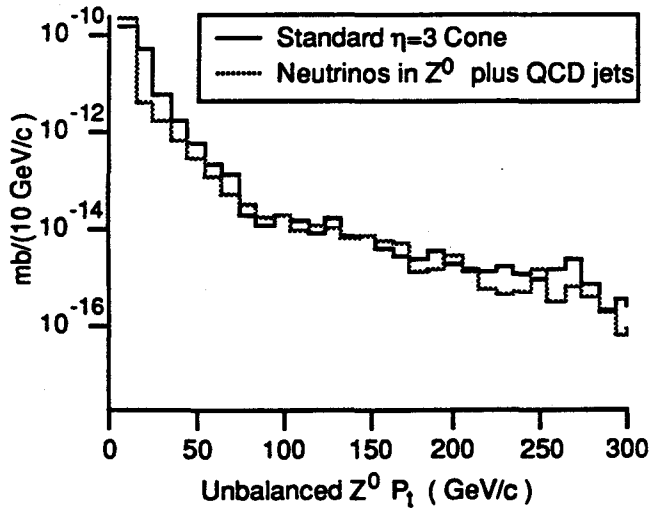

Figure 6-10 Missing E_T distributions for QCD Z + jets events for simulated detector (solid) and ideal detector (dashed).

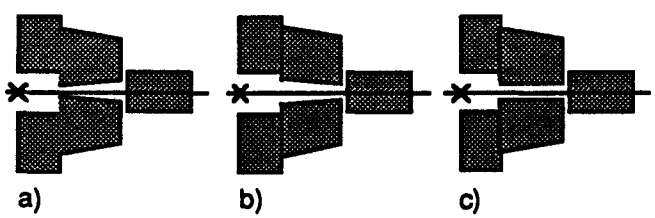

Figure 6-11 Alternative geometries for the end cap and forward calorimeter transition: (a) standard cone, (b) inverse cone, and (c) cylinder. Only half the detector is shown. (Not to Scale.)

ISAJET was used to simulate the signal from $H \rightarrow ZZ \rightarrow l^+l^- \nu\nu$ with Higgs masses of 400, 600, and 800 GeV, and background events were generated from two sources: QCD Z + jets, and continuum Z pair production with $ZZ \rightarrow l^+l^- \nu\nu$. Event selection was done by requiring two leptons within $\eta < 2.5$, reconstructed to the Z mass within 10 GeV. For events satisfying this requirement, the unbalanced p_T of the Z reconstructed from the lepton pair was plotted. For Higgs decays this shows a Jacobian peak up to $M_H/2$; for the background it is a smoothly falling distribution governed by the Z production kinematics. Figure 6-12 shows the signals are clearly visible above the background for the whole range of Higgs masses considered [5].

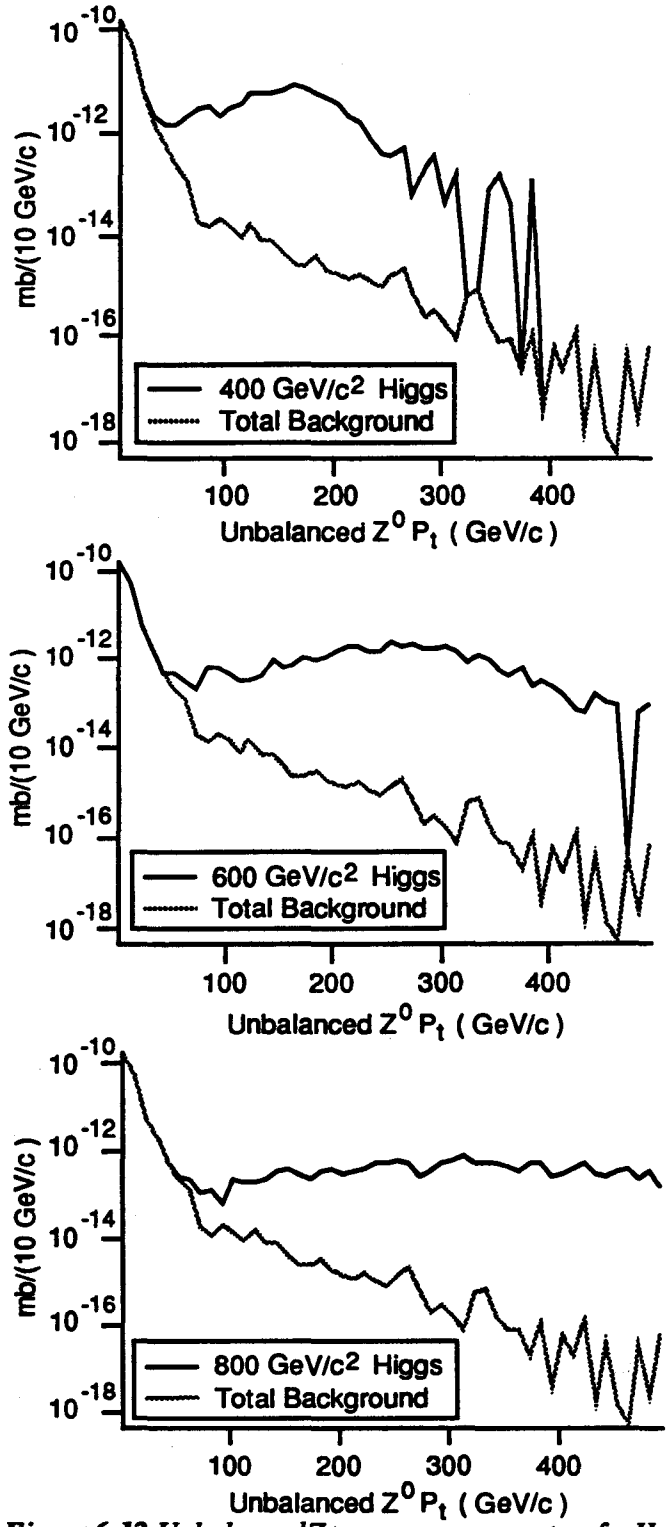

Figure 6-12 Unbalanced Z transverse momentum for $H \rightarrow ZZ \rightarrow l^+l^- \nu\nu$ (solid) and background of Z + jets $\rightarrow l^+l^-$ and continuum $ZZ \rightarrow l^+l^- \nu\nu$ (dashed) for Higgs mass of (a) 800, (b) 600, and (c) 400 GeV. The signal is clearly visible in all cases.

Therefore, the $H \to ZZ \to l^+l^- \nu\nu$ channels seem to offer a good way of extending our reach to higher Higgs masses than are accessible at standard luminosity with the four charged-lepton Higgs decays. At an integrated luminosity of 10^{40} cm^{-2}, there will be ~500 events above background for $M_H = 400$ GeV, ~200 for $M_H = 600$ GeV, and ~80 for $M_H = 800$ GeV.

6.3.1.7 $H \to ZZ \to l^+l^- jj$

Finally, $H \to ZZ \to l^+l^- q\bar{q}$ with one Z hadronic decay may be reconstructed, giving a potential factor of 24 more signal statistics than the four charged-lepton modes. This decay has been studied [18], and at high Higgs mass it can be reconstructed with reasonable efficiency. It provides an additional channel to study the heavy ($M_H \sim 800$ GeV) Higgs.

The detector was simulated as described earlier. Isolated leptons ($\Sigma E_T < 5$ GeV in $\Delta R = 0.2$) were assumed to have perfect angular measurement, while their momenta were treated by the resolution of the calorimeter or the muon system. Events were selected by requiring two isolated muons with

$$p_{T\mu\mu} > 200 \text{ GeV}, \quad |M_{\mu\mu} - M_Z| < 5 \text{ GeV}.$$

Jets were reconstructed by a simple cone algorithm with iteration of the cone axis. Jets with $p_T > 50$ GeV were found with a cone of $\Delta R = 0.2$ and a minimum cell $E_{Tmin} = 1$ GeV. One and only one pair of jets was required satisfying

$$p_{Tjj} > 250 \text{ GeV},$$
$$\Delta R_{jj} < 1.0,$$
$$|\phi_{jj} - \phi_{\mu\mu}| > 100 \text{ degrees}.$$

The mass of the pair was calculated by summing energy vectors within a cone of $\Delta R = 0.7$ around the axis defined by the vector sum of the two jets, and a cut was made at $|M_{jj} - M_Z| < 8$ GeV. Finally, the extra E_T in a larger cone of $\Delta R = 1.0$ was required to be less than 5%, to assure that the Z is isolated.

The production cross section of a standard $H \to l^+l^- q\bar{q}$ is 0.068 pb at $M_H = 800$ GeV. After the cuts, about 130 signal events are expected with 10^{40} cm^{-2} luminosity. Including the ee channel would give a total of 260 events assuming the same efficiency.

The dominant background is single Z production through the Drell-Yan process. The total cross section of $\mu\mu$ production at the Z mass with p_T greater than 200 GeV is about 13 pb. The accepted background events have a cross section of 0.04 pb in the muon channel alone, giving a signal-to-background ratio of 0.33. Because the Higgs has a large width at such a high mass, the signal does not exhibit itself as a bump, but as an excess of events within the mass window.

Part of the Higgs cross section is produced by WW fusion (Fig. 6-13), which leads to forward jets. Requiring at least one additional jet with $p_T > 50$ GeV and $\eta > 2.5$ improves the signal-to-background by a factor of 1.25, while retaining 36% of the signal. The $M_{\mu\mu jj}$ distribution after this cut is shown in Fig. 6-14.

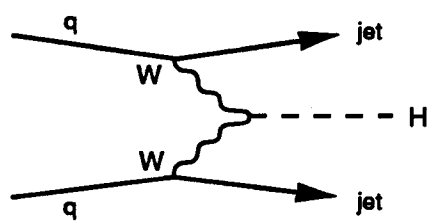

Figure 6-13 Feynman graph for WW → H, showing the forward quark jets.

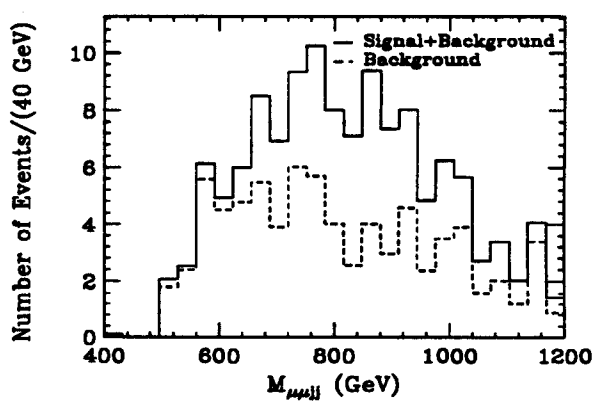

Figure 6-14 $M_{\mu\mu jj}$ distribution of signal plus background (solid) and the background only (dash).

It is a reconstructed Z from the jet-jet mass that really separates the signal from the background. Figure 6-15 shows the jet-jet mass distribution for

events with $600 < M_{ll\,jj} < 1000$ GeV without the $M_{jj} \approx M_Z$ cut. There is a statistically significant excess of events at M_Z. The signal-to-background ratio may perhaps be improved further by using the fact that Z's from the Higgs are longitudinally polarized and so have a $\sin^2\theta^*$ decay distribution, whereas the background is mainly transverse with a $(1 + \cos^2\theta^*)$ distribution.

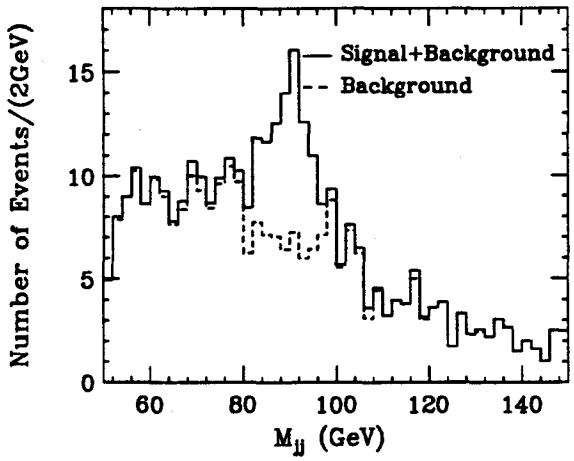

Figure 6-15 M_{jj} distribution of signal plus background (solid) and background only (dash).

6.3.1.8 Summary

The capability of the detector to discover the Higgs in various mass ranges using the decay channels described above is summarized in Fig. 6-16, covering the entire mass range $70 < M_H < 800$ GeV.

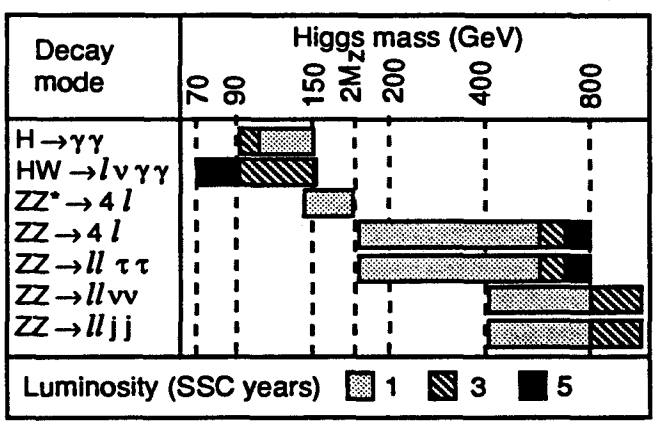

Figure 6-16 Approximate mass reach for Higgs discovery in various decay modes with the EMPACT/TEXAS detector.

6.3.2 Top Quark

Assume a top quark with a mass of 250 GeV. How is it discovered in the detector? How accurately could the mass be measured? Can its decay properties be determined? For example, if the top decays to a charged Higgs with a mass of 150 GeV, at what branching ratio level can this process be detected?

6.3.2.1 Top Events with Isolated eμ Signature

In this channel, top events should be identified from the decay chain:

$$t \to Wb, \quad W \to l\nu,$$
$$\bar{t} \to W\bar{b}, \quad W \to l\nu$$

with one e and one μ to eliminate the Drell-Yan background. The basic event selection criteria require one isolated electron and one isolated muon with $p_T > 30$ GeV and at least two jets with $p_{T1} > 50$ GeV, $p_{T2} > 30$ GeV. Then the background from W pair production and $Z \to \tau^+\tau^-$ decays is at the 1% level.

In this decay mode, the best way to measure the top mass is to reconstruct the lepton-jet mass [19]. Figure 6-17 shows the lepton-jet invariant mass for jets containing a nonisolated muon as a b tag. The solid line shows $M_t = 250$ GeV and the dashed line $M_t = 200$ GeV. After one SSC year, the top mass could be determined by fitting these invariant masses to a level fixed by systematic errors alone.

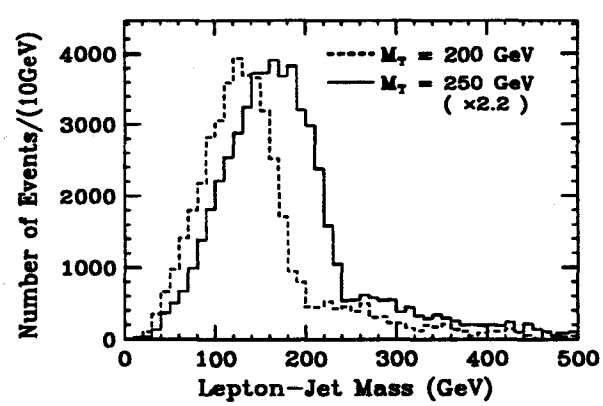

Figure 6-17 Lepton-jet invariant mass, where the jet has a nonisolated muon associated with it.

Because the distribution itself is wide, the effect of the resolution is minimal. Similar results have been obtained from the invariant mass distributions for the lepton-jet mass with the highest p_T jet, and from the lepton-lepton mass with one isolated and one nonisolated lepton.

6.3.2.2 Top Mass Reconstruction from Hadronic Decays

While the $e\mu$ decays are very clean, they do not allow direct reconstruction of the top mass. Direct reconstruction is possible for the decay chain:

$$t \rightarrow Wb, \quad W \rightarrow l\nu, \ (l = e, \mu)$$
$$\bar{t} \rightarrow W\bar{b}, \quad W \rightarrow q\bar{q}$$

The key is to find the two jets from the W. Requiring high p_T and looking for nearby jets reduces the combinatorial background [19]. Events were selected by requiring one isolated lepton with $p_T > 30$ GeV. Jets were found with a jet cone size $R = 0.3$; a minimum cell $E_{T,\,min} = 1$ GeV; and a minimum jet $p_{T,\,min} = 40$ GeV. A jet pair was selected if:

$$p_{Tjj} > 200 \text{ GeV}.$$
$$\Delta R_{jj} < 1.0$$
$$|\phi_{jj} - \phi_l| > 100 \text{ degrees};$$

The mass of the pair was calculated by summing energy vectors in a cone of $R = 0.7$ and with the axis defined by the vector sum of the two jets. The pair closest to M_W was selected. The extra E_T in a larger cone of $R = 1.0$ was required to be less than 5%, to assure that the W was relatively isolated. Jet pairs with mass within $|M_{jj} - M_W| < 15$ GeV were then used, with the jet closest to the reconstructed W being selected as the b-jet candidate. This tends to be true when the top has high p_T so that the W and b stay close. With no other selection on the b-jet, a peak at the top mass can already be seen at this stage.

To clean up the signal, the separation between the W and the closest jet was required to have $\Delta R < 2$. The p_T of the reconstructed top was required to be greater than 300 GeV. These additional cuts gave the mass distribution shown in Fig. 6-18. The broad background from misidentified W and b is reduced.

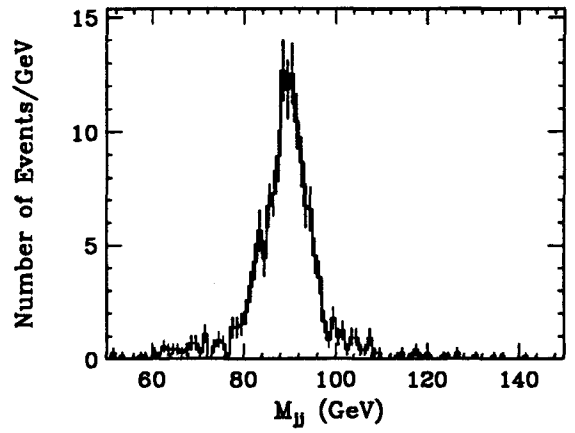

Figure 6-18 Mass of two close jets of events with only one pair of jets and with isolation cut.

The only background considered so far has been single W production in association with QCD radiation. The isolated muon comes from $W \rightarrow \mu\nu$ decay. The accepted events are also shown in Fig. 6-19. The background in the signal region is at the level of 3%.

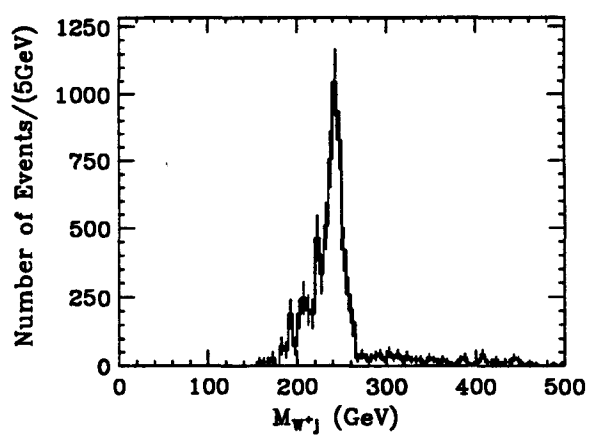

Figure 6-19 W-jet invariant mass after cuts. 250 GeV top (solid), W+ jets (dash).

Because the background does not seem to be overwhelming, the worsening of the calorimeter resolution by pileup noise and transverse shower development, which this simulation does not include, will probably not degrade measurement of the top mass in this decay mode.

6.3.2.3 Search for $t \to H^+b$ Decays

If there exists a charged Higgs lighter than the t, say $M_t = 250$ GeV and $M_{H^+} = 150$ GeV, then the decay $t \to H^+b$ can be significant. For $H^+ \to \tau^+\nu$, such decays can be observed by triggering on a conventional decay, $\bar{t} \to l^- \nu\bar{b}$, and measuring the relative rates for e, μ, and single-prong hadronic τ decays of the associated t. This test is limited by systematics. If the ratio can be determined to 10%, as seems reasonable, then sensitivity will be

$$B(t \to H^+ b)\, B(H^+ \to \tau^+ \nu) \approx 1\%$$

It is possible, although not theoretically favored, that the $H^+ \to c\bar{s}$ decay might be dominant. In this case, it is possible to trigger as before and reconstruct the $H^+ \to$ jet-jet decay in a manner similar to the $W \to$ jet-jet reconstruction. Figure 6-20 shows the resulting distribution for a 10% $t \to H^+b$ branching ratio with a 100% $H^+ \to c\bar{s}$ decay. Evidently this would be readily detectable; the sensitivity is estimated to be a product branching ratio of a few percent.

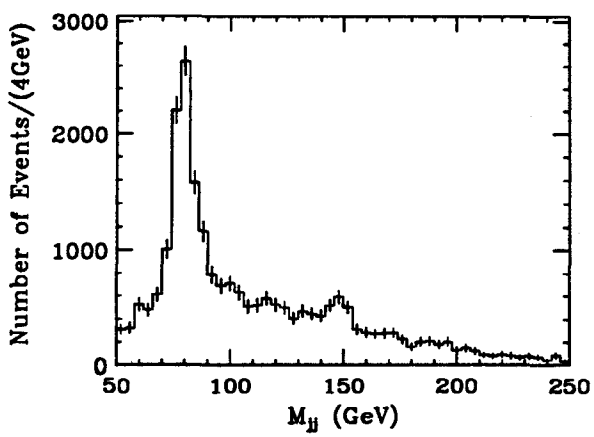

Figure 6-20 Jet-jet mass for $t \to H^+b$, $H^+ \to c\bar{s}$.

6.3.3 Jet Energy Resolution

Demonstrate the jet energy resolution as a measure of the calorimetry performance of the proposed detector by studying the decays:

$$Z^0 \to jet + jet$$
$$Z' \to jet + jet,\ M_{Z'} = 1\ TeV$$

If a fixed-cone algorithm with a radius ΔR is used to find the jets, then the cones will generally be separate if the momentum of the Z^0 or Z' is somewhat below $M/\tan(\Delta R)$ but will overlap at higher momenta. In the intermediate regime, the decay can be considered as one jet or two. The Z mass resolution and shift will be affected by fragmentation and shower fluctuations. Also, for a fraction of Z decays, a hard gluon radiated by one of the quarks may appear as a well-defined third jet or miss the cone cut. While the former can be recognized, the latter leads to lost energy.

ISAJET was used to produce a sample of 5000 Z^0's with a mass of exactly 91 GeV and 5000 Z' with a mass of 1000 ± 1 GeV [20]. For each event, the particles from the Z^0 or Z' were boosted to the rest frame and then reboosted to the desired momentum. The remaining particles in the event, and any neutrinos, were ignored. Undecayed particles were converted to hadronic energy and muons were assumed to give 3 GeV of hadronic energy. Each momentum vector was re-aimed to the center of the correct calorimeter tower.

GEANT with full shower simulation was used to calculate the difference between the particle and the shower centroid. Typical distributions from this investigation are shown in Fig. 6-21. These were used to determine a transverse offset to be applied to each track.

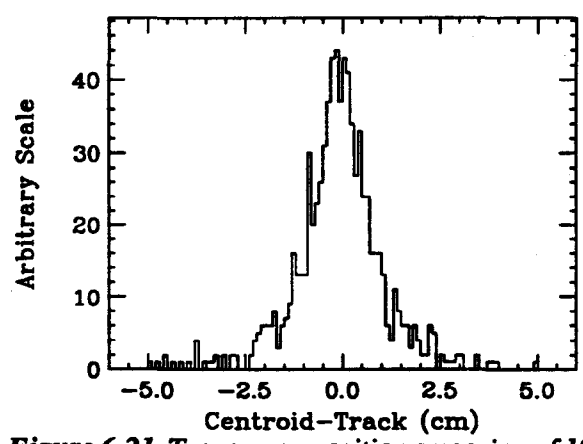

Figure 6-21 Transverse position smearing of 10 GeV pions in EMPACT/TEXAS lead-LAr calorimeter from GEANT.

Energy smearing was done using the appropriate calorimeter resolutions for SPACAL, for LAr, and for the LAr CAD model augmented by the energy crossover in the $\eta = 3$ region from GEANT [5].

Figure 6-22 shows the SPACAL and LAr CAD mass distributions for the Z^0 at rest obtained by summing all hit cells.

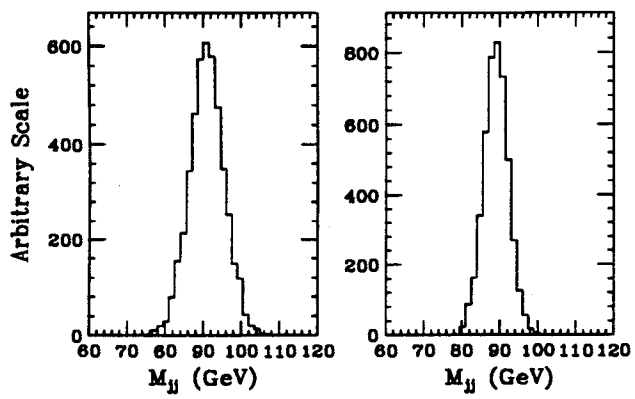

Figure 6-22 $Z^0 \rightarrow jj$ resolutions summing all hit cells. (a) SPACAL. (b) LAr CAD model.

A fixed-cone jet algorithm with $\Delta R = 0.7$ was then applied. No jet splitting or variation of ΔR were attempted. Figure 6-23 shows the resulting mass distribution. A cone of $\Delta R = 0.9$ reduces the tails by more than a factor of two, but this large cone would probably include too much energy from the underlying event and from pileup. Figure 6-24 shows the corresponding plots for a 1 TeV Z'.

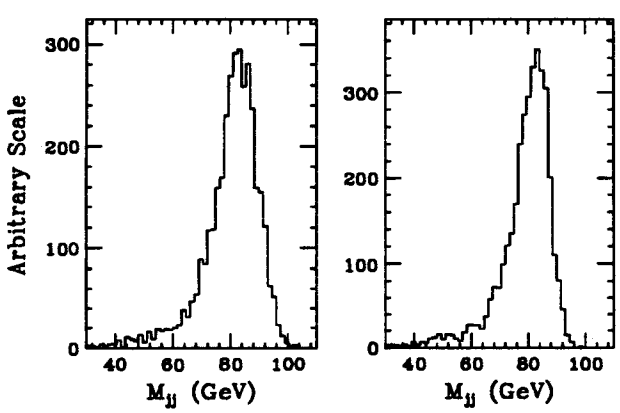

Figure 6-23 $Z^0 \rightarrow jj$ resolutions for $\Delta R = 0.7$ cone clustering. (a) SPACAL. (b) LAr CAD model.

Z^0 and Z' mass resolutions were calculated from the simulations. When the mass curve was asymmetric, the resolution was determined from FWHM/2.36; otherwise the data in the peak were fit to a Gaussian. The results are summarized in Table 6-4.

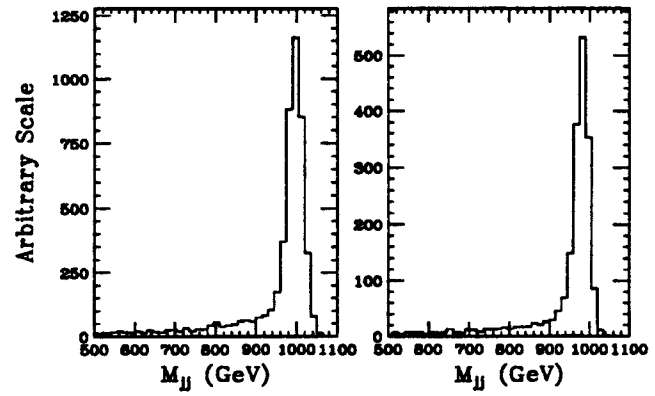

Figure 6-24 $Z' \rightarrow jj$ resolutions for $\Delta R = 0.7$ cone clustering. (a) SPACAL. (b) LAr CAD model.

Table 6-4 $Z^0, Z' \rightarrow$ jet + jet masses and resolutions.

P (GeV)	Perfect Calorim	SPACAL Param	LAr Param	LAr CAD
$Z^0 \rightarrow jj$, no clustering				
0	91.0	91.0 ±4.5	91.0 ±4.5	88.5 ±3.0
50	91.0	90.8 ±4.4	90.8 ±4.4	89.5 ±3.0
100	91.0	90.8 ±3.8	90.8 ±3.8	89.0 ±3.0
200	91.0	91.0 ±3.4	91.0 ±3.4	88.8 ±2.3
500	91.0	92.0 ±3.0	92.0 ±3.0	89.0 ±2.5
$Z^0 \rightarrow jj$, $\Delta R = 0.7$ cone				
0	83.0 ±4.2	82.0 ±6.8	82.0 ±5.9	81.0 ±5.9
50	84.5 ±3.8	83.3 ±6.1	83.3 ±6.1	82.0 ±5.1
100	86.3 ±3.2	86.0 ±5.1	86.0 ±5.1	84.8 ±4.4
200	91.0 ±1.4	91.7 ±3.5	91.7 ±3.5	89.0 ±3.4
500	90.0 ±1.0	90.3 ±3.6	90.3 ±3.6	89.2 ±2.5
$Z' \rightarrow jj$, no clustering				
0	1000	990 ±19	990 ±19	980 ±16
1000	1000	990 ±22	990 ±19	980 ±15
$Z' \rightarrow jj$, $\Delta R = 0.7$ cone				
0	990 ±13	990 ±19	990 ±19	980 ±19
1000	990 ±15	990 ±22	990 ±22	980 ±18

The η-ϕ segmentation of $.07 \times .07$ has negligible effect on the masses or widths; the same is true for the transverse shower smearing, even with a lead calorimeter at a radius of 1 meter. Both effects primarily smear the hadron direction but not the energy, and the particles with the largest smearing tend to be those of lowest energy. Calorimeter energy resolution directly affects the mass resolution. The parameterized LAr and SPACAL distributions are indistinguishable. The CAD parameterization gives a slightly narrower width at all Z^0 and Z' momenta because it assumes a slightly better intrinsic resolution. It also shows a mass shift because it includes losses resulting from material and punchthrough. The mass resolution is degraded by the fixed-cone jet algorithm, especially for low momentum Z^0's. Carefully tuning of the jet algorithm will be essential for a real analysis.

6.3.4 Lepton Detection

Demonstrate the acceptance and resolution (not the ability to run at extremely high luminosities) of the lepton detector by a study of a Z' with a mass of 4 TeV. Show a measurement of mass and asymmetry for 1000 produced $Z' \to e^+e^-$, $\mu^+\mu^-$, $\tau^+\tau^-$ each.

A new neutral gauge boson Z' of mass 4 TeV has been simulated [21] using PYTHIA. Appropriate couplings of the Z' to fermions have been added for various Z' models. Note that, depending on the Z' model, the assumed 1000 $Z' \to \mu\mu$ events would require 5 to 10 years at 10^{40} cm^{-2} per year. This search would obviously benefit from a luminosity well above the standard 10^{33} $cm^{-2}\ s^{-1}$.

6.3.4.1 $Z' \to \mu\mu$

The geometrical acceptance for $Z' \to \mu^+\mu^-$ decays is 88% for the rapidity coverage $\eta < 2.5$.

There is essentially no real background to this process. Drell-Yan production of dileptons through a virtual photon or Z^0 is about five orders of magnitude below the peak.

Figure 6-25 shows the dimuon mass distribution with a vertex-constrained muon momentum fit.

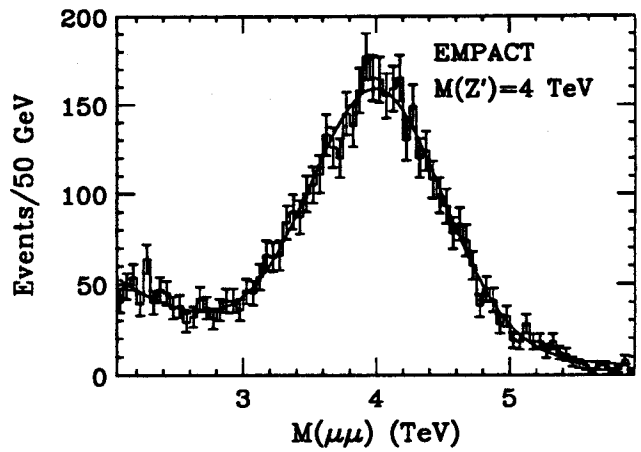

Figure 6-25 Mass spectrum for 1000 $Z' \to \mu\mu$ events for a 4 TeV Z' mass.

Because the resolution exceeds the natural width of the Z', the data have been fit with a Gaussian on a smooth continuum, giving $\sigma = 383$ GeV, or 9.6% of $M_{Z'}$. Multiple scattering, muon detector resolution, and detector misalignments have been included. The average momentum resolution of all the muons for the entire detector is 14%. Without using the vertex constraint, $M_{Z'}$ has $\sigma = 495$ GeV.

For these high-energy muons, energy loss in the calorimeter must be considered. This has been simulated using GEANT. Although typical muon energy losses are O(50 GeV), there are occasional large energy losses from hard interactions. Because the muons are isolated, the measured energy in the calorimeter can be recombined with the muon momentum measurement. But some energy is lost because it is deposited in inactive elements. For less than 1% of the events, a muon will lose over 20% of its energy in inactive elements, exceeding the average muon momentum measurement error (14%). Such events have been excluded. For the remaining events, the effect of energy loss is small compared to the momentum resolution. The overall efficiency in the muon channel is about 87%.

Tracking inefficiency (about 6%) resulting from muon radiation is discussed in Sect. 3.4.2 and is not included here. For 1000 total $Z' \to \mu\mu$ events, the error on $M_{Z'}$ would be about $\Delta M = 383\ \text{GeV} / \sqrt{870} = 13$ GeV, or 0.3%.

For this experiment the forward-backward asymmetry is measured using muons. For pp

collisions, it is an odd function of the Z′ rapidity. While it would be possible to fit to the expected distributions, little sensitivity is lost by folding the distribution and then integrating over rapidity. Therefore the asymmetry A_{FB} is defined as follows: let $y_\pm$ be the rapidities of the final state muons, $\mu^\pm$. Then if $y_+ + y_- > 0$

$$A_{FB} = A_{FB}^{+} = \frac{\sigma(y_- > y_+) - \sigma(y_- < y_+)}{\sigma(y_- > y_+) + \sigma(y_- < y_+)}$$

while for $y_+ + y_- < 0$, $A_{FB} = -A_{FB}^{+}$. Table 6-5 summarizes A_{FB} for various models and gives the statistical error, ΔA_{FB}, expected for 1000 $\mu\mu$ events. All muons in our 1000-event sample were measured with the correct charge.

Table 6-5 A_{FB} and width for Z′ in various models.

Model	$A_{FB} \pm \Delta A_{FB}$	$\Gamma \pm \Delta\Gamma$ (GeV)
E6, $\theta = 90°$	-0.14 ± 0.03	48 ± 1.3
E6, $\theta = 128°$	-0.31 ± 0.04	38 ± 1.1
L-R symmetric	0.10 ± 0.03	88 ± 2.4
Alt. L-R symm.	-0.22 ± 0.04	60 ± 1.8

6.3.4.2 $Z' \rightarrow e^+e^-$

Because of the superior energy resolution for electrons, the Z′ mass and width are best measured in the e^+e^- channel. At such high energies, only the 0.5% constant term in the energy resolution matters. Figure 6-26 shows the expected M_{ee} distribution for 1000 events. There is essentially no difference between this distribution and the generated one. We have fit to a Breit-Wigner resonance function plus a smooth continuum. The error on the mass is $\Delta M_{Z'} = 2.8$ GeV or 0.07%. The value of $\Gamma_{Z'}$ is model dependent and is given in Table 6-5 along with the measurement error for the 1000 $Z' \rightarrow ee$ sample.

At high luminosity not only the mass and width but also the couplings of a 4 TeV Z′ could be measured. The cross section and asymmetry will, in general, be different in the off-peak region than in the resonance region. Because of its excellent mass resolution for electron and muon channels, the detector is well-suited for these studies.

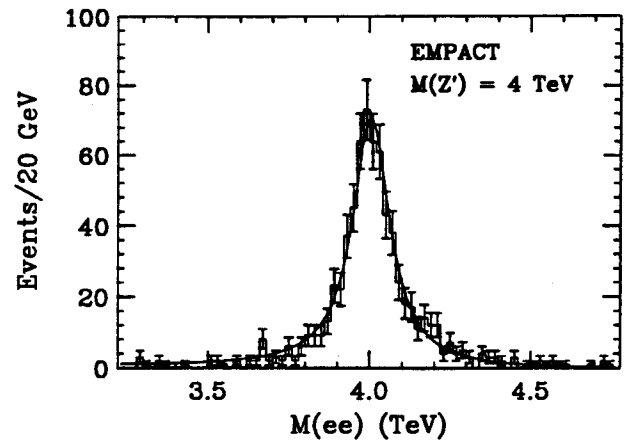

Figure 6-26 Mass spectrum for 1000 $Z' \rightarrow ee$ events for a 4 TeV Z′.

6.3.4.3 $Z' \rightarrow \tau^+\tau^-$ mode

For $Z' \rightarrow \tau\tau$ there are at least two neutrinos. Because the ν's will be almost back-to-back, their momenta cannot be determined from the missing p_T. For τ decays into three prongs, the ν_τ momentum is softer, and it is possible to see a peak in the visible p_T. The three-prong jets will be detected using the TRD tracker. A one-prong jet will be required on the other side to eliminate any QCD background.

ISAJET was used to generate 1000 $Z' \rightarrow \tau\tau$ events with $M_{Z'} = 4$ TeV, and the TRD response was simulated. For the three-prong decays, the three tracks are typically inside a single row of straws, but the multiplicity can be determined from the pulse height distribution, as indicated in Table 6-6. The three-prong jet is called an isolated "heavily ionizing" or "twice minimum ionizing" track in the TRD; the one-prong recoil is called an isolated "electron," which may be a real e or a high-p_T π or μ. From 1000 ττ decays a signal of 244 events is obtained with one three-prong and one one-prong decay, and 156 of these pass the TRD cuts. Figure 6-27 shows that the reconstructed three-prong jet E_T is degraded from that of the τ because of the missing neutrino energy; but there is a clear signal around $p_T \sim 1$ TeV.

The background to this distribution would be from Drell-Yan ττ events, which have a very small cross section compared to the Z′, and from QCD jets in the range $p_T \sim 1$ TeV. One of the jets would

have to fragment into a very-high-momentum single charged pion, while the other would have to appear like a three-prong τ decay. This gives a negligible background.

Assuming that the TRD performance is well understood, lepton universality in the ratio $B(Z' \rightarrow \tau\tau)/B(Z' \rightarrow \mu\mu)$ will be tested with a precision determined by the $\tau\tau$ statistics, i.e., $\pm$ 8% from 1000 Z′ decays into each mode.

Table 6-6 Detection of $Z' \rightarrow \tau\tau$ using the TRD tracker.

Found As	$\tau \rightarrow$ 3 Charged	$\tau \rightarrow$ 1 Charged
Heavily Ionizing	40%	2%
"Electrons"	20%	80%
2 × min. Ionizing	40%	13%
Min. Ionizing	0%	5%

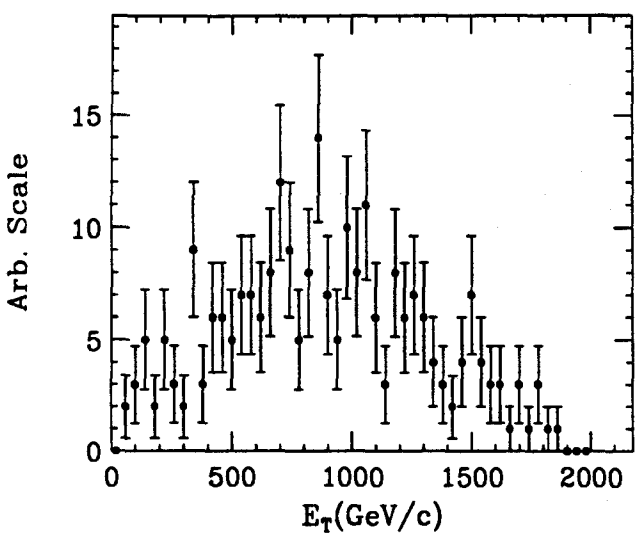

Figure 6-27 Reconstructed E_T distribution for three charged particle τ jets found in the TRD tracker.

6.4. ADDITIONAL PHYSICS STUDIES

In addition to the questions posed by the PAC, other studies have been performed that illuminate particular physics strengths of the detector. The good hermeticity of the calorimeter enables missing-p_T signals of supersymmetric particles to be seen, and the excellent hadron calorimetry enables jet energy measurements at high p_T and a search for quark substructure to be made.

6.4.1 Supersymmetry

Supersymmetric (SUSY) particles are produced in pairs: $\tilde{g}\tilde{g}$, $\tilde{g}\tilde{q}$, $\tilde{q}\tilde{q}$, $\tilde{q}\tilde{\gamma}$, or $\tilde{g}\tilde{\gamma}$. This analysis [22] concentrates on the $\tilde{g}\tilde{g}$ channel in the minimal SUSY model [23], partly because it has the largest cross section, and partly because its signatures are most affected by the existence of cascade decays among the four neutral color-singlet superparticles $\tilde{\chi}^0_i$, i = 1–4, and two charged ones $\tilde{\chi}^{\pm}_i$, i = 1–2. These cascade decays give complicated events with missing p_T, jets, leptons, W and Z bosons, and even light Higgs bosons [24].

6.4.1.1 Large Missing E_T Signature

Gluino masses of 220, 300, 750, and 1500 GeV were considered, each with one or two choices for the other parameters in the minimal SUSY model. Some of these cases were studied previously [25], while others are consistent with recent CDF and LEP limits [26].

About 25% of the $\tilde{g}\tilde{g}$ events have at least one gluino that decays directly to $\tilde{\chi}^0_1$, giving large missing p_T. The major backgrounds are from heavy quarks (top in particular) and from gauge boson at high p_T. Samples of about 3500 events for each of the masses were generated using ISAJET, including all decays. The events were analyzed in a simple calorimeter simulation with the CAD model resolution, and jets were found using a cone algorithm with $\Delta R = 0.7$. Samples of 4000 Z^0 decaying to neutrinos and 15 000 QCD events containing either a lepton with $p_{Tl} > 50$ GeV or a neutrino with $p_{T\nu} > 100$ GeV were generated and analyzed in the same way.

The minimal set of cuts requires at least four jets with $p_T > 50$ GeV and a transverse sphericity S greater than 0.2. Stronger cuts can be applied requiring large p_T jets and large E_T^{miss}, but these discriminate against lower mass gluinos.

Figure 6-28 shows the missing transverse energy, E_T^{miss}, and the p_T^{out} distributions for the 750 GeV gluino with the cuts described. p_T^{out} is defined to be the momentum out of the plane formed by the transverse sphericity direction and the beam direction. The solid curve shows the gluino

distribution. The dashed curve shows the same distribution from QCD-produced heavy quark background events. The QCD background at low E_T^{miss} or p_T^{out} is underestimated because at least 100 GeV of neutrino energy was required during the generation. The dot-dashed curve shows the distribution for the backgrounds from $Z \rightarrow \nu\nu$ events.

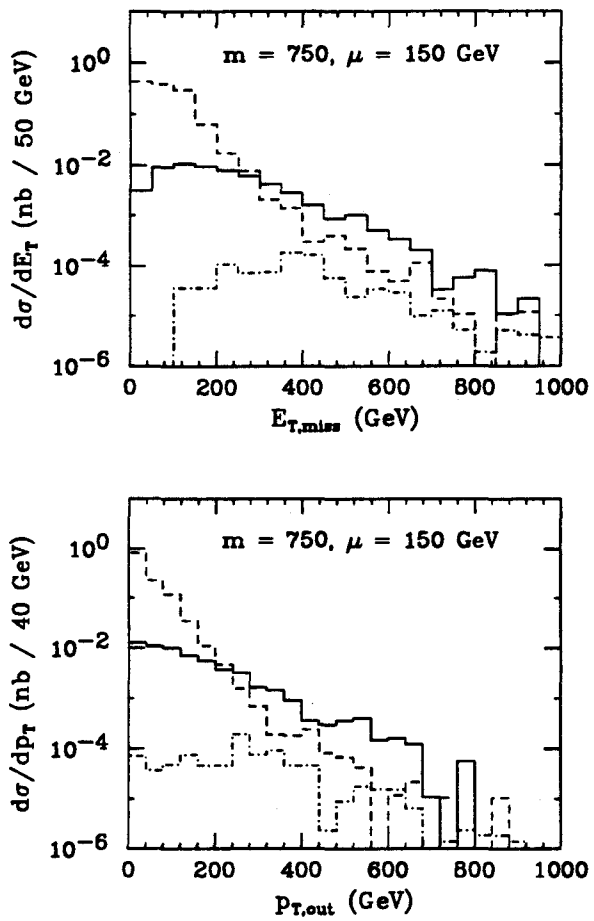

Figure 6-28 E_T^{miss} and p_T^{out} distributions for $M_{\tilde{g}}$ = 750 GeV.

The signal-to-background ratios were found [22] to be 5:1 for the 220 GeV gluino with E_T^{miss} > 200 GeV; 3.5:1 for the 300 GeV gluino with E_T^{miss} > 100 GeV; and 4:1 for the 750 GeV gluino with E_T^{miss} > 300 GeV. For the 1500 GeV gluino it was difficult to establish a signal-to-background ratio because not enough background events were generated at very large p_T, but the signal would be at E_T^{miss} > 1 TeV.

If a large E_T^{miss} signal were present in the data, the four-jet and two-jet masses could be used to determine the gluino mass. In Fig. 6-29 the transverse mass M_T calculated from the four largest E_T jets plus the missing p_T is shown for the 300 GeV and 750 GeV gluinos, using only events with E_T^{miss} exceeding the cut values stated above. These distributions are clearly sensitive to the gluino mass. At present, the background statistics for the higher mass cases are quite poor, but it is not likely that they will significantly alter the shape of the signal distributions.

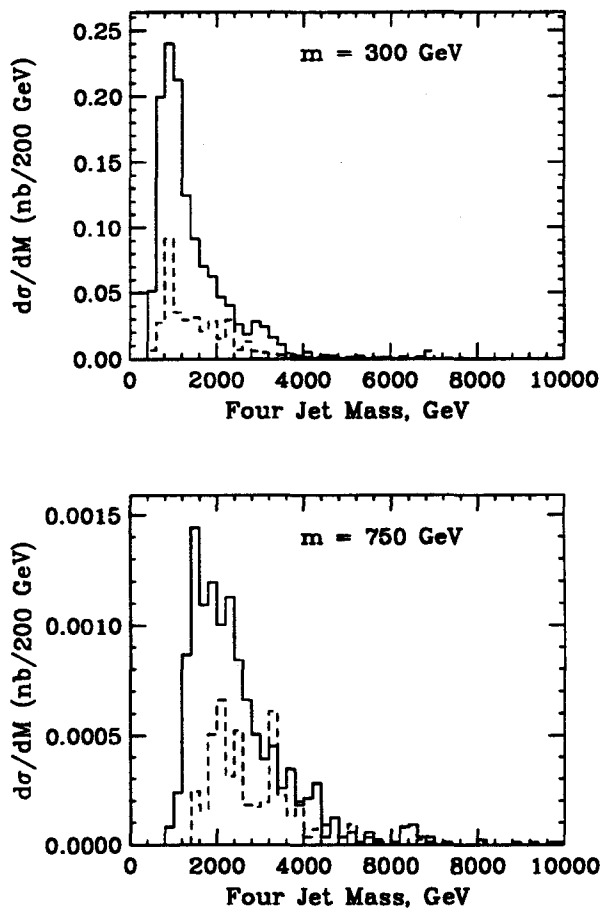

Figure 6-29 Effective mass of 4 highest p_T jets and the missing p_T. The dashed curve is the background.

The two-jet mass formed from the jet with the largest E_T and the closest of the next three largest E_T jets in ΔR can also be used to determine the gluino mass. These two jets are likely to belong to

the same gluino, and the peaks of the distributions shift in proportion to the gluino mass [22].

6.4.1.2 Dilepton Signatures for Gluinos

The primary signature for gluino production is large missing E_T. Additional signatures are the presence of same-sign dileptons or Z^0 decays in the events with large missing E_T. The same-sign dilepton signature, which arises from the Majorana nature of gluinos, is particularly interesting.

The gluino event samples were generated [22] using ISAJET, and events having at least two leptons with $p_T > 20$ GeV were selected. The number of events per year are indicated in Table 6-7 with various cuts. Electrons and muons have been summed to improve the Monte Carlo statistics. Most of the leptons have $\eta < 2.5$. The $p_T > 20$ GeV cut is severe for 220 GeV gluinos. If it were reduced to 5 GeV, the rate would increase by almost an order of magnitude.

Table 6-7 Gluino events per year for dilepton selections and η cuts

Selection	For Gluino Mass			
	220	750	1500	3000
all	3.8×10^6	1.8×10^5	5600	69.3
all ($\eta < 2.5$)	3.0×10^6	1.7×10^5	5400	68.4
all like sign ($\eta < 2.5$)	1.2×10^6	6.8×10^4	2200	27.9

It is expected that the leptons from the gluino decays will be isolated, with $E_T < 5$ GeV in a cone $\Delta R = 0.1$ surrounding the lepton. Only isolated leptons are used because this significantly reduces the heavy quark background.

Various effective mass distributions have been suggested to determine the mass of the gluino [25]. One of these, M_{tot}, is the effective mass of the two highest p_T leptons, the four highest p_T jets, and the missing p_T. This "$\tilde{g}\tilde{g}$ system mass" is shown in Fig. 6-30 for gluino masses of 220 GeV, 750 GeV, and 1500 GeV respectively. Clearly this distribution is sensitive to the gluino mass, peaking at roughly twice the gluino mass.

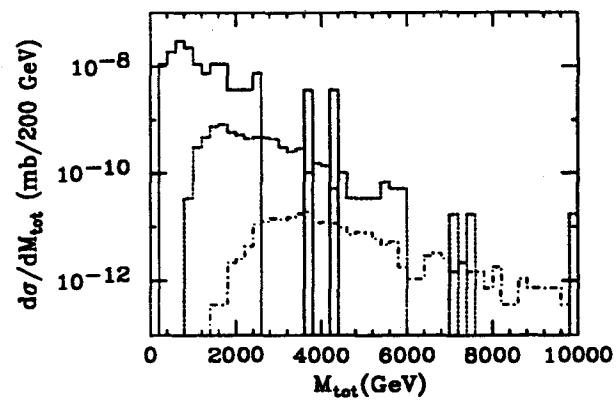

Figure 6-30 Effective mass of 2 highest p_T leptons, 4 highest p_T jets, and the missing p_T for gluino events for M = 200 GeV (solid), M = 750 GeV (dashed), and M=1500 GeV (dot-dashed).

6.4.2 Limits on Quark Compositeness

The composite nature of quarks would show up as a deviation from the standard QCD cross section for jets at high p_T. The systematic errors in jet energy measurements include uncertainties in the underlying event and in leakage outside the cone. There are also uncertainties in the parton distributions, but it is expected that additional knowledge will be gained from HERA and from the SSC itself.

Figure 6-31 shows the signals for compositeness scales $\Lambda = 5$, 10, and 20 TeV and the QCD cross section with MRS Set B [27] parton distributions. The effect of choosing the EHLQ Set 1 structure function is shown. This is an extreme example of current uncertainty, because EHLQ 1 is no longer favored, but it does set a scale for the experimental effects described below.

A previous study [28] concluded that the calorimeter should have $|e/h - 1| < 0.1$. However, it assumed that the calorimeter would be calibrated at 10 GeV, which is inappropriate for SSC jets in the multi-TeV range. For the present study [29], the GFLASH [30] simulation was used to calculate the π^0 content of hadronic showers on an event-by-event basis. The response to hadrons was then simulated as the sum of a purely hadronic component, E_{had}, and a purely electromagnetic component, E_{em}.

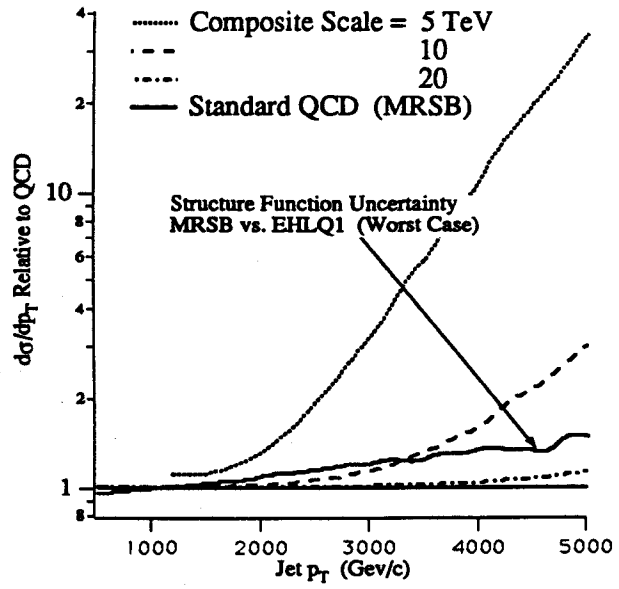

Figure 6-31 Compositeness signals for Λ = 5, 10, and 20 TeV and the QCD expectation. The effect of parton distributions is shown for MRS Set B vs EHLQ Set 1.

Figure 6-32 shows the average response to hadrons as a function of incident energy for two different calorimeter intrinsic e/h values. The response has been calibrated at 100 GeV. These curves are consistent with the analytic estimates of Groom [31]. An intrinsic e/h = 1.00 (not shown) gives a constant average response equal to unity, but would have a finite resolution.

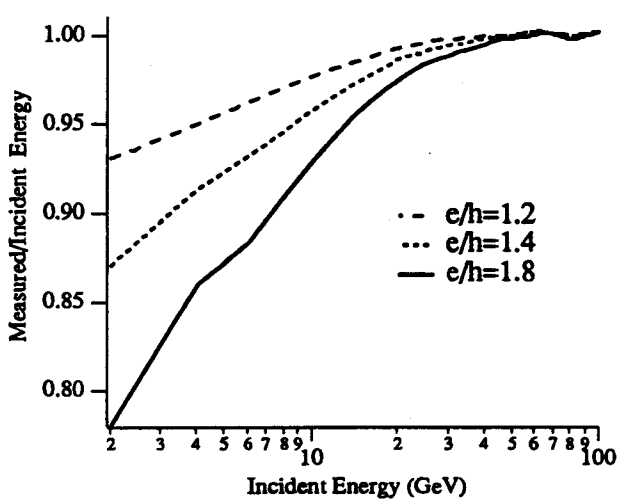

Figure 6-32 Average calorimeter response as a function of incident hadron energy for various values of e/h.

ISAJET was used to generate QCD jet events. Jets were found using a cone algorithm with ΔR = 0.7.

The resulting jet cross section is shown in Fig. 6-33(a) for different values of intrinsic e/h and two different calibration points. Fig. 6-33(b) shows the same cross sections relative to the QCD expectations with e/h = 1.00. The largest deviations from QCD are for the low-energy calibration point (10 GeV). Fig. 6-32 indicates that low-energy calibration shifts the response to all higher incident energies upward.

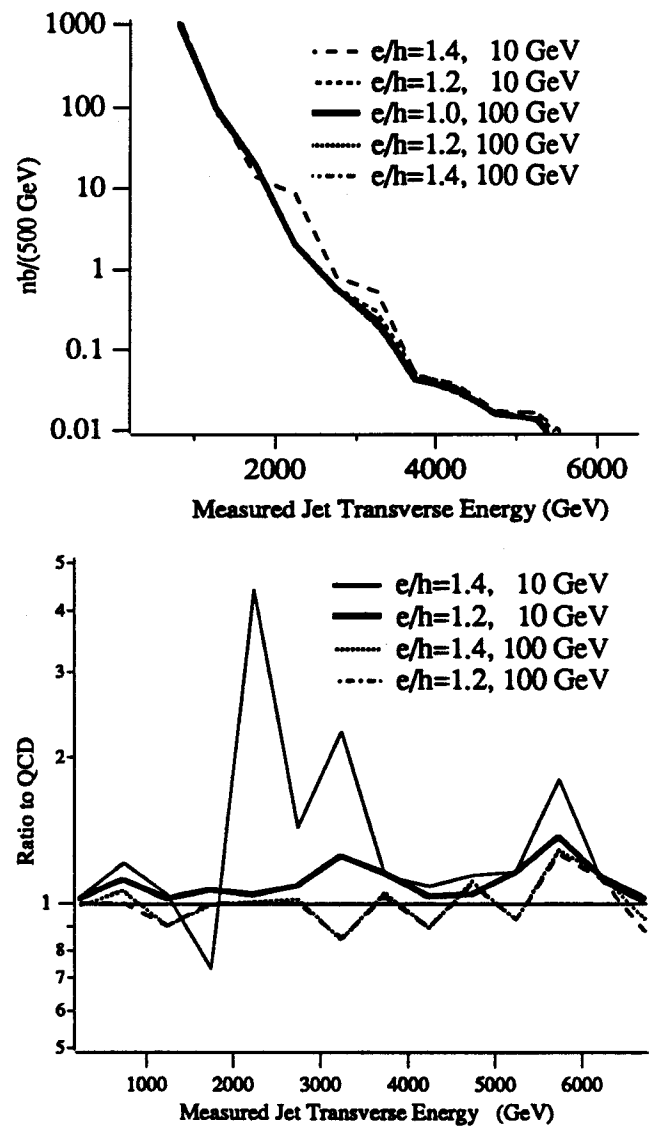

Figure 6-33 (a) Jet cross section for various values of e/h and calibration points (see text.) (b) Same cross sections normalized to QCD with e/h = 1.00.

In conclusion, the calorimeter e/h does not seem very important for compositeness searches, provided the calibration is made at high energy. Either the LAr or SPACAL design proposed should be capable of determining compositeness limits up to scales $\Lambda \sim 15$ TeV and beyond if systematic effects are understood.

REFERENCES

1. F. E. Paige and S. D. Protopopescu, "ISAJET: A Monte Carlo Event Generator for pp and $p\bar{p}$ Reactions," in Proc. 1986 Summer Study on Physics at the Superconducting Supercollider (Snowmass, CO, 1986), p. 320.
2. H. -U. Bengtsson and T. Sjostrand, Comput. Phys. Commun. **46**, 43 (1987).
3. S. L. Linn, Nucl. Instrum. & Methods **A288**, 598 (1989).
4. T. S. Adams *et al.*, "Status Report of an Engineering Design Study of Hermetic Liquid Argon Calorimetry for the SSC," Proc. of the Workshop on Calorimetry for the Supercollider, (World Scientific, Tuscaloosa, AL, 1989) p. 243; W. J. Womersley, Nucl. Instrum. & Methods **A289**, 475 (1990).
5. G. Forden, "A Preliminary Study of the p_T Response of the EMPACT $\eta = 3.0$ Cone," EMPACT/TEXAS Note 236.
6. W. L. Dunn *et al.*, "Development of a Robust CAD-to-GEANT Interface for Physics Detector Design," DOE SBIR-10386-90-I, January 1990.
7. F. Carminati, Presentation at ECFA LHC Workshop, Aachen, October 1990.
8. For recent discussions, see J. F. Gunion and G. L. Kane, contribution to Snowmass '90 proceedings.
9. See, for example, C. Barter *et al.*, "Detection of $H \to \gamma\gamma$ at the SSC," in Proceedings of the Summer Study on High-Energy Physics in the 1990s, edited by S. Jensen, World Scientific (1988) p. 98.
10. H. Newman, in Proceedings of the Fort Worth Symposium on SSC Detector R&D, October 1990, (to be published).
11. H. Iso, private communication.
12. T. Kamon, "Search for Intermediate Mass Higgs," EMPACT/TEXAS Note 340.
13. R. Kleiss, Z. Kunszt, and W. J. Stirling, preprint DTP/90/54 (1990).
14. K. Furuno, EMPACT/TEXAS Note 350.
15. M. Chen, E. Nagy. and G. Herten, "High Pt Weak Bosons as Signatures for Higgs-Like Heavy Particles," Proceedings of the Workshop on Experiments, Detectors, and Experimental Areas for the Supercollider; R. Donaldson and M. G. D. Gilchriese, Berkeley, (1987); F. E. Paige, and R. Thun, "$t\bar{t}$ Backgrounds for $H \to \mu^+\mu^-\mu^+\mu^-$ at the SSC," SSCL preprint (1990); S. R. Gottesman, "A Study of $H \to Z^0Z^0 \to 4\mu$ for EMPACT," EMPACT Note 229 (1990); S. R. Gottesman and J. Shank, "Monte Carlo Study of Search for a Standard Model Higgs with the EMPACT Detector," EMPACT/TEXAS Note 235.
16. G. Yost, "$H \to ZZ \to 4\mu$," EMPACT/TEXAS Note 343.
17. F. E. Paige and E. Wang, Proc. Workshop on Calorimetry for the SSC, (Tuscaloosa, 1989) p. 99.
18. H. Ma, "Higgs $\to ll$ qq Decay at the SSC," EMPACT/TEXAS Note 346.
19. H. Ma, "Top at the SSC," EMPACT/TEXAS Note 347.
20. M. Shupe, "Mass Resolution of the EMPACT/TEXAS Detector for Z^0 and Z' in the Mode Jet-Jet," EMPACT/TEXAS Note 348.
21. R. Frey, "$Z' \to l^+l^-$ in the EMPACT/TEXAS Detector," EMPACT/TEXAS Note 349.
22. V. Fonseca *et al.*, "SUSY Searches at the SSC," EMPACT/TEXAS Note 228.
23. H. Haber & G. Kane, "The Search for Supersymmetry: Probing Physics Beyond the Standard Model," Physics Reports 117, p. 75 (1985).
24. R.M. Barnett *et al.*, "Experiments, Detectors, and Experimental Areas for the Supercollider," (Berkeley, 1987), p. 187; H. Baer *et al.*, ibid., p. 210.
25. M. Barnett *et al.*, "High Energy Physics in the 1990s," Snowmass, 1988, p. 226.
26. CDF and ALEPH results preliminarily announced at Snowmass 1990.
27. A. D. Martin, R. G. Roberts, and W. J. Stirling, Phys. Rev. **D42**, 798 (1990).
28. V. Barnes, *et al.*, in Proceedings of the Workshop on Experiments, Detectors, and Experimental Areas for the Supercollider," R. Donaldson, M. G. D. Gilchriese, Eds. (World Scientific, Berkeley, CA, 1987), p. 235.

29. G. Forden, "e/h Study for EMPACT/TEXAS," Note 352 (1990).
30. G. Grindhammer, M. Rudowicz, S. Peters, Workshop on Calorimetry for the Supercollider, R. Donaldson, M. G. D. Gilchriese, Eds. (World Scientific, Tuscaloosa, Alabama, 1989), p. 151.
31. See for example D. Groom, "Jet Response of a Homogeneous Calorimeter," SDC Note 90-00078.

7.0 COST, SCHEDULE, AND MANAGEMENT

7.1 INTRODUCTION

The EMPACT/TEXAS collaboration has worked closely with the Physics Research Division of the SSCL to arrive at a clear, consistent approach to determine the cost of the detector system described in this LoI. The collaboration has adhered to the cost-estimating guidelines provided by the SSCL, and thus presents costs segregated into the distinct categories of detector, EDI/QA, services and equipment, facilities, computing, contingency, and escalation.

We have performed bottoms-up estimations of nominal costs based on a detailed work-breakdown structure (WBS) consistent with the overall SSC project WBS, and have used SSCL- provided labor rates in our nominal cost estimations. We have also made conservative determinations of contingencies based on quantitative estimations of the risks caused by technical, cost, and schedule considerations for each WBS element that, taken together with the nominal costs, provides a reliable upper limit on the cost of the detector system. The nominal costs—with contingencies—are then escalated according to SSCL guidelines and presented along with an experiment design, fabrication, installation, and commissioning schedule consistent with the overall SSC project schedule. We conclude with a discussion of the management structure and institutional responsibilities for the period that encompasses preparation of the proposal and beyond.

7.2 EoI BASELINE METHODS

As detailed in Sect. 8 of the EEoI, the cost estimate categories included detector, engineering, facilities, and R&D. A WBS with a mix of bottoms-up estimation (primarily for the calorimeter options and toroids) and parametric analysis (e.g., use of average cost per pound for finished material or a completed system) were used, and the derived costs were considered to be quite conservative. Given that the EEoI focused on physics goals and optimal performance, and included a wide variety of technology options, it would have been premature to attempt a detailed determination of contingencies or escalation. One of the primary points made in the EEoI was that a series of iterations would be employed by the collaboration to trade off physics performance, engineering feasibility, and cost considerations in arriving at the optimum system. In addition, it was assumed that detailed cost and program guidelines would be forthcoming from the SSCL. Indeed, the collaboration views the LoI as being consistent with the iterative process described in the EEoI.

7.3 EVOLUTION OF THE EMPACT/ TEXAS DETECTOR

The detector described in this LoI is clearly based on the system presented in the EEoI, albeit with a number of significant changes and improvements. These differences can be grouped into three categories, based on the motivation for making the change or improvement:

1) **Modifications of physics scope**, caused by the merger of the EMPACT, TEXAS, and 10^{34} groups;
2) **Design improvements** that yield a better performance-to-cost ratio;
3) **Descoping** to reduce costs.

In addition, significant improvements in our understanding of costs and contingencies have resulted from more detailed breakdowns of the elements that comprise detector subsystems (e.g., detailed examination of cryogenic service requirements), as well as improvements in understanding of component (e.g., electronics) and support equipment (e.g., test beam calibration) costs.

Table 7-1 summarizes for each of the above categories, the changes and improvements made to each subsystem that have a significant cost impact.

Table 7-1 Changes and improvements made in developing the EMPACT/TEXAS detector.

	Modifications of Physics Scope	Design Improvements	Descoping
Tracking	Scintillating Fiber Imaging Preradiator with Silicon Pads (LAr and SPACAL)		Elimination of Vertex Detector Reduction in TRD Channel Count (25%)
Calorimetry	Fine Sampling EM Calorimetry (LAr and SPACAL)	Increased Size of Individual Modules (LAr and SPACAL) Use of Lead Eutectic and Decreased Scintillator/Lead Ratio (SPACAL)	Reduction in Number of EM and HAD Transverse and Longitudinal Segments Increased Fiber Diameter (HAD SPACAL) Use of Lead Absorber (LAr)
Muon System	Barrel Toroid Inner Radius Increased to 5.15 Meters in Order To Remove Radial Constraint on Calorimeter	Redesigned Muon System	Reduce End Toroid Length and Field Reduction in Number of Muon Channels (20%)
Support Structure		Redesign of Detector Support Bridges	

7.4 LoI COST ESTIMATE METHODS

The process by which the detector cost estimates and contingencies were arrived at is described in detail below.

7.4.1 Detailed Work Breakdown Structure

A detailed WBS has been developed for accumulating detector cost estimates [1]. This WBS is based on existing detectors (DØ and SLD) and has been expanded to include SSC specific items. Continuous contact with the SSCL has resulted in a WBS fully integrated with the SSCL project WBS and currently breaks down to nine levels. There are approximately 550 WBS elements included in the current WBS structure. Table 7-2 shows a partial cut away view of the WBS.

7.4.2 Bottoms-Up Estimates

The nominal cost of a subsystem is built from the cost estimates of components, processes, and units of labor. With the use of computer-aided

Table 7-2 Example of the EMPACT/TEXAS WBS.

WBS Number	WBS Level	Program Element	EDI/QA	M&S	Total ($k)
5.2.1.2b	**4**	**SPACAL**	17,642	68,435	86,078
5.2.1.2.1	5	Central Calorimeter	8,630	28,604	37,234
5.2.1.2.1.1	6	Ring 1	3,846	3,439	7,284
5.2.1.2.1.1.1	7	Assemble Towers		675	675
5.2.1.2.1.1.2	7	Tower Assemblies		2,764	2,764
5.2.1.2.1.1.2.1	8	Lead (Eutectic 158)		1,672	1,672
5.2.1.2.1.1.2.2	8	Fiber (3 mm)		305	305
5.2.1.2.1.1.2.3	8	Fiber (0.5 mm)		434	434
5.2.1.2.1.1.2.4	8	Photomultipliers		200	200
5.2.1.2.1.1.2.5	8	Tower End Fittings		154	154
5.2.1.2.1.2	6	Ring 2		2,587	2,587
5.2.1.2.1.2.1	7	Assemble Towers		506	506
5.2.1.2.1.2.2	7	Tower Assemblies		2,081	2,081
5.2.1.2.1.2.2.1	8	Lead (Eutectic 158)		[illegible]	

engineering (CAE) models and the WBS, the subsystems are broken down to individual components. Information from the engineering models such as weights, materials, specifications, tolerances, dimensions, quantities, drawing counts, etc. is used for developing engineering and material requirements. This information is then used to obtain material estimates from vendors.

Labor estimates are developed largely from detailed manufacturing estimates. Manufacturing plans are used for outlining the tasks to be performed for assembly (e.g., of the toroids and calorimeter). Industrial engineers then determine the machine and labor hours required for each task. This information is organized into spreadsheets for compilation of costs by the EMPACT/TEXAS cost model. We note that all estimates are first done in FY1990 dollars, and later escalated according to the schedule.

7.4.3 Cost Model

To facilitate the cost-estimating process, a computerized cost model [1] is employed. This spreadsheet-based tool is invaluable for estimating costs for various detector design configurations in a short time period, providing valuable information for decision making. For each WBS item, the model includes cost parametrics, bottoms-up cost estimates, analogies to historical detectors, and other pertinent information that relate cost to physics performance. The utility of the cost model is apparent when the effects of design improvements or descoping options are rapidly evaluated. The cost model contains the following data concerning labor rates and EDI/QA.

7.4.3.1 Labor Rates—To standardize the detector cost estimates, labor rates provided by the SSCL have been incorporated into the cost model for determining nominal costs. SSCL-provided rates include those for work done at SSCL by SSCL employees or local "job shop" labor, as well as rates for large and small industrial vendors of high-technology products or services such as superconducting magnet design and fabrication. The latter rates were used, for example, in estimating costs of calorimeter and toroid design and fabrication. Standard industrial factors (where not provided by SSCL) are applied to the base rates for overhead, and general and administrative service. SSCL-provided job shop and contractor labor rates are used for assembly and installation activities.

7.4.3.2 EDI/QA—EDI/QA as defined by SSCL for the LoI covers the following activities (1) preliminary design; (2) final design of systems; (3) procurement of components; (4) manufacture of components (planning and quality assurance); and (5) installation planning, supervision, checkout, and test. For this LoI, we include in EDI/QA the costs of engineering, technical oversight, and QA associated with the tasks listed above.

7.4.4 Risk Analyses and Contingency Determination

A contingency is the quantitative expression of the technical, cost, and schedule risks that are associated with each WBS element. The better one understands the technical challenges, the detailed elements of a subsystem, and the unit labor and component costs, the better one should be able to fix the nominal cost and the smaller the associated contingency. A large contingency can result from a significant technical concern (e.g., the manufacture of radiation-hard scintillating fibers); a cost concern (e.g., uncertainty in labor rates); a schedule concern (e.g., manufacturing capacity); or any combination thereof.

A considerable effort has been expended to perform risk analyses and contingency determination in a manner consistent with the SSCL guidelines.

One begins with quantitative analysis of cost, technical, and schedule risks at the lowest level estimated (lowest WBS element). The risk is arrived at by the use of engineering and program experience and judgement, historical data, and vendor information, and quantified by the scale given in Table 7-3. Higher risk factors are given to WBS elements where, for example, the design approaches the state of the art or where the cost

Table 7-3 Technical cost, and schedule risk factor definitions.

Risk Factor	Technical	Cost	Schedule
1	Existing Design and Off-the-Shelf H/W	Off-the-Shelf or Catalog Item	
2	Minor Modifications to an Existing Design	Vendor Quote from Established Drawings	No Schedule Impact of Any Other Item
3	Extensive Modifications to an Existing Design	Vendor Quote with Some Design Sketches	
4	New Design, within Established Product Line	In-house Estimate for Item within Current Product Line	Delays Completion of Noncritical Path Subsystem Item
6	New Design, Different from Established Product Line; Existing Technology	In-house Estimate for Item with Minimal Company Experience but Related to Existing Capabilities	
8	New Design, Requires Some R&D Development but Does Not Advance State-of-the-Art	In-House Estimate for Item with Minimal Company Experience and Minimal In-House Capability	Delays Completion of Critical Path Subsystem Item
10	New Design, Development of New Technology Which Advances State-of-the-Art	Tops-Down Estimate from Analogous Programs	
15	New Design Way Beyond the Current State-of-the-Art	Engineering Judgement	

estimate is arrived at without a reliable vendor quote.

For each assigned risk factor, a weight is applied based on the severity of the risk, as described in Table 7-4. For example, a technical risk that affects design and manufacturing warrants a 4% weight, while a risk that affects only design is weighted by 2%. Similarly, a cost risk that is determined to result from uncertainty in material and labor costs warrants a 2% weight, while risk caused only by labor rate or material cost uncertainty is weighted by 1%. The resulting possible contingency ranges are from 5% to 98%. For example, vendor quotes from a completed drawing for a new design with minimum schedule effect would result in a contingency value of 12% (i.e., 2 x 4% technical + 1 x 2% cost + 2% schedule), a realistic value for a component at this level. Contingency determinations for each WBS element have been made [1].

Large cost versus risk assignments for WBS elements result from two rather distinct causes. A large contingency occurs when specific cost concerns are identified, for example, the cost of radiation-hard scintillating fiber or the exact number of steps (and thus the cost) of manufacturing a calorimeter module. Alternatively, large contingencies also occur in the few cases where nominal costs are calculated by simply scaling existing systems. In this latter manner, a large contingency can in fact be associated with a "low-tech" system such as support equipment or cooling.

The total contingency for the detector is arrived at by multiplying the derived risk percentage by the nominal cost for each WBS item and summing the resultant costs. The total (upper limit) cost is then the total nominal cost plus the total contingency.

It should be emphasized that summation of contingencies calculated in the above manner assumes a worst-case scenario at all levels. Historically, one can expect that, for some systems savings will accrue because of optimization, advances in technology and price breaks. The

Table 7-4 Technical, cost, and schedule weights for contingency determination.

Risk	Minimum	Maximum	Range
Technical Weights			
2% (Design or Manufacturing)	1	15	2%-30%
4% (Design & Manufacturing)	1	15	4%-60%
Cost Weights			
1% (Material Cost or Labor Rate)	1	15	1%-15%
2% (Material Cost & Labor Rate)	1	15	2%-30%
Schedule Weight			
1%	2	8	2%-8%
			5%-98%

detector cost plus contingency calculated in the manner described above is in fact an upper limit on the detector system cost.

7.5 EMPACT/TEXAS COST AND CONTINGENCY ESTIMATES

7.5.1 Major Subsystem Nominal Costs

Particular attention has been paid to the three areas—calorimetry, toroids, and electronics—that compose 75% of the total cost. We discuss these below. Cost details of other subsystems are available [1].

7.5.1.1 Toroids—The engineering feasibility of superconducting toroidal magnet systems is not an issue, given the history of magnetic confinement fusion. The real focus is on the question of cost effectiveness. To this end, we have undertaken detailed cost studies of the engineering designs discussed in Section 3.0. The nominal costs and associated contingencies presented in this LoI for the toroid system reflect a robust design that incorporates the most conservative features of three independent design and cost studies performed by Grumman Corporation, General Dynamics Corporation, and Ansaldo Componenti. For consistency, final labor costs were determined using rates provided by the SSCL as representative of large commercial superconducting magnet designers and fabricators. Confidence in the design and cost estimates are strengthened by the fact that together, Grumman, General Dynamics, and Ansaldo have an unparalleled wealth of experience in the design and fabrication of large superconducting magnets in a very cost-competitive environment.

7.5.1.2 Calorimetry—Cost estimates for calorimetry are based on thorough engineering designs, a detailed WBS, and careful manufacturing and assembly plans. The LAr calorimeter system design is based on extensive work done by Martin Marietta [2]. For SPACAL, independent designs and cost estimates were made by Martin Marietta and the Francis Stark Draper Laboratories, and included examination of a number of module manufacturing scenarios to minimize assembly steps and labor [3]. These designs are described in this LoI and supporting EMPACT/TEXAS Notes.

For both systems, care has been taken to include the cost of support systems, including cryogenic services, handling and assembly equipment, and *in situ* and test beam calibration.

7.5.1.3 Electronics—Electronics is clearly a major component of the overall cost of the detector, and is too often dealt with by a broad-brush "average" costs per channel. To reinforce confidence in the nominal cost and contingency estimates, we present here the basis for our electronics costs in some detail. These costs are based on studies with LeCroy Corporation of the actual costs of selected commercial products used in high-energy physics experiments [4]. As such, they represent the costs of well-understood technologies, but do not take into account reductions in cost that may arise from new but unproven methods [4].

The design philosophy adopted for the detector electronics is conventional and conservative. The intent of this choice is not to restrict the design of the final system, but rather to increase the reliability of the electronics cost estimates. Also, the costing

approach is designed to facilitate consistent cost estimation for a variety of circuits in the absence of detailed circuit designs. In this model, generic costs are determined for the design and manufacture of custom integrated circuits and printed circuit boards. These generic costs are based on recent and ongoing projects.

Table 7-5 summarizes the costs associated with custom integrated circuits (IC). The development component includes a feasibility study, design work, and prototyping. The difference in costs between ICs of high and low complexity reflects the higher design and prototyping costs associated with a more complex design. The production costs for ICs include manufacturing, testing, and packaging.

Table 7-5 also shows costs for printed circuit boards (PCB). Complex boards are FASTBUS-sized (40 x 40 cm^2) that typically accommodate 128 readout (ADC or TDC) channels. A typical example of a simple board is a chamber-mounted preamplifier-discriminator card housing 16 channels. The production costs, which are per unit, exclude the cost of the custom ICs but include standard components, automated assembly, automated testing, and the boards themselves. The production costs for complex and simple boards are consistent with an approximately size-independent figure of $12.50 per square inch.

Table 7-5 Generic development /production costs for integrated circuits and printed circuit boards.

Generic Electronics Cost Data	Complex	Simple
IC Development	$395k	$260k
IC Production (per Unit)	$10-16	$10-16
PCB Development	$285k	$110k
PCB Production (per Unit)	$3.1k	$240

Finally, each readout circuit board is assessed an additional $900.00 slot charge, reflecting the cost of the crate mechanics, low-voltage power supplies, and cooling. With the above numbers, plus figures for miscellaneous items such as high- voltage power supplies, cables, and system installation and testing, the task of cost estimation reduces to determining the number of channels of a given design that can be accommodated per IC or PCB.

Table 7-6 summarizes the costs by subsystem. The large system-to-system variation in high-voltage power supply costs per channel reflects the variation in the number of channels per supply module.

Table 7-6 Costs of front-end electronics for the TRD Tracker, LAr calorimeter system, SPACAL, and the muon chamber system.

TRD	R&D ($k)	EDI/QA ($k)	Mfg/Channel
High Voltage	$0	$80	$1.33
Amplifier	$184	$184	$17.00
Cable	$0	$80	$5.50
ADC or TDC	$441	$277	$29.91
Total	$625	$621	$53.74
LAr Calorimeter	R&D ($k)	EDI/QA ($k)	Mfg/Channel
Preamp	$301	$91	$25.00
Cable	$0	$80	$5.50
High Voltage	$0	$80	$0.23
ADC	$441	$277	$64.00
Total	$742	$528	$94.73
SPACAL	R&D ($k)	EDI/QA ($k)	Mfg/Channel
High Voltage	$220	$143	$51.80
ADC	$441	$277	$64.00
Cable	$0	$80	$20.00
Total	$661	$500	$135.80
Muon System	R&D ($k)	EDI/QA ($k)	Mfg/Channel
Preamp	$0	$80	$1.33
Cable	$184	$184	$17.00
High Voltage	$0	$80	$5.50
ADC	$441	$277	$33.00
Total	$625	$621	$56.83

7.5.2 Contingency Determinations

Table 7-7 gives examples of the numerical risk assignments for detector materials and services activities. A similar approach is taken for EDI/QA risk assignments. These tables are based on the WBS and employ the method presented in the previous section. Complete tables of risk assignments for each element of the WBS are available [1].

7.5.3 Cost and Contingency Tables

Table 7-8 presents the top-level WBS breakdown of costs and contingencies. Tables 7-9 through 7-16 give the second-level WBS breakdowns in 1990 dollars for each subsystem, including nominal cost and contingency

Table 7-7 Example of risk assignments for manufacturing contingency analysis.

WBS Number	WBS Level	Program Element	Materials and Services Contingency Analysis						
			Tech Wt	Cost Wt	Tech %	Cost %	Sched %	Composite Risk %	M&S w/ Contingency
5.2.1.2a	**4**	**Liquid Argon Calorimetry**						**21.2%**	**80,321**
5.2.1.2.1	5	Central Calorimeter						19.5%	31,000
5.2.1.2.1.1	6	Central Vacuum Vessel	4	3	2%	2%	2%	16.0%	179
5.2.1.2.1.2	6	Central Argon Vessel	4	3	2%	2%	2%	16.0%	2,090
5.2.1.2.1.3	6	Feedthroughs	8	10	2%	2%	2%	38.0%	1,818
5.2.1.2.1.4	6	Support Tube	4	4	2%	2%	2%	18.0%	1,644
5.2.1.2.1.5	6	Cooling Coils	4	10	2%	2%	2%	30.0%	138
5.2.1.2.1.6	6	Cooling Piping	4	10	2%	2%	2%	30.0%	164
5.2.1.2.1.7	6	Insulation	2	2	2%	2%	2%	10.0%	1
5.2.1.2.1.8	6	Support Tube Support	4	4	2%	2%	2%	18.0%	1,122
5.2.1.2.1.9	6	Modules						17.4%	20,505
5.2.1.2.1.9.1	7	1 - End Outer						14.8%	2,503
5.2.1.2.1.9.1.1	8	Absorber Material	2	3	2%	1%	4%	11.0%	580
5.2.1.2.1.9.1.2	8	G-10 Boards	4	4	2%	1%	4%	16.0%	697
5.2.1.2.1.9.1.3	8	Manufacturing Labor						16.0%	1,226
5.2.1.2.1.9.1.3.1	9	Channel	4	6	2%	1%	2%	16.0%	13
5.2.1.2.1.9.1.3.2	9	Plate	4	6	2%	1%	2%	16.0%	7
5.2.1.2.1.9.1.3.3	9	Strongback	4	6	2%	1%	2%	16.0%	16
5.2.1.2.1.9.1.3.4	9	End Cap	4	6	2%	1%	[illegible]		
5.2.1.2.1.9.1.3.5	[illegible]	[illegible]							

assignments. The breakdown of costs and contingencies (also in FY90 dollars) to lower WBS levels, as well as the SSCL provided costs for facilities and computing, can be found in Ref. 1.

7.6 SCHEDULE AND ESCALATED COSTS

7.6.1 Schedule

Figure 7-1 presents a first-level schedule for the development, design, engineering, fabrication, and installation of the detector consistent with the most recent overall SSCL project schedule (i.e., commissioning in March 1999). This schedule is the basis for the funding profiles presented below.

Figure 7-2 shows the key events and milestones in the 1991–92 timeframe with particular emphasis on the process by which major technology choices will be made. This "critical path" to the choices that define the final configuration of the detector is based on iterative physics performance/engineering feasibility and cost tradeoff approach emphasized in the EEoI (see, in particular, Figure 8-3) and on the inside cover of the divider for this section.

7.6.2 Escalated Costs

Figures 7-3(a) and (b) show the funding profiles and total expenditures per year in FY90 dollars and then-year dollars, respectively. Then-year dollars are calculated according to the escalation factors provided by the SSCL.

We emphasize the significant amount of funding necessary in the 1991–92 timeframe to perform the development and engineering required to make technology choices, particularly regarding calorimetry. With adequate initial-phase funding we can assure the completion of the detector system by March 1999.

Table 7-8 EMPACT/TEXAS cost and contingency summary.

WBS Number	Detector System	Costs in 1990 $k			Contingency Value	Total w/ Contingency
		Detector	EDI/QA	Total		
5.2.1.1	**Tracking**					
5.2.1.1.1	Preshower Detector	5,096	1,100	6,195	33.4%	8,262
5.2.1.1.2a	Tracking Pads (LAr)	1,458	219	1,677	27.5%	2,138
5.2.1.1.2b	Tracking Pads (SPACAL)	1,463	219	1,682	27.6%	2,146
5.2.1.1.3	TRD	11,370	1,252	12,622	20.1%	15,163
5.2.1.2	**Calorimetery**					
5.2.1.2a	**LAr Option**					
5.2.1.2.1, 2	Central + Ends	49,834	16,250	66,085	19.3%	78,857
5.2.1.2.3	Forward	9,870	2,052	11,922	28.6%	15,335
5.2.1.2.4	Cryogenic System	4,122	3,684	7,806	12.6%	8,788
5.2.1.2b	**SPACAL Option**					
5.2.1.2.1, 2	Central + Ends	55,344	15,789	71,133	31.5%	93,557
5.2.1.2.3	Forward	13,091	1,853	14,945	32.5%	19,803
5.2.1.3	**Toroids**					
5.2.1.3.1	Central	50,215	4,237	54,452	25.8%	68,515
5.2.1.3.2	Ends	53,381	4,530	57,911	23.0%	71,257
5.2.1.3.3	Dump Protection System	1,900	240	2,140	16.0%	2,482
5.2.1.3.4	Cryogenic System	9,437	1,009	10,446	14.8%	11,990
5.2.1.4	**Muon Detectors**					
5.2.1.4.1	Detectors	28,575	4,286	32,861	35.8%	44,613
5.2.1.4.2	Gas System	1,650	248	1,898	21.5%	2,305
5.2.1.4.3	Alignment and Positioning	6,550	1,100	7,650	13.7%	8,699
5.2.1.5	**Signal Handling**					
5.2.1.5.1	Front End Electronics					
5.2.1.5.1.1	Preshower Detector	2,086	209	2,295	26.0%	2,891
5.2.1.5.1.2a	Tracking Pads (LAr)	3,332	333	3,665	26.0%	4,618
5.2.1.5.1.2b	Tracking Pads (SPACAL)	1,612	161	1,773	26.0%	2,235
5.2.1.5.1.3	TRD	15,477	621	16,098	20.7%	19,424
5.2.1.5.1.4a	LAr Calorimeter	11,398	528	11,926	22.2%	14,569
5.2.1.5.1.4b	SPACAL	3,730	500	4,230	18.4%	5,009
5.2.1.5.1.5	Muon Detectors	23,318	621	23,939	10.5%	26,456
5.2.1.5.2	Trigger and Event Building	16,280	1,820	18,100	15.6%	20,915
5.2.1.5.3	Data Acquisition	2,144	214	2,358	24.0%	2,924
5.2.1.5.4, 5	Control/Monitoring Systems	2,700	270	2,970	24.0%	3,683
5.2.1.6	**Support Structure**	4,161	256	4,417	19.8%	5,293
5.2.1.7	**Project/SSC Interface**					
5.2.1.7.1	Power and Electrical	535	63	598	13.8%	681
5.2.1.7.2	Compressed Air System	245	24	269	29.1%	348
5.2.1.7.3, 4	Detector Specific Cooling	269	27	296	29.1%	382
5.2.1.7.5	Fixtures/Handling Eq.	4,240	1,093	5,333	30.4%	6,952
5.2.1.7.6	Safety Systems	414	41	456	32.7%	605
5.2.1.7.7, 8	Counting House	554	273	827	26.7%	1,048
5.2.1.7.9	Cable Handler	1,217	243	1,460	28.3%	1,874
5.2.1.8	**Calibration in Test Beam**					
5.2.1.8a	LAr Option	2,602	260	2,862	20.1%	3,438
5.2.1.8b	SPACAL Option	1,687	169	1,856	29.5%	2,403
5.2.1.9	**Detector Installation**	12,091	1,687	13,778	23.4%	16,997
5.2.1.10	**Integration/Management**	18,350	2,667	21,017	20.3%	25,274
5.2.1a	**Total LAr Option**	354,871	51,457	406,329	22.3%	496,776
5.2.1b	**Total SPACAL Option**	349,182	46,823	396,005	24.8%	494,185

Table 7-9 Tracking system costs and contingencies.

Tracking	Nominal Cost ($k)	Cont Value	Cost w/ Cont ($k)
Preshower Detector	6,195	33.4%	8,262
Tracking Pads (LAr)	1,677	27.5%	2,138
Tracking Pads (SPACAL)	1,682	27.6%	2,146
TRD			
Straws	11,520	20.0%	13,824
Radiators	86	21.8%	105
Support Frame	36	21.8%	44
Cables	420	21.4%	510
Gas Routing	180	21.4%	219
Thermal System	180	21.4%	219
Gas System	200	21.7%	243
Total (LAr Option)	20,494	24.7%	25,564
Total (SPACAL Option)	20,500	24.7%	25,571

Table 7-10 LAr costs and contingencies.

LAr Calorimeter	Nominal Cost ($k)	Cont Value	Cost w/ Cont ($k)
Modules	39,443	17.9%	46,497
Argon/Vacuum Vessels	6,314	15.1%	7,266
Feedthroughs	3,870	35.4%	5,240
Cooling Coils/Piping	2,894	17.3%	3,395
Support Tube	2,902	17.2%	3,402
Assembly & Test	6,561	18.8%	7,795
Tooling/Test Equipment	4,099	28.3%	5,260
Forward Calorimeter	11,922	28.6%	15,335
Cryogenic Systems	7,806	12.6%	8,788
Total	85,813	20.0%	102,979

Table 7-11 SPACAL costs and contingencies.

SPACAL	Nominal Cost ($k)	Cont Value	Cost w/ Cont ($k)
Tower Assembly	19,108	29.3%	24,702
Lead	14,815	32.0%	19,556
Fiber	5,347	50.3%	8,037
Photomultipliers	2,646	34.0%	3,546
Tower End Fittings	2,301	26.0%	2,900
Calorimeter Assy & Test	6,170	20.4%	7,430
Support Structure	3,807	16.5%	4,436
Tooling/Test Equipment	16,939	35.5%	22,950
Forward Calorimeter	14,945	32.5%	19,803
Total	86,078	31.7%	113,360

Table 7-12 Muon system costs and contingencies.

Muon System	Nominal Cost ($k)	Cont Value	Cost w/ Cont ($k)
Conductor Structure	47,611	30.0%	61,894
Superconducting Winding	5,287	10.0%	5,816
Superconductor	26,705	30.0%	34,717
Dewar	9,794	16.0%	11,361
Insulation	2,747	30.0%	3,571
Feedthroughs	2,866	16.0%	3,325
Assy of 5-degree Coils	9,904	10.0%	10,894
Assy of 45-degree Coils	7,449	10.0%	8,194
Dump Protection System	2,140	16.0%	2,482
Cryogenic System	10,446	14.8%	11,990
Muon Detectors	32,861	35.8%	44,613
Alignment & Positioning	7,650	13.7%	8,699
Gas System	1,898	21.5%	2,305
Total	167,358	25.4%	209,861

Table 7-13 Signal handling costs and contingencies.

Signal Handling	Nominal Cost ($k)	Cont Value	Cost w/ Cont ($k)
Preshower Detector	2,295	26.0%	2,891
Tracking Pads (LAr)	3,665	26.0%	4,618
Tracking Pads (SPACAL)	1,773	26.0%	2,235
TRD	16,098	20.7%	19,424
Calorimeter (LAr)	11,926	22.2%	14,569
Calorimeter (SPACAL)	4,230	18.4%	5,009
Muon Detector	23,939	10.5%	26,456
Trigger and Event Building	18,100	15.6%	20,915
Data Acquisition	2,358	24.0%	2,924
Control/Monitoring Sys	2,970	24.0%	3,683
Total (LAr Option)	81,350	17.4%	95,480
Total (SPACAL Option)	71,762	16.4%	83,536

Table 7-14 Detector support structure and SSC interface costs and contingencies.

Support Structure	Nominal Cost ($k)	Cont Value	Cost w/ Cont ($k)
Overhead Support Sys	4,280	19.7%	5,121
End Toroids Roller Sys	137	25.5%	172
Total	4,417	19.8%	5,293
SSC Interface	**Nominal Cost ($k)**	**Cont Value**	**Cost w/ Cont ($k)**
Power and Electrical	598	13.8%	681
Compressed Air System	269	29.1%	348
Nonconventional Cooling	254	29.1%	328
HVAC Control	42	29.1%	54
Fixtures/Handling Eq	5,333	30.4%	6,952
Safety Systems	456	32.7%	605
Counting House	646	26.2%	815
Fixed Counting Area Eq	181	28.4%	232
Cable Handler	1,460	28.3%	1,874
Total	9,240	28.7%	11,889

Table 7-15 Test beam calibration costs and contingencies.

Calibration	Nominal Cost ($k)	Cont Value	Cost w/ Cont ($k)
LAr			
Cryostat	700	16.0%	812
Modules	1,093	18.1%	1,292
Electronics	409	22.0%	499
Fixtures	440	31.8%	580
Test Labor	220	16.0%	255
SPACAL			
Towers	932	34.7%	1,255
Electronics	264	18.4%	313
Fixtures	440	31.8%	580
Test Labor	220	16.0%	255
Total (LAr Option)	2,862	20.1%	3,438
Total (SPACAL Option)	1,856	29.5%	2,403

Table 7-16 Detector installation, integration, and management costs and contingencies.

Installation	Nominal Cost ($k)	Cont Value	Cost w/ Cont ($k)
Tracker	331	29.4%	428
Calorimeter	1,116	27.9%	1,428
Signal Handling	2,181	25.7%	2,741
Muon Detectors	706	29.4%	913
Trigger	429	29.4%	555
Toroids	7,384	19.5%	8,821
Data Acquisition	66	29.4%	86
Monitoring System	136	29.4%	175
Detector Sys C/O & Test	1,430	29.4%	1,850
Total	13,778	23.4%	16,997
Integration and Management	**Nominal Cost ($k)**	**Cont Value**	**Cost w/ Cont ($k)**
Sys Engr & Integration	12,315	20.3%	14,809
Project Management	2,486	20.3%	2,989
Int & Mgmt Travel	1,015	20.3%	1,221
Admin Services & Supt	5,201	20.3%	6,255
Total	21,017	20.3%	25,274

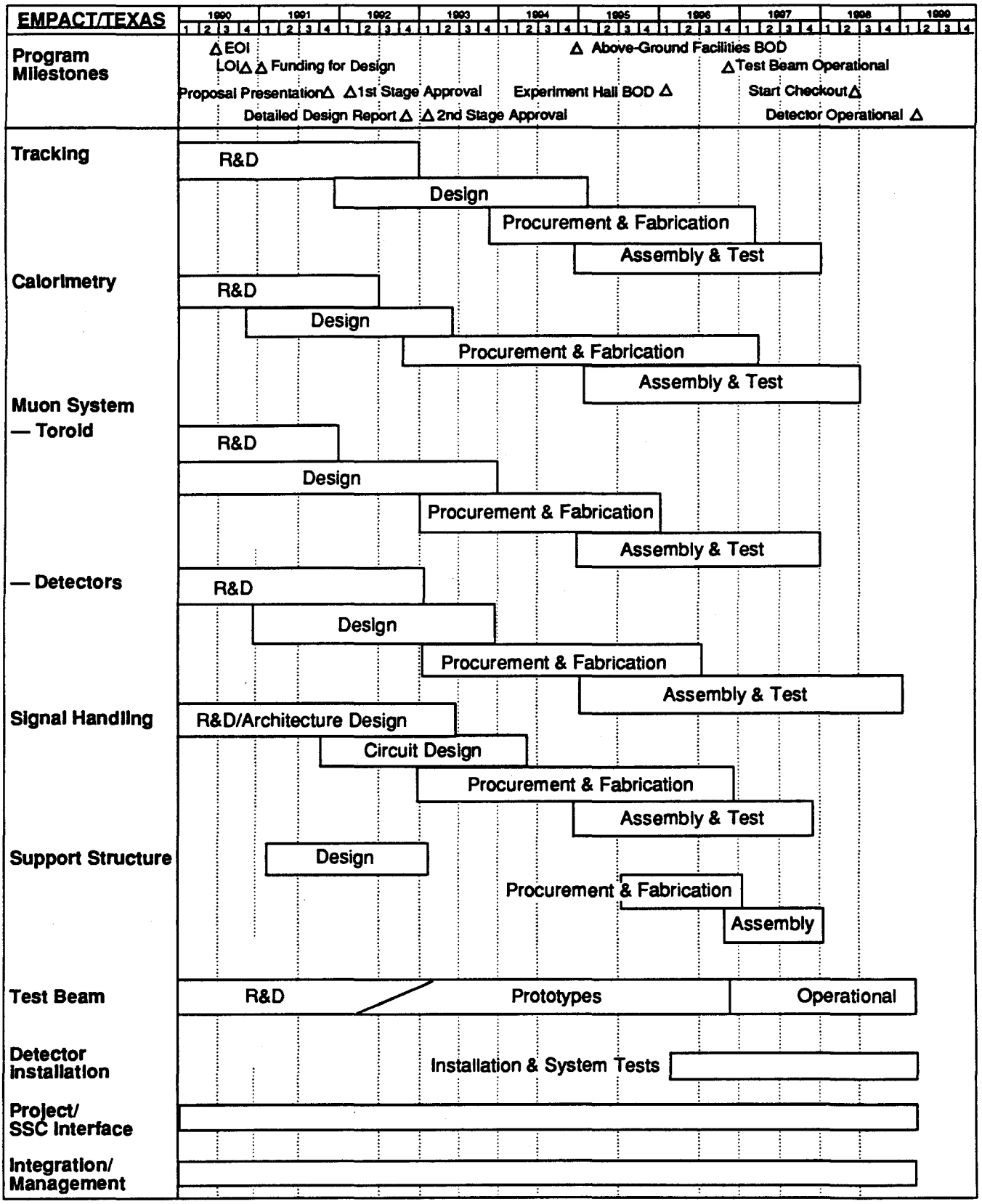

Figure 7-1 EMPACT/TEXAS schedule.

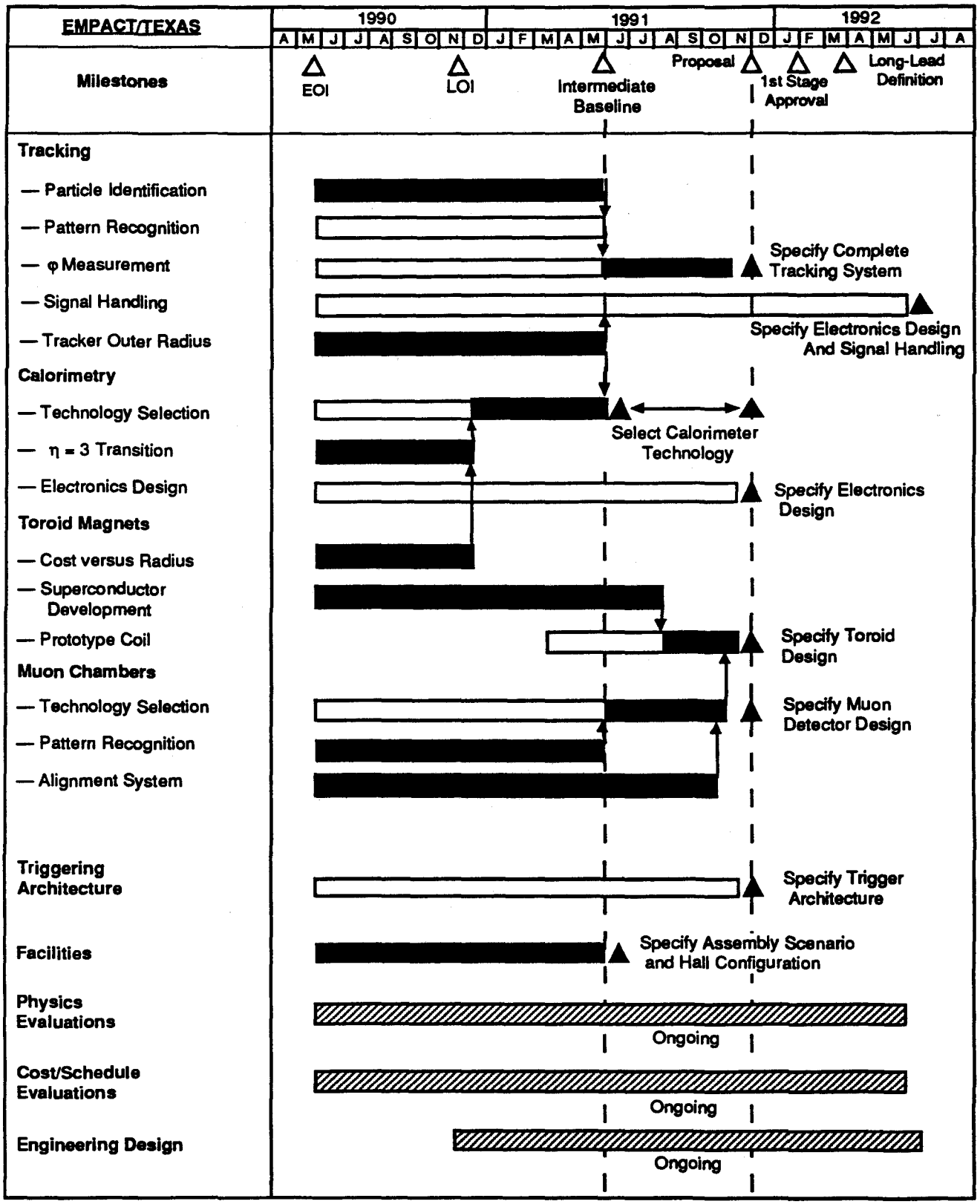

Figure 7-2 Key events and milestones in the development of EMPACT/TEXAS. Black lines indicate critical path activities.

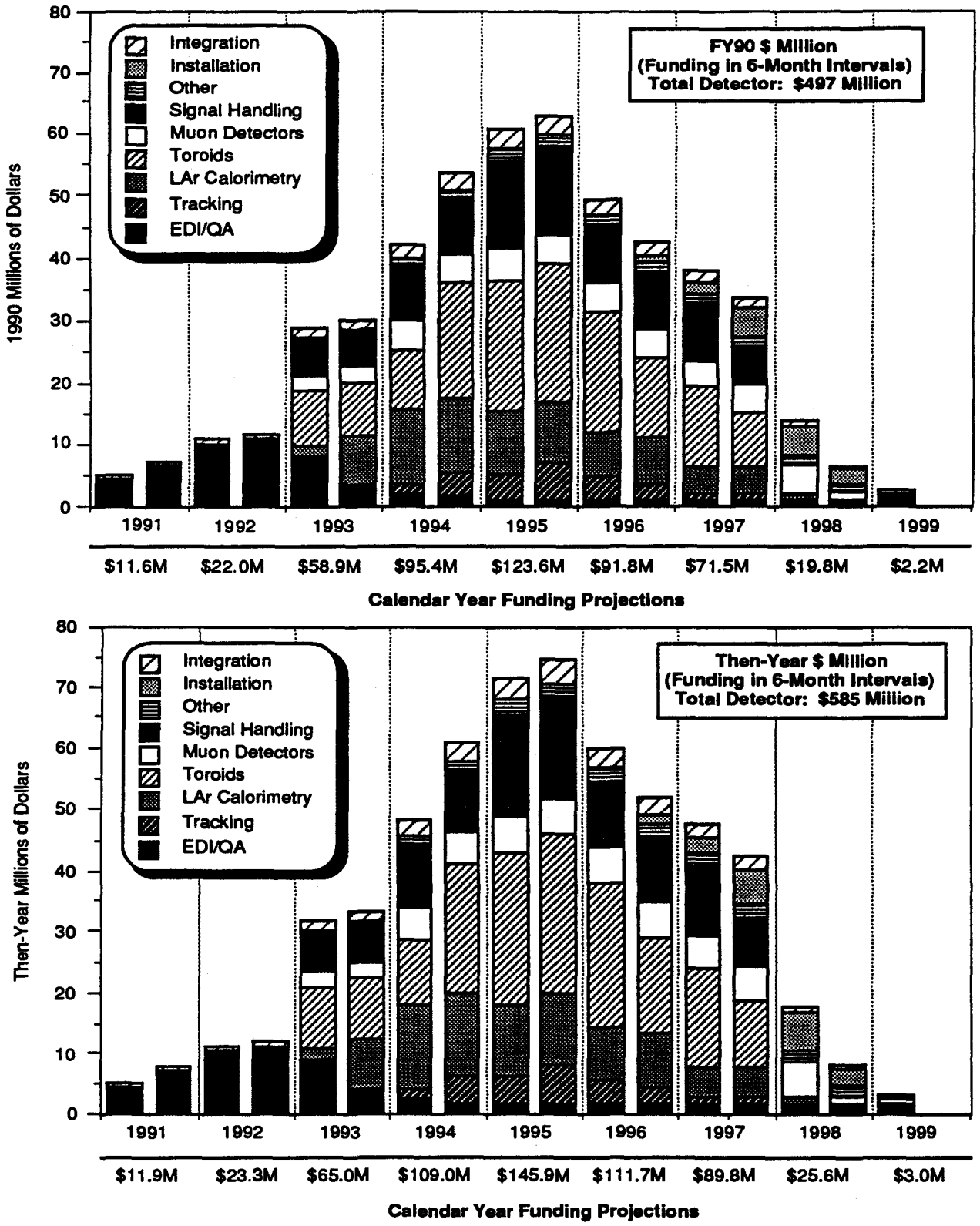

Figure 7-3 (a) Funding profile and annual expenditures in FY90 dollars, and (b) funding profile and annual expenditures in then-year dollars.

7.7 MANAGEMENT

7.7.1 Collaboration and Project Management

The EMPACT/TEXAS collaboration is a group of scientists with similar physics interests who believe that the detector proposed is the best way to pursue SSC physics. At the same time we recognize that the detector is an enormous high-technology project that must be designed, fabricated, assembled, and commissioned before experimentation can begin. The first step is to develop a sound, credible proposal. To this end, we propose an organization for 1991–92 timeframe and beyond, that relies on sound scientific direction, experienced engineering, strong project management, and clear fiscal oversight. This organization is shown in Fig. 7-4. The composition of the Collaboration Council, Scientific Policy Committee, and Technical Advisory Committee is described in Sect. 9 of the EEoI, as is the method of adding new institutions. We focus here on the project organization.

There are three features of the project organization shown in Fig. 7-4 that merit some elaboration. First, a project manager and support staff are assumed to be employees of the SSCL. This structure provides clear lines of SSCL project, fiscal, and contractual authority over the industrial members of the EMPACT/TEXAS team. Second, there are U.S. and Soviet physics coordinators for each subsystem. This recognizes the major Soviet contribution to EMPACT/TEXAS and assures good communication and efficient use of all resources. Third, the detector project as a whole has a chief engineer and each subsystem has a lead engineer. These engineers have been integrally involved from the EoI stage, understand the issues that drive the technology choices that must be made, and have the confidence of the collaboration.

The anticipated areas of interest and responsibility for collaborating institutions are listed in Table 7-17. The majority of these institutions are also participating in the detector R&D and simulation activities. It should be noted, however, that responsibilities are expected to evolve over the project lifetime, and that the collaboration as a whole, and each institution in particular, is committed to doing whatever is necessary to make EMPACT/TEXAS a success.

7.7.2 Post LoI Activities

The scope and schedule of the undertaking proposed here requires that we move decisively to the next stage. In December 1990 and January 1991, we will initiate the following specific actions to provide the logistical infrastructure for management and funding of the EMPACT/TEXAS project.

1) Select, in conjunction with the SSCL, a project manager and key project support personnel. In addition, we will establish SSCL—EMPACT/TEXAS interfaces and liaisons for safety, quality assurance, planning, contracts, finance, and cost control.

2) Negotiate funding for R&D, engineering, and proposal preparation with the SSCL. The fund requests presented in the EEoI and TEoI will, along with SSCL overall project schedule and funding considerations, form the basis for these negotiations.

3) Continue the development of critical-path facilities requirements and designs via the establishment of a standing joint EMPACT/TEXAS—SSCL Facility Design Group.

4) Hold a full collaboration meeting (Jan. 24–26 at SSCL) to formalize and coordinate all EMPACT/TEXAS proposal activities and R&D responsibilities.

5) Submit a formal plan to Soviet authorities for commitment of contributions to EMPACT/TEXAS.

6) Negotiate Memoranda of Understanding and/or contracts between the collaboration, SSCL, and all participating institutions.

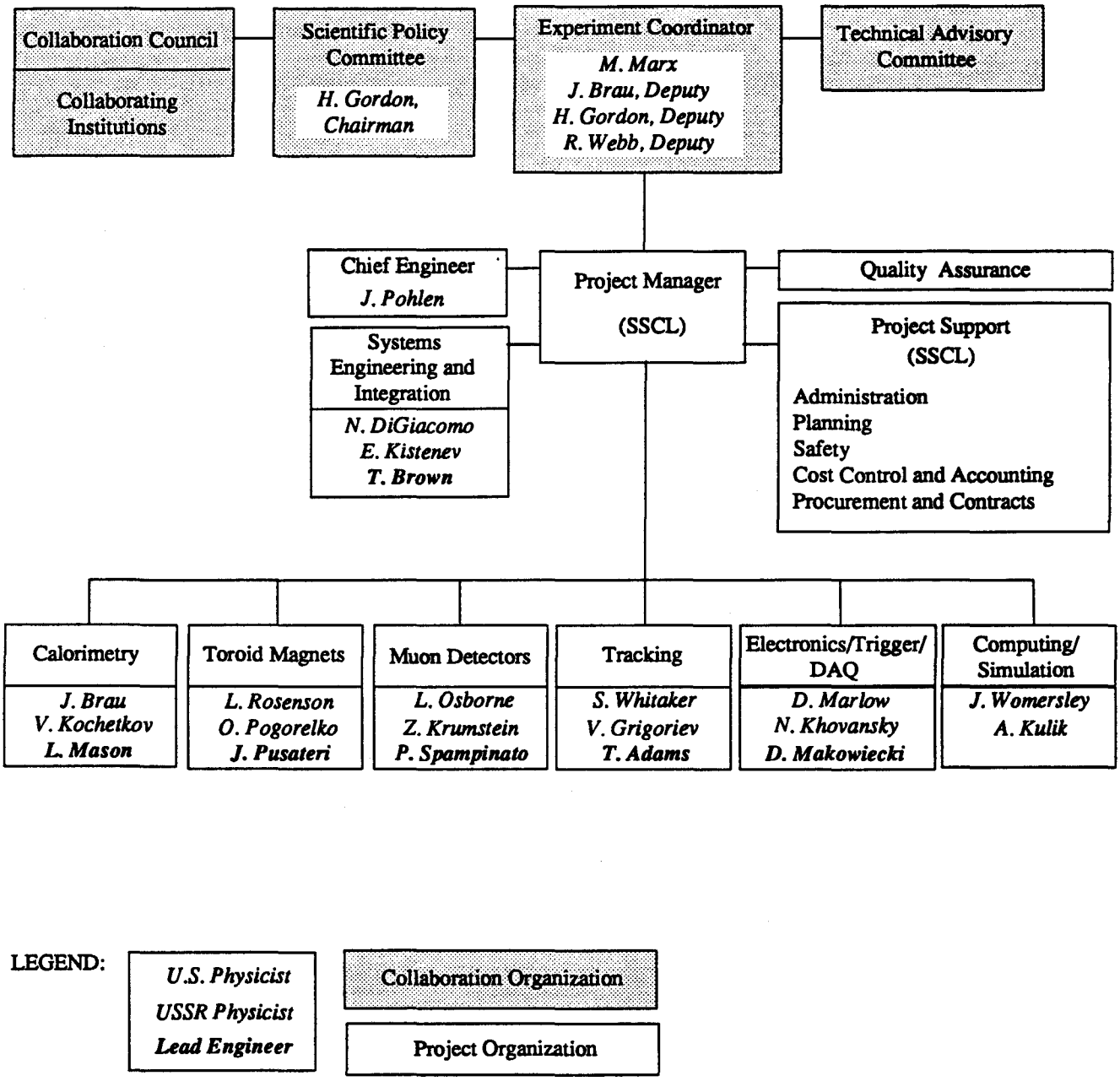

Figure 7-4 EMPACT/TEXAS organization for the proposal preparation period; the project manager and project support personnel (including cost control and contracts) are assumed to be SSCL employees.

Table 7-17 EMPACT/TEXAS member institutions and associated responsibilities.

Institution	Calorimetry	Muon	Toroid	Tracking	Trigger/DAQ	Simulation	Integration
Adelphi University	x						
University of Arizona	x	x				x	
Boston University	x			x			
Bowdoin College						x	
Brookhaven National Laboratory	x	x		x	x	x	x
University of California, Davis		x			x		
University of California, San Diego	x						
Carnegie Mellon University	x				x	x	
Drexel University		x					
Fairfield University	x				x		
Florida State University	x					x	
Grumman Corporation		x	x				x
Universidad de Guanajuato	x						
University of Houston		x			x	x	
Indiana University		x				x	
IHEP, Alma-Ata					x		
IHEP, Protvino	x	x		x	x	x	x
INP, Byelorussian State University					x		
INR, Moscow				x			
ITEP, Moscow	x		x			x	
Institute of Physics, Georgia, USSR						x	
JINR, Dubna		x		x	x	x	x
University of Kansas				x		x	
Lawrence Livermore Laboratory				x	x		
Lebedev Physical Institute				x			
Lehigh University						x	
Louisiana State University		x				x	
Martin Marietta Astronautics Group	x			x	x		x
U. of Massachusetts at Amherst						x	
MIT		x				x	
Michigan State University		x			x		
Moscow Engineering &Physical Institute				x			
Moscow State University, Moscow	x			x		x	
Moscow State University, Dubna		x				x	
Nanjing University, Nanjing					x	x	
New York University					x		
Northeastern University				x			
Oak Ridge National Laboratory			x				
University of Oregon	x					x	
Princeton University					x		
University of Rochester	x	x				x	
Universidade Estadual de Sao Paulo						x	
Universidade de Sao Paulo				x	x	x	
University of South Carolina				x			
State U. of New York at Stony Brook		x					x
SSC Laboratory						x	
Tbilisi State University						x	
Texas A&M University	x						
University of Texas at Austin					x		
Vanderbilt University		x		x			
Vassar College						x	
University of Washington	x			x		x	
College of William and Mary	x						
Yale University		x				x	
Yerevan Physics Institute						x	

REFERENCES

1. M. Montgomery *et al.*, "EMPACT/TEXAS Costs and Contingencies," EMPACT/TEXAS Note 342 (1990).
2.. T. Adams *et al.*, "Status of the EMPACT/TEXAS LAr Calorimetry Design," EMPACT/TEXAS Note 351 (1990).
3. C. Elder *et al.*, "Status of the EMPACT/TEXAS SPACAL Design," EMPACT/TEXAS Note 339 (1990).
4. T. Majors *et al.*, "EMPACT/TEXAS Electronics Costs," EMPACT/TEXAS Note 338 (1990).